

Optical Injection of High- β Quantum Dot Micropillar Lasers

vorgelegt von
Master of Science
Elisabeth Anna Katharina Schlottmann

an der Fakultät II - Mathematik und Naturwissenschaften
der Technischen Universität Berlin
zur Erlangung des akademischen Grades

Doktor der Naturwissenschaften
- Dr. rer. nat. -

genehmigte Dissertation

Promotionsausschuss:

Vorsitzende: Prof. Dr. Ulrike Woggon

Gutachter: Prof. Dr. Stephan Reitzenstein

Gutachter: Prof. Dr. Frédéric Grillot

Tag der wissenschaftlichen Aussprache: 20.12.2019

Berlin 2020

Contents

Abstract	1
Zusammenfassung	3
1 Introduction	5
2 Theoretical Background	9
2.1 Towards Semiconductor Lasers	9
2.2 Quantum Dot Micropillar Lasers	18
2.3 Laser Dynamics under Optical Injection	24
2.4 Photon Statistics	29
3 Experimental Methods	37
3.1 Sample Fabrication	37
3.2 Micro-Electroluminescence and -Photoluminescence	39
3.3 Measurement of Photon Statistics	43
4 Fundamental Emission Characteristics of Quantum Dot Micropillar Lasers	49
4.1 Intensity Characteristics and Bimodal Behavior	49
4.2 Temporal Emission Dynamics	53
5 Photon Number Distribution of Microlasers	59
5.1 Pulsed Electrical Excitation	59
5.2 Measurement of the Photon Number Distribution	63
5.3 Photon Statistics of Exciton-Polariton Lasers	78
6 Optical Injection Experiments in Quantum Dot Micropillar Lasers	89
6.1 Optical Injection in Single QD Mode Micropillar Lasers	89
6.2 Optical Injection in Bimodal QD Micropillar Lasers	104
7 Conclusion and Outlook	121
Formula Symbol and Abbreviation List	122

Bibliography	127
A Appendix	143
A.1 Layer Design Sample M4072	143
A.2 Layer Design Sample M2977	144
A.3 Layer Design Sample M4159	145
Acknowledgements / Danksagung	146

Abstract

The huge progress in laser miniaturization opens new fields of research at the crossroads between nanophotonics and nonlinear dynamics. Cavity-enhanced microcavities exhibit lasing close to the quantum regime and are excellent testbeds for exploring nonlinear dynamics at the low-power limit by optical injection. Quantum dot micropillar lasers exhibit a bimodal behavior that features intrinsic dynamics and intriguing photon statistics.

In the present thesis, the photon number distribution of two qualitatively different types of microlasers is investigated and injection locking of quantum dot micropillar lasers is explored.

The photon statistics is an important measure for the evidence of lasing in high- β microlasers operating at sub- μW light powers. Utilizing the outstanding photon detection capabilities of transition-edge sensors, the full photon number distribution of microlaser is measured for the first time to obtain profound insight into the emission dynamics of these nanophotonic devices. For bimodal quantum dot micropillar laser, two cases are distinguished. In the first case of a stable microlaser, one polarization mode undergoes a transition from thermal emission below threshold to a lasing state above threshold. Meanwhile, the other polarization mode transfers to a non-lasing thermal state. In the second case of a bistable quantum dot micropillar, both polarization modes have the potential to reach the lasing regime and the photon number distribution exhibits a superposition of a thermal and a coherent distribution in a single measurement. This behavior was inaccessible with common experimental techniques and is revealed by the photon number distribution.

The second type of microlaser under investigation is an exciton-polariton laser which is based on stimulated scattering and Bose-Einstein condensation of quasi-particles and not on population inversion as it is required for conventional photon lasers. The transition to lasing is investigated by means of the photon number distribution. The photon statistics exhibits a coherence buildup well described by thermal-coherent states. Slight deviations from the model can serve as the starting point for the examination with competing theories.

In the following experiments, quantum dot micropillar lasers are subject to optical injection. A single-mode microlaser reveals locking to the master laser. However, at the

boundaries, the microlaser discloses a 'partial locking' to the master laser which is a novel effect of the enhanced spontaneous emission. Optical injection into the non-lasing mode pushes this mode to lasing. Moreover, optical injection causes stochastic mode switching between the modes, depending on their relative strength and spectral detuning.

In summary, measurements of the photon statistics and optical injection experiments reveal new dynamics of microlasers and yield deeper insights into their physics. The results of this thesis have high potential to pave the way for the control of dynamics close to the quantum regime which is crucial for future applications, e.g. in photonic reservoir computing.

Zusammenfassung

Der enorme Fortschritt in der Laserminiaturisierung eröffnet neue Forschungsansätze im Spannungsfeld zwischen Nanophotonik und nichtlinearer Dynamik. Resonatorverstärkte Mikrokavitäten führen zu Laseremission nahe des Quantenregimes und eignen sich daher hervorragend als Versuchsobjekte, um durch optische Injektion an der unteren Leistungsgrenze die nichtlineare Dynamik zu erforschen. Quantenpunkt-Mikrosäulen-Laser zeigen ein bimodales Verhalten, welches sich durch intrinsische Dynamik und faszinierende Photonenzahlstatistiken auszeichnet. Im Rahmen dieser Arbeit wird die Photonenzahlverteilung zweier qualitativ unterschiedlicher Typen von Mikrolasern und optische Injektion von Quantenpunkt-Mikrosäulen-Lasern untersucht.

Die Photonenzahlstatistik ist ein wichtiges Maß für den Nachweis von Laseremission in Mikrolasern mit einem hohem β -Faktor, welche mit Leistungen unterhalb des μW -Regimes arbeiten. Unter Ausnutzung der hervorragenden Photonendetektionseigenschaften von supraleitenden Phasenübergangsthermometern (Transition-Edge Sensors) wird die vollständige Photonenzahlverteilung von Mikrolasern zum ersten Mal gemessen. Dadurch ergibt sich ein tieferer Einblick in die Emissionsdynamik von Mikrolasern. Im Zusammenhang mit bimodalen Quantenpunkt-Mikrosäulen-Lasern werden zwei Fälle unterschieden. Im ersten Fall eines stabilen Mikrolasers geht die eine Polarisationsmode von einer thermischen Emission unterhalb der Laserschwelle in einen lasenden Zustand oberhalb der Laserschwelle über. Währenddessen geht die andere Polarisationsmode in einen nicht-lasenden Zustand über. Im zweiten Fall eines bistabilen Quantenpunkt-Mikrosäulen-Lasers können beide Polarisationsmoden das Laserregime erreichen und die Photonenzahlverteilung zeigt eine Überlagerung einer thermischen und einer kohärenten Verteilung in einer Einzelmessung. Dieses Verhalten war unzugänglich mit üblichen experimentellen Techniken und wurde durch die mittels eines supraleitenden Phasenübergangsthermometers gemessene Photonenzahlverteilung aufgedeckt.

Der zweite hier untersuchte Mikrolasertyp ist ein Exziton-Polariton-Laser. Dieser beruht auf stimulierter Streuung und Bose-Einstein-Kondensation von Quasiteilchen und steht damit im Gegensatz zu einem herkömmlichen Photonenlaser, welcher auf Besetzungsinversion basiert. Der Übergang zu Lasing wird anhand der Photonenzahlverteilung untersucht. Die Photonenzahlstatistik zeigt einen durch thermisch-kohärente Mischzustände

gut beschriebenen Kohärenzaufbau. Geringe Abweichungen vom Modell können als Ausgangspunkt für die Überprüfung konkurrierender Theorien dienen.

In den folgenden Experimenten werden Quantenpunkt-Mikrosäulen-Laser optisch injiziert. Dabei zeigt sich eine Phasen- und Frequenzangleichung eines Einzelmoden-Mikrolasers an den Master-Laser. An den Grenzen offenbart der Mikrolaser jedoch eine "teilweise Angleichung" an den Master-Laser. Letzteres stellt einen neuartigen Effekt, hervorgerufen durch die verstärkten spontanen Emission dar. Die optische Injektion treibt die nicht-lasende Mode in einen lasenden Zustand. Darüber hinaus bewirkt die optische Injektion eine stochastische Umschaltung zwischen den Moden in Abhängigkeit von ihrer relativen Stärke und der spektralen Verstimmung.

Zusammenfassend lässt sich sagen, dass Messungen der Photonenstatistik und Experimente zur optischen Injektion neue Dynamiken von Mikrolasern aufzeigen und tiefere Einblicke in ihre Physik geben. Die Ergebnisse dieser Dissertation weisen ein hohes Potential auf, den Weg für die Kontrolle der Dynamik von Mikrolasern nahe des Quantenregimes zu ebnen. Dies ist für zukünftige Anwendungen, wie beispielsweise im Reservoir Computing, von entscheidender Bedeutung.

1 Introduction

The intersection of nanophotonics and nonlinear dynamics promises new exciting physics at the crossroads between classical and quantum physics. In this context, cavity-enhanced microlasers are ideal candidates to investigate nonlinear dynamics close to the quantum regime. Dynamics in lasers can be generated by external perturbations, e.g. by delayed feedback or an optically injected master laser. Lasers can also feature intrinsic dynamics. For instance, quantum dot (QD) micropillar lasers often possess a bimodal character leading to mode switching dynamics.

The small mode volume of microlasers in the order of the cubic wavelength enlarges light-matter interaction in these devices which is described in the framework of cavity quantum electrodynamics (cQED). Micropillars with only a few QDs as gain medium are interesting quantum optical devices which emit on-demand indistinguishable photons [San02, Din16] or entangled photon pairs [Dou10] in the weak coupling regime of cQED. They also show strong coupling [Rei04] as well as single-QD lasing effects [Gie17]. When it comes to lasing the large spontaneous emission factor β strongly reduces the threshold pump power for QD micropillars with suitably large QD density. This leads to a characteristic s-shaped input-output dependence [Bjö91] towards the limiting case of thresholdless lasing for $\beta = 1$ [Kha12].

For conventional semiconductor lasers with mW output powers, the large nonlinear increase of emission intensity at threshold in conjunction with a pronounced decrease of emission linewidth is an adequate measure for the verification of lasing. The threshold nonlinearity is less pronounced for microlasers with sub- μ W output powers which makes it difficult to identify lasing solely by the investigation of the input-output characteristics. An adequate method to prove the emission of coherent light from microlasers is the determination of the excitation power dependent second-order autocorrelation function $g^{(2)}(\tau)$ with a Hanbury-Brown and Twiss configuration [Ulr07, Kre17]. Alternatively, substantially more information about the photon statistics is given by the photon number distribution which can be determined by advanced photon number resolving detectors. Single-photon detectors, based e.g. on avalanche photodiodes, are not suitable for this purpose because they cannot measure the number of detected photons. In contrast, transition-edge sensors (TESs) reliably measure the photon number per light pulse and give direct access to the

underlying photon number distribution [Mil03]. Thus, TESs open the possibility to determine the full photon statistics of nanophotonic devices and gain a deeper insight into their physics. This is of particular interest for microlaser applications with relevant nonlinear processes like metrology [Boi09], subwavelength lithography [Cao10], ghost imaging [Gat04] and two-photon-excited fluorescence [Jec13].

Against this background, the investigation of nonlinear laser dynamics at ultra-low light levels is an important and widely unexplored research topic and state-of-the-art microlasers enable research down to the quantum limit. Overall, three key experiments are applied to evoke dynamics in lasers: Delayed feedback, optical injection and mutual coupling of lasers. In feedback experiments an external mirror reflects light back into the laser, building an external cavity. Early experiments revealed effects like linewidth tailoring or multistability [Lan80]. In optical injection experiments, an external master laser drives a target slave laser. Frequency locking of the slave laser to the master laser is a clear signature of interaction between the lasers and was observed already in the 1960s [Sto66]. Likewise, two lasers can be (mutually) coupled and synchronized [Fab93]. Semiconductor lasers are usually electrically driven and easy-to-handle and therefore favored test-bed systems for the study of laser dynamics [Ern10]. Optical injection was extensively studied in semiconductor lasers and induces complex dynamics [Wie05]. Interesting for applications is, for instance, the increasing modulation bandwidth with optical injection [Sim97].

Even though microlasers have become more important for applications [Ma19], their dynamical characteristics have not been much under focus. First experiments regarding optical feedback applied to QD micropillar lasers [Alb11] revealed the existence of chaotic effects by photon statistics measurements. Besides, Josephson junction lasers under optical injection showed classical locking behavior [Cas17]. Based on the first experiments in this field, the low threshold powers and small cavity photon numbers predict QD micropillar lasers to be very suitable for the investigation of feedback effects in the quantum regime [Car13]. The extension of investigations to microlasers is important for potential applications in all-optical flip-flops [Jeo06, Mor06] and reservoir computing [Bru15, Heu19] which relies on coupled lasers arrays [Lar12] and can strongly benefit from the small footprint and small threshold pump powers of microlasers.

Additionally, bimodal QD micropillar lasers are particularly interesting for the study of nonlinear dynamics because they provide inherent dynamics. In the case of structural asymmetries, the fundamental cavity mode is split into two orthogonal polarization modes that compete for the same gain [Ley13]. Typically, one mode is lasing while the second component is suppressed. In this case, stochastic polarization mode switching with rich dynamics can occur [Red16]. Similar intra-mode dynamics has also been reported for

ring-lasers [MT78], vertical-cavity surface-emitting lasers (VCSELs) [Vir13] and photonic crystal cavity lasers [Mar18]. Moreover, optical injection can induce polarization chaos in VCSELs [Gat06, DIC18]. Tailoring the switching dynamics in QD micropillar lasers finds potential applications in microwave generation [Lin17], random number generation [Uch08] and secure data communication [Rog01].

In this thesis, an experimental study of the photon statistics of QD micropillar lasers and exciton-polariton lasers, as well as optical injection in QD micropillar lasers, is presented.

Advantages of high- β QD micropillar lasers are the large fraction of spontaneous emission in the laser mode [Ler13] with only tens of QDs in the gain medium [Str06], while the electrical excitation allows for easy and stable handling in complex experimental configurations [Böc08]. The fundamental mode is usually split into two orthogonally polarized modes due to slight asymmetries on the pillars' cross section, already providing intrinsic mode switching characteristics [Red16].

Simple statistical measurements of the second-order autocorrelation are nowadays widely used for the study of microlaser devices [Ulr07]. We apply an alternative technique based on TESs which goes well beyond and enables the first measurement of the full photon number distribution for microlasers [Sch18b, Kla18b, Sch18c]. The lasing process in single-mode microlasers can be better understood and discloses intriguing novel dynamics of bimodal lasers.

Optical injection experiments examine the dynamics of spontaneous emission enhanced QD micropillar lasers. Their capability of injection locking is investigated and found to deviate from the classical behavior [Sch16]. The bimodal character and in particular the switching dynamics contribute interesting aspects to the investigations [Sch19]. Potential applications can be found in the fast data transmission.

The thesis includes 6 chapters:

The theoretical background in chapter 2 first discusses the fundamental laser theory. This includes the consideration of the principles of laser dynamics and its description via rate equations. An explanation of the spontaneous emission enhancement in low mode volume QD micropillar lasers is given then, followed by a description of the essential optical injection effects. Finally, the chapter closes with the characteristics of thermal and coherent photon statistics.

Chapter 3 describes the utilized microlaser devices and experimental methods. The fab-

rication and design structure of the QD micropillar laser and the exciton-polariton laser are explained in detail. The spectroscopic methods comprise advanced experiments based on micro-electroluminescence measurements as well as statistical measurements with a Hanbury-Brown and Twiss setup and a transition-edge sensor detection system.

Initial experimental results are presented in chapter 4. The characteristics of the optical spectrum of QD micropillar lasers and their temporal dynamics are described.

Chapter 5 comprises the full photon statistics of single-mode and bimodal QD micropillar lasers and their switching dynamics. Furthermore, the full photon number distribution of exciton-polariton lasers is presented and allows for a deeper understanding of the coherence built-up in these devices.

The optical injection experiments are demonstrated in chapter 6. The phase- and frequency-locking characteristics and the temporal dynamics of QD micropillar lasers are measured. Optical injection provokes mode switching in bimodal microlasers which is examined with cross-correlation experiments.

A conclusion and outlook are given in chapter 7.

2 Theoretical Background

This chapter introduces the theoretical background needed for the understanding of the experimental results of this thesis. An introduction of lasers with a focus on semiconductor lasers is given in the first section 2.1. It begins with a general description of lasers and introduces the rate equation model to describe the emission of semiconductor lasers. Section 2.2 explains the Purcell effect which leads to an enhanced spontaneous emission in microcavities which is essential for the operation of low mode volume microlasers. Section 2.3 discusses the dynamics of semiconductor lasers, necessary to understand the influence of optical injection presented in chapter 6. Finally, the photon statistics of thermal and coherent light sources is discussed in section 2.4. This section gives the basic background for the photon number distribution of microlasers presented in chapter 5.

2.1 Towards Semiconductor Lasers

Laser Principle

The word LASER is an acronym for 'light amplification by stimulated emission of radiation'. The first laser was experimentally realized in the year 1960 by Maiman [Mai60]. Any laser has three main components: A **source to pump** the **gain medium** to population inversion and a **cavity**.

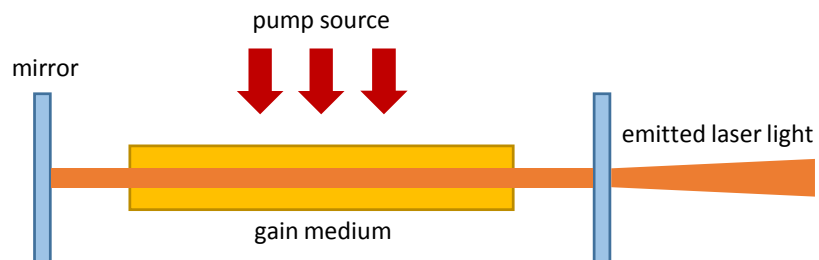


Figure 2.1: Schematic laser principle: A pump source excites the gain medium to population inversion. The gain medium can emit photons via spontaneous emission and by stimulated emission. The cavity is built by two opposite mirrors which reflect the emitted photons multiple times. One of the mirrors is partly transparent and transmits the laser light.

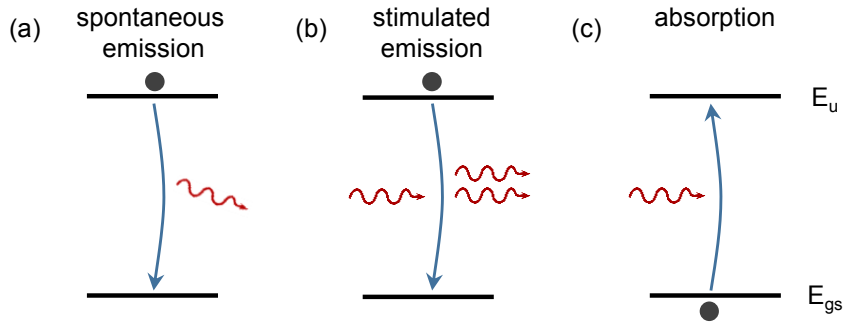


Figure 2.2: Radiative processes between two states. (a) Spontaneous emission: A charge carrier in an excited state descends to the lower state under emission of a photon with random phase and direction. (b) An incoming photon stimulates the emission of a second photon with the same energy and phase. (c) The absorption of a photon lifts the charge carrier to the excited state.

The following description and notation follow the book 'Laser' by Eichler and Eichler [Eic15] which can be recommended for an introduction to the general principles of lasers. In a simplified consideration, the emitters inside the laser gain medium can be described by a two level system. Three radiative effects occur between the two levels: Spontaneous emission, stimulated emission and absorption (see figure 2.2).

A charge carrier from the upper level passes to the lower level under the radiation of a photon with the energy $E_{\text{phot}} = E_u - E_{\text{gs}} = \hbar\nu$ and a random direction and phase. An incident photon with the matching energy E_{phot} stimulates the transition of a charge carrier. The emitted second photon adopts the phase and direction from the original photon. An incident photon can be absorbed by a charge carrier in the ground state E_{gs} under the transition to the upper state.

A cascade of stimulated emission is the basic requirement for laser radiation. Three preconditions have to be fulfilled in order for initiate and sustain the laser process by stimulated emission.

1. **Population inversion:** During the lasing process the upper level is populated with higher probability than the lower level. Then, the stimulated emission dominates over the absorption of photons.
2. **Resonator condition:** The cavity possesses modes within the emission spectrum of the gain medium. $m \lambda_{\text{cav}} = 2 n_{\text{eff}} L$ with $m \in \mathbb{Z}$. λ_{cav} is the wavelength of the cavity mode, n_{eff} the refractive index and L the length of the gain medium.
3. **Threshold condition:** $GRT > 1$. The gain G compensates the losses due to (wanted) mirror reflection $R = \sqrt{R_1 \cdot R_2} < 1$ and other losses, like reabsorption and scattering,

described by the transmission T .

Maxwell-Bloch Equations

To mathematically describe the laser process, we consider the electric field \mathbf{E} , the polarization of the gain medium \mathbf{P} and the population inversion n . In this section the laser rate equations are introduced, starting from the general case to the Maxwell-Bloch equations. The emission intensity is given by the electric field amplitude $I = |E^2|$ and the rate equation of the electric field can be rewritten for the intensity or the photon number, but the phase information gets lost.

The derivation of the Maxwell-Bloch equations is shortly retraced after reference [Oht12]. The electric field \mathbf{E} of a plane wave for a propagation in z -direction can be defined in general as

$$\mathbf{E} = \frac{1}{2}E e^{ikz-i\omega_0 t} + \frac{1}{2}E^* e^{-ikz+i\omega_0 t} , \quad (2.1)$$

with the electric field amplitude E , the wavenumber k , the frequency ω_0 and the time t . The polarization \mathbf{P} is defined equivalently. The starting point is the wave equation for an electric field \mathbf{E} which can be derived from the Maxwell equations under the assumption of non-magnetized media:

$$\frac{\partial^2 \mathbf{E}}{\partial z^2} - \frac{n_{\text{eff}}^2}{c^2} \frac{\partial^2 \mathbf{E}}{\partial t^2} = \mu_0 \frac{\partial^2 \mathbf{P}}{\partial t^2} . \quad (2.2)$$

n_{eff} is the refractive index, c the speed of light and μ_0 the magnetic permeability in vacuum. After simply inserting the electric field, the second-order terms can be neglected with the slowly varying envelope approximation under the assumption that P and E vary slowly compared to the frequency ω_0 . A rate equation for the electric field is obtained with a phenomenological added damping term [Oht12]:

$$\frac{\partial E}{\partial z} + \frac{n_{\text{eff}}}{c} \frac{\partial E}{\partial t} = \frac{ik}{2\epsilon_0 n_{\text{eff}}^2} P - \frac{n_{\text{eff}}}{2\tau_{\text{phot}} c} E . \quad (2.3)$$

ϵ_0 is the vacuum permittivity and τ_{phot} the photon lifetime. The electric field propagates in space and time and its derivation terms cannot be separated into two equations. The electric field induces a polarization in the cavity. The damping term describes the decay of the electric field with the photon lifetime τ_{phot} . τ_{phot} is essentially limited by the cavity emission and losses due to reabsorption and scattering.

The rate equation for the polarization is derived with the aid of the microscopic polarization and the definition of the polarization equivalently to equation 2.1. Fast oscillating

terms with $2\omega_0$ can be neglected with the rotating wave approximation. Including the phenomenologically added decay term, the rate equation reads

$$\frac{\partial P}{\partial t} = -i(\omega_A - \omega_0)P + \frac{i\mu^2}{2\hbar} E n - \frac{P}{\tau_{\text{pol}}} . \quad (2.4)$$

Here, $(\omega_A - \omega_0)$ gives the gain medium's detuning between the transition frequency ω_A and the laser frequency ω_0 . μ is the moment of the transition and τ_{pol} the polarization decay time. The polarization decays because of spin-dephasing and elastic collisions in the laser medium and restricts the decay time τ_{pol} .

The population inversion n is defined as the difference of the population in the upper and the lower energy state $n_u - n_{\text{gs}}$. The equation for the population inversion n can be derived as

$$\frac{\partial n}{\partial t} = -\frac{i}{\hbar} (E P^* - E^* P) + \frac{n_{\text{thr}} - n}{\tau_{\text{pump}}} . \quad (2.5)$$

n_{thr} is the population inversion at threshold and τ_{pump}^{-1} the pump rate.

The three general laser rate equations 2.3, 2.4 and 2.5 are also known as Maxwell-Bloch equations. With this system of three equations the dynamics of all kinds of conventional lasers can be described.

Laser Classes

The dynamics of a laser depends on the interplay of the three parameters for the decay times τ_{phot} , τ_{pol} and τ_{pump} . Regarding the dynamics, lasers are classified in class A, B and C by the relation of the time scales and weighting between the three components. The classification was introduced by Arecci et al. in [Are84] and a comprehensive overview is given in references [Oht12] and [Wie05].

- Class A lasers: $\tau_{\text{phot}} \gg \tau_{\text{pol}}, \tau_{\text{pump}}$. The rate equations can be simplified to a single equation for the electric field. The polarization P and the population inversion n follow the electric field amplitude E adiabatically. These lasers are very stable and dynamical effects do not occur. Some gas lasers with high quality factor Q , e.g. dye lasers or He-Ne lasers are classified to class A.
- Class B lasers: $\tau_{\text{phot}}, \tau_{\text{pump}} \gg \tau_{\text{pol}}$. The decay of the polarization P is fast compared to E and n . This reduces the system to two equations which offer two degrees of freedom. Periodical oscillations, so called relaxation oscillations, in E and n can

occur [All97], although the class B lasers are in general stable. They can become chaotic when external perturbations for instance through optical feedback or optically injected light add a third degree of freedom. Semiconductor lasers are class B lasers and the further discussion will be focused on this case.

- Class C lasers: τ_{phot} , τ_{pol} and τ_{pump} have similar orders. The rate equations 2.3, 2.4 and 2.5 cannot be simplified and the full model is used to describe the dynamics. The three degrees of freedom can lead to a chaotic behavior by themselves. Most optically pumped gas lasers fall in this category.

Semiconductor Lasers

In the previous description, the general interlevel radiative processes have been considered. Semiconductor lasers possess continuous energy bands. The radiative transition occurs from an electron in the conduction band to an unoccupied 'hole' state in the valence band.

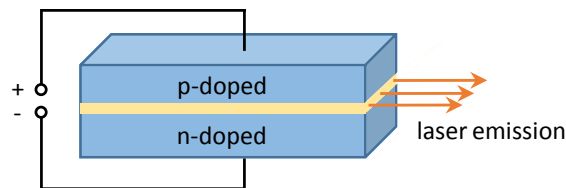


Figure 2.3: Sketch of a simple semiconductor laser. The p- and n-doped semiconductor with a space-charge region in between is driven in forward direction. The end-facets of the semiconductor partly reflect the light and build the laser cavity.

The intrinsic region at the p-i-n junction acts as active medium, where the population inversion is realized. The first, and most simple realization of a semiconductor laser, depicted in figure 2.3, is an edge-emitter with a p-n junction [Hal62, Nat62]. The difference of the refractive index between the semiconductor material ($n_{\text{GaAs}} \approx 3.6$) and air ($n_{\text{air}} \approx 1$) leads to a partial reflection of about 32 % according to Fresnel's law. Consequently, the cleaved facets of the semiconductor act as mirrors and build a Fabry-Pérot cavity.

A huge practical advantage of semiconductor lasers is the direct electrical excitation which explains the unprecedented success story of these opto-electronic devices. In fact the high optical gain combined with high-Q cavities enable a small and compact assembly which can be realized for a mass market with high yield in a cost efficient way. However, the first semiconductor lasers were pumped with electrical pulses and needed to be cooled

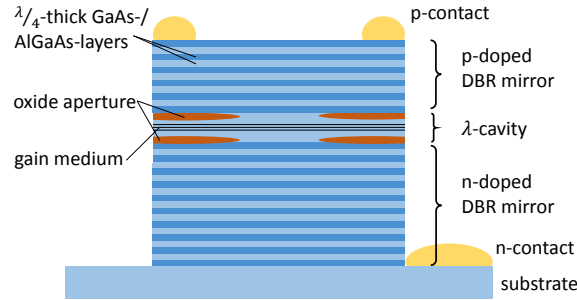


Figure 2.4: Device design of a VCSEL. $\lambda/4$ -thick alternating GaAs and AlGaAs-layers form a high reflective DBR-mirror. The λ -thick cavity includes an oxide aperture to guide the electrical current to the center of the active medium at the optical mode maximum. Multiple quantum wells are usually used as an active medium.

with liquid nitrogen. In 1963, Alferov and Kroemer had the noble prize winning idea of heterostructure lasers [Alf63, Kro63]. Thin layers of differently composed semiconductor material reduce the dimension of the space-charge region which increases the energy efficiency. This technique allowed for room-temperature lasing [Hay70].

The textbook 'semiconductor lasers' by Agrawal and Dutta [Agr13] is recommended for further details.

Vertical Cavity Surface Emitting Lasers

Particularly interesting for this thesis are vertical cavity surface emitting lasers (VCSEL). In edge-emitting semiconductor lasers the device emits along the space-charge region of the p-i-n-junction. In contrast, VCSELs emit vertically to it. The first kind of this laser was built in 1979 [Sod79].

The general device design of a VCSEL structure is depicted in figure 2.4. The active medium typically consists of a multiple quantum wells which are grown inside a λ -thick cavity. The cavity is sandwiched by high-reflective distributed Bragg reflector mirrors (DBR). Alternating $\lambda/4$ -thick layers of gallium arsenide (GaAs) and aluminum gallium arsenide (AlGaAs) feature a discontinuous change of the refractive index $n_{\text{AlGaAs/GaAs}}$. The reflected emission with the wavelength λ interferes constructively. The mirror reflectivity is [Agr13]

$$R = \left(\frac{1 - \left(\frac{n_{\text{AlGaAs}}}{n_{\text{GaAs}}} \right)^{2N}}{1 + \left(\frac{n_{\text{AlGaAs}}}{n_{\text{GaAs}}} \right)^{2N}} \right)^2 \quad (2.6)$$

and can exceed 99%. N is the number of mirror pairs. Importantly, the lower DBR-mirror possesses more mirror pairs than the upper DBR-mirror to ensure a directed emission to the top. The mirrors are p- and n-doped, respectively, for a good conductivity. An oxide structure guides the current to the central part of the VCSEL.

VCSELs are usually rotational symmetric which is advantageous for the radiation characteristic. The diameter is typically in the order of several μm up to $30\ \mu\text{m}$ [Eic15]. Applications of VCSELs are for instance in optical data communication and profit from high energy efficiency and compact on-chip device design. The fast modulation response makes them interesting for high bit rate data transmission in modern data centers. A new record for the modulation speed of 200 GHz has recently been realized by using VCSELs as spin-lasers [Lin19].

Linewidth Enhancement Factor α

In semiconductor lasers is the refractive index n_{eff} coupled to the carrier density N . This causes a coupling of the laser frequency to the carrier density N and effectively, fluctuations in the carrier density N broaden the emission linewidth. The effects are expressed by the linewidth enhancement factor α [Hen82]:

$$\alpha = \frac{\frac{\partial \text{Re}(n_{\text{eff}})}{\partial N}}{\frac{\partial \text{Im}(n_{\text{eff}})}{\partial N}} = -\frac{4\pi}{\lambda} \frac{dn_{\text{eff}}/dN}{dG/dN} \quad (2.7)$$

The real and imaginary parts of the refractive index n_{eff} change with the density of the charge carriers N . A variation of the refractive index n_{eff} influences the laser frequency. Typically, α has a value between 1 and 10 for semiconductor lasers [Wie05].

The α -factor is in particular important for the appearance of dynamical instabilities and indicates the laser's sensitivity to perturbations. Conversely, the α -factor can be determined by the responsivity to optical injection [Hol18].

Rate Equation Model

Semiconductor lasers are in general class B lasers where the polarization follows the electric field due to short polarization decay times τ_{pol} . The rate equations model (see equations 2.3, 2.4 and 2.5) can be simplified for semiconductor lasers to two equations. The electric field E is given by [Oht12]:

$$\frac{dE}{dt} = \frac{G}{2} (1 - i\alpha) (n - n_{\text{thr}}) \cdot E + \beta \cdot \frac{n}{\tau_{\text{sp}}} . \quad (2.8)$$

Here, the linewidth enhancement factor α is included as a gain specific parameter. G is the linear optical gain and n_{thr} is the population inversion at threshold. The population inversion above the laser threshold ($n - n_{\text{thr}}$) enables stimulated emission, specified by the first term. The term $E_{\text{sp}} = \beta \frac{n}{\tau_{\text{sp}}}$ describes the coupling of the spontaneous emission into the laser mode. τ_{sp} is the (Purcell enhanced) spontaneous emission lifetime in the upper energy level inside the cavity. In general, spontaneous emission is not directional. The β factor gives the probability that a spontaneously emitted photon is coupled into the cavity mode and is in particular important for microlasers operating in the regime of cavity quantum electrodynamics. This interesting aspect will be treated in detail later in this section.

The rate equation for the population inversion n under electrical carrier injection is [Oht12]

$$\frac{dn}{dt} = \frac{J}{e d} - \frac{n}{\tau_{\text{sp}}} - G(n - n_{\text{thr}}) E^2 . \quad (2.9)$$

Semiconductor lasers are almost exclusively pumped by electric current. The first term describes the dependence on the current density J and the extent of the active layer d in the propagation direction of the electric field. The second term expresses the spontaneous emission (in all directions) which reduces the carrier density. The third term reflects the stimulated emission which, in dependence of the gain G and the electric field amplitude E , lowers the population inversion.

Relaxation Oscillation Dynamics

Semiconductor lasers are per se stable in the lasing process because their dynamics is governed by two degrees of freedom (class B lasers). Importantly, a variation from the steady state in E or n leads to damped oscillations in both because the photon lifetime τ_{phot} is short compared to the radiative carrier lifetime τ_{sp} : After the turn-on of a semiconductor laser, the carrier density increases and eventually exceeds the threshold density. Above the threshold, the photon density and, therefore, E increases quickly and reduces the carrier density faster than the pump reoccupies the excited state. As a result, the photon density decreases because of insufficient gain and the carrier density increases again. These damped oscillations in E and n are called relaxation oscillations and are characterized by the damping Γ_{RO} and the oscillation frequency ω_{RO} [Oht12]:

$$\Gamma_{\text{RO}} = -\frac{1}{2} \left(G \cdot E^2 + \frac{1}{\tau_{\text{sp}}} \right) , \quad \omega_{\text{RO}} = \frac{1}{2\pi} \sqrt{\frac{G \cdot E^2}{\tau_{\text{phot}}} - \Gamma_{\text{RO}}^2} . \quad (2.10)$$

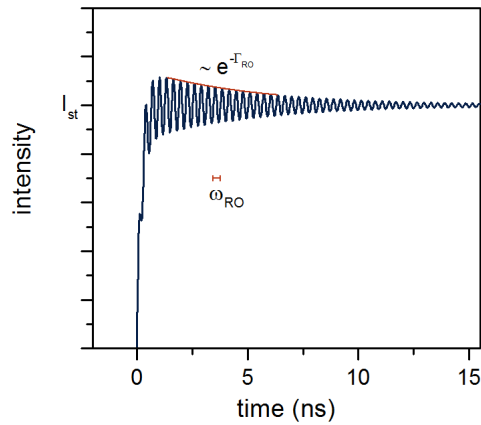


Figure 2.5: Exemplary relaxation oscillations of the intensity $I = |E|^2$ after the turn-on of a laser.

The oscillations are damped because of losses, mainly the laser radiation of the cavity. Consequently, long carrier lifetimes τ_{sp} reduce the damping and oscillations can occur for typically few ns up to tens of ns. The exemplary progress of the photon density Φ after a sudden turn-on at $t = 0$ is depicted in figure 2.5. Relaxation oscillations occur not only at the turn-on, but also after a perturbation from the steady state, e.g. via time delayed optical feedback, in the lasing regime. The RO frequency scales with the square root of the normalized pump which is proportional to the gain G . Typical frequencies are in the order of a few GHz [Oht12].

2.2 Quantum Dot Micropillar Lasers

In this thesis, quantum dot micropillar lasers are chosen for the experiments on nonlinear dynamics at ultra-small light levels usually well below $1 \mu\text{W}$. An introduction on the fundamental optical properties of microcavities, quantum dots (QD) as gain medium and QD micropillar lasers is given here, while the detailed structure and sample processing is presented in section 3.1.

Microlasers

Microlasers have small mode volumes on the order of the cubic wavelength which enhance the light-matter coupling and cavity quantum electrodynamics (cQED) gains importance in describing their optical properties. Different designs of microlasers have been successfully realized. QDs are often chosen as gain medium to benefit from their electronic density of state [Ara82]. They are implemented for instance in microdisk lasers [Slu93, Mic00], photonic crystal cavities [Str06] or micropillar lasers [Rei06]. Other examples of microlasers are plasmonic nanorods [Lu12], coaxial lasers [Kha12] or metallo-dielectrical lasers [Nez10].

Light-Matter Coupling

The effects of the cQED increase the spontaneous emission into the cavity mode for cavities with small mode volume. In the following, the effect for single emitters in a cavity is discussed.

An emitter in a cavity is influenced by the (vacuum) electrical field. The dipole moment d_{dm} and the electric field E characterize the coupling strength $g = |\langle d_{\text{dm}} \cdot E \rangle|$. In the 'strong coupling' regime of cQED $|\langle d_{\text{dm}} \cdot E \rangle| > |\nu_{\text{cav}} - \nu_{\text{QD}}|/4\hbar$ holds [And99], with the linewidth of the cavity mode ν_{cav} and the linewidth of the QD emission ν_{QD} . A periodic energy exchange between the emitter and the cavity, called Rabi oscillations, occurs. The cavity mode and the emitter in strong coupling form a 0D polariton.

The high accuracy needed for the spatial and spectral match of cavity and emitter energy are ambitious to realize for an ensemble of self-assembled quantum dots. In microlasers the emitters are usually in the 'weak coupling' regime and $|\langle d_{\text{dm}} \cdot E \rangle| < |\nu_{\text{cav}} - \nu_{\text{QD}}|/4\hbar$ [And99] applies.

The emitter couples to the vacuum fluctuations of the electrical field which reduces its spontaneous emission lifetime. The optical mode density is proportional to the quadratic frequency ω^2 in free space. The mode density increases for a low mode volume cavity at resonance and the spectral density is redistributed to a (narrow) Lorentzian distribution.

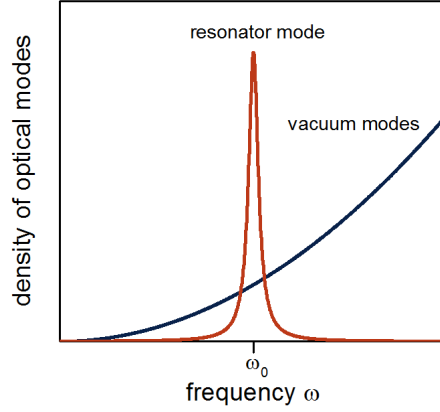


Figure 2.6: Density of optical modes of a cavity (red) and in vacuum (blue). The optical mode density of resonator mode has a Lorentzian shape while the density of modes increases quadratically in 3D.

As a result, the lifetime of a dipole-coupled emitter is reduced and consequently the emission in the cavity mode is enhanced while other emission, e.g. into leaky modes, gets suppressed [Bay01].

The lifetime reduction becomes relevant if the mode volume V_M of a laser is in the order of μm^3 . The mode volume V_M is the spatial dimension of the cavity mode, primarily limited by the cavity size. The ratio of the photon lifetime in bulk material and inside the cavity is defined as the Purcell factor $F_P = \frac{\tau_{\text{sp,bulk}}}{\tau_{\text{sp,cav}}}$. For a single emitter, F_P can be written as [Jah12]

$$F_P = \underbrace{\frac{3 Q \lambda_{\text{cav}}^3}{4\pi^2 n_{\text{eff}}^3 V_M}}_{F_{P,\text{max}}} \cdot \underbrace{\frac{(\nu_{\text{cav}}/2)^2}{(\nu_{\text{cav}}/2)^2 - \Delta_{\text{QD}}^2}}_{\text{spectral mismatch}} \cdot \underbrace{\frac{|\mathbf{E}_{\text{QD}}|^2}{|\mathbf{E}_{\text{max,cav}}|^2}}_{\text{spatial mismatch}}. \quad (2.11)$$

The first term is the maximal Purcell factor $F_{P,\text{max}}$ and depends on the Q factor, the mode wavelength λ_{cav} , the refractive index n_{eff} and the mode volume V_M . A small mode volume enlarges F_P . Highly reflective mirrors increase the Purcell factor via the quality factor Q . The two other terms specify the deviations from the optimum. The QD can be spectrally mismatched from the cavity. The spectral detuning Δ_{QD} has to be smaller than the half cavity linewidth ν_{cav} . A non-perfect overlap of the electric field from the QD \mathbf{E}_{QD} and the cavity $\mathbf{E}_{\text{max,cav}}$ caused by a spatial mismatch additionally reduces the Purcell factor.

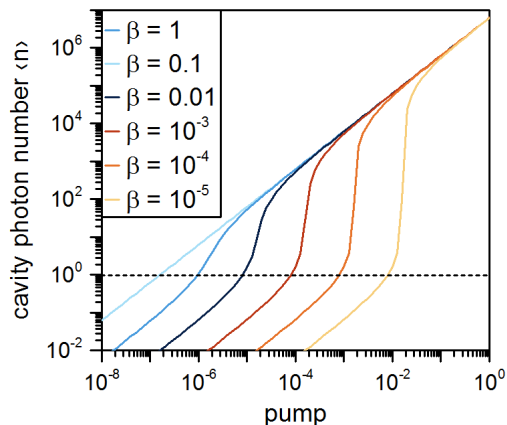


Figure 2.7: Input-output characteristics of laser with β factors between 10^{-5} and 1. The dashed line marks the cavity photon number of $\langle n \rangle = 1$ and the intersection with each line the respective laser threshold. The kink in the intensity and the threshold decreases with β and a straight line occurs for $\beta = 1$.

Spontaneous Emission Factor β

A reduction of the emitter lifetime in a cavity favors the emission into the cavity mode compared to any random direction. In this context, the β factor describes the fraction of the spontaneous emission into the cavity mode and is defined as the spontaneous emission rate in the cavity mode $\tau_{\text{sp,cav}}^{-1}$ divided by the total emission rate:

$$\beta = \frac{\tau_{\text{sp,cav}}^{-1}}{\tau_{\text{sp,cav}}^{-1} + \tau_{\text{sp,bulk}}^{-1}} = \frac{F_{\text{P}}}{F_{\text{P}} + 1} . \quad (2.12)$$

F_{P} is averaged over all contributing emitters. β can take values between 0 and 1 and reaches 1 in the limiting case of thresholdless lasing.

Below threshold, the intensity increases linearly with the pump. The intensity increases abruptly at the threshold for conventional low β lasers. Here, the spontaneous emission in the cavity mode is low and β is between $10^{-5} - 10^{-4}$. For a microlaser, the intensity characteristic differs strongly, dependent on the β factor (c.f. figure 2.7). At low pump powers, the intensity is mainly specified by the spontaneous emission and therefore increases for lasers with increasing β . The intensity kink at threshold 'smoothes' out with increasing β and a change in the intensity slope is not an adequate threshold definition anymore [Bjö94, Gie07]. As an alternative general definition for high- β microlasers, a cavity photon number of $\langle n \rangle = 1$ can be applied. The threshold is shifted to lower pump powers with increasing β .

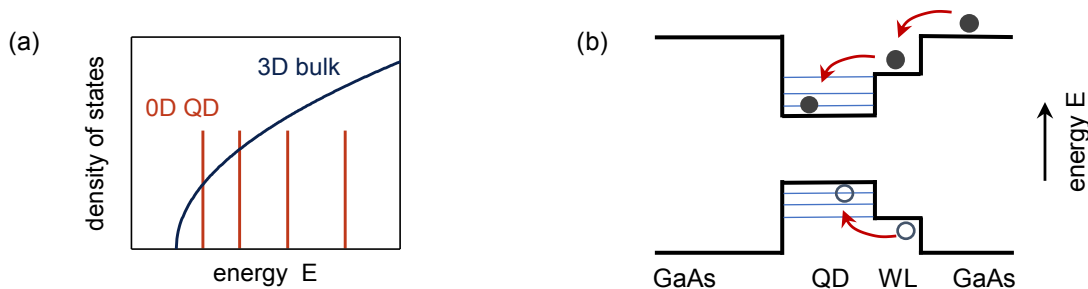


Figure 2.8: (a) Density of states for a 3D semiconductor of the form $D_{3D} \sim \sqrt{E - E_{\text{gap}}}$ and the discrete states of a QD. (b) Simplified sketch of an InGaAs QD within a GaAs matrix material in the energy band diagram. Charge carriers, electrons ● and holes ○, relax via phonon scattering via the WL into the QD.

In the limit of thresholdless lasing with $\beta = 1$, the complete spontaneous emission is coupled into the considered cavity mode. It is worth mentioning that lasing is not achieved below the limit of $\langle n \rangle = 1$ in the case of a thresholdless device. Then, a determination of the threshold is not possible by considering the intensity, but accessible with the measurement of the photon statistics.

Quantum dots

The active medium in the microlasers used for the experiments of this thesis consists of indium gallium arsenide (InGaAs) QDs. QDs are often described as 'artificial atoms' due to their discrete electronic energy levels [Mic09]. Quantum dots are nanocrystals which are typically fabricated by self-organized Stranski-Krastanov growth [Str37]. Thin layers of semiconductor material can be grown with molecular beam epitaxy or metalorganic chemical vapour deposition. The semiconductor matrix material is in our case gallium arsenide (GaAs) and InGaAs is grown on top. The lattice constants of InGaAs ($a_{\text{In}_x\text{Ga}_{1-x}\text{As}} = (5.65 + 0.4x) \text{ \AA}$) and GaAs ($a_{\text{GaAs}} = 5.65 \text{ \AA}$) differ up to 7%. Thus, growing InGaAs on GaAs results in strained InGaAs. After the growth of one or two monolayers of InGaAs, the strain relaxation leads to the formation of small 'islands', i.e. QDs of few nm in size. The thin formation layer of InGaAs is denominated as wetting layer. On top of the QDs, a capping layer of the matrix material (GaAs) is grown.

Due to the different bandgaps of GaAs and InGaAs charge carriers are confined in all three spatial dimensions in the QD. If the size of the QD is in the order of the de-Broglie wavelength, the density of states becomes discrete and the energy levels are discretized. The density of states for a 3D bulk semiconductor and a zero dimensional QD are shown in figure 2.8 (a). The energy states in the QD are analogous to the model of a harmonic

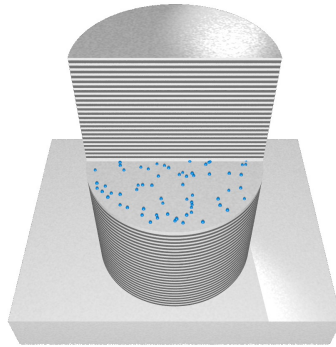


Figure 2.9: Sketch of a quantum dot micropillar laser. The active medium is a single layer of QDs (depicted in blue) centered between two DBR mirrors.

oscillator. In the energy band structure of a QD the electrons in the conduction band and the holes in the valence band relax from the matrix material in the wetting layer and thereafter in the QD upon non-resonant excitation as depicted in figure 2.8 (b).

Quantum Dot Micropillar Lasers

A sketch of a QD micropillar laser is shown in figure 2.9. The structure design has similarities with VCSELs which were presented in section 2.1. The cavity has a thickness of one λ and enables standing waves only for the fundamental longitudinal mode. Beneath and above the cavity distributed Bragg reflector mirrors (DBR) are located. Each layer is grown with a thickness of $1/4$ of the chosen cavity wavelength λ_{cav} , which is matched to the maximum gain medium amplification. The mirror reflectivity is very large with $R > 0.95$, calculated after [She95]. The typical mode volume of a QD micropillar laser is in the order of $V_M \sim \mu\text{m}^3$ [Ler13].

A single layer of QDs is grown in the middle of the cavity to maximize light-matter interaction with the optical mode. The QD-size and density can be controlled during the epitaxial growth via temperature, material quantity and composition [Bim99]. The QD-size and material composition alters the emission wavelength. Hence, the latter can be optimized for the desired laser characteristics. QDs enable quantum emitter properties, rendering QDs as good candidates as emitters for microlasers. Lasing was shown to be achieved with less than 100 QDs in the cavity and pronounced single-QD gain effects [Rei08b].

The first QD micropillar laser was presented in 2006 in optically excited samples [Rei06]. QD micropillars grown with p and n doped DBR mirrors, respectively, and an intermediate intrinsic cavity can be electrically pumped [Böc08]. The detailed structure of the used

sample will be discussed in section [3.1](#) and the optical mode characteristics in section [4.1](#).

2.3 Laser Dynamics under Optical Injection

Section 2.1 was devoted to the topic of laser characteristics and their description by rate equations. This section discusses the occurring dynamics when a semiconductor laser is subject to optical injection.

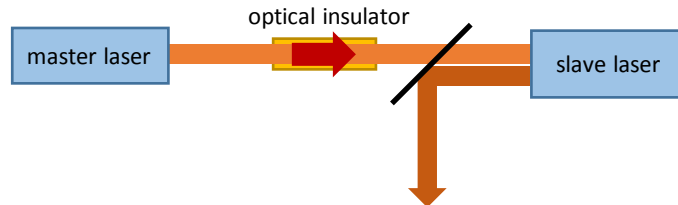


Figure 2.10: Principle of optical injection: A master laser is unilaterally coupled to a slave laser. In this case, the unilaterality is ensured by an optical insulator. The emission of the slave laser is studied.

The first experiments on optical injection were performed on gas lasers 1966 by Stover and Steier [Sto66]. They frequency-shifted a HeNe laser by varying the cavity length and injected its emission into a second HeNe laser at lower emission intensity. Phase-locking of the slave laser to the master laser was observed.

A widely used application of optical injection is the stabilization of (high power) lasers. Optical injection with a low power laser can stabilize the frequency and reduce the noise of the driven laser. A further application is found for multimodal lasers. Injection locking can pin the gain to a single mode [Oht12, Par08].

This section follows the discussions and notations in the books 'Laser dynamics' by T. Erneux and P. Glorieux [Ern10] and 'Semiconductor lasers: stability, instability and chaos' by J. Ohtsubo [Oht12] which are recommended for further details in this topic.

Adler Equation

Adler's equation was derived in 1946 to describe phase-locked radiofrequency oscillators [Adl46], but suits as a general description for externally driven oscillators like injected lasers. The classical Adler equation can be written as

$$\frac{d\Delta_\phi}{dt} = \Delta - a \sin(\Delta_\phi) \quad (2.13)$$

with the phase difference Δ_ϕ and the frequency difference $\Delta = \omega_0 - \omega_{inj}$ between the injected oscillator and the external master oscillator. a is the coupling strength. The relation between the coupling strength a and the detuning Δ is decisive for the affiliation

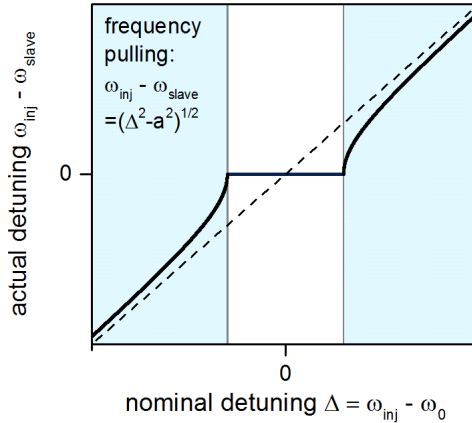


Figure 2.11: The actual detuning between drive and oscillator $\omega_{inj} - \omega_{slave}$ over the nominal frequency detuning $\Delta = \omega_{inj} - \omega_0$. The detuning without injection locking is drawn as dashed line. The oscillator is pulled towards the master (blue shaded area) and adapts its frequency inside the locking range ($|\Delta/a| \leq 1$, with the coupling strength a).

to the different locking regimes. If $|\Delta/a| \leq 1$, the injected oscillator adapts the master frequency. The slave is frequency-locked to the master and the phase difference Δ_ϕ is constant. For $|\Delta/a| \geq 1$, the phase difference Δ_ϕ is continuously increasing. The injected oscillator is not synchronized to the master, but the master pulls the slave oscillator's frequency ω_{slave} towards its own frequency ω_{inj} as depicted in 2.11.

Optical Injection in Semiconductor Lasers

In the previous section the laser rate equations for semiconductor laser were discussed for the electric field E and the population inversion n (c.f. equation 2.8 and 2.9). With optical injection, an additional term for the incident electric field of the master laser E_{inj} is added to the rate equation [Ern10]:

$$\frac{dE}{dt} = \frac{G}{2} (1 - i\alpha) (n - n_{thr}) \cdot E + \kappa \cdot E_{inj} \cdot e^{-2\pi i \Delta t} . \quad (2.14)$$

Two important parameters are introduced here. The injection strength κ is commonly defined as the square root of the fraction between master and slave intensity $\kappa = \sqrt{\frac{I_{inj}}{I_{slave}}}$. The detuning is the frequency difference between injected master laser and the slave laser $\Delta = \omega_{inj} - \omega_0$. The population inversion is affected by the modified electric field inside the cavity, but the description of the rate equation 2.9 does not change.

Considering the complex electrical field, the rate equation can be decomposed in equations

for intensity and phase Ψ . The rate equation for the phase is of the form [Oht12]

$$\underbrace{\frac{d\Psi}{dt}}_{\frac{d\Delta_\phi}{dt}} = \underbrace{-\tau_{\text{phot}}\Delta}_{\omega} - \underbrace{\sqrt{\frac{1+\alpha}{P_{>\text{thr}}}} \sqrt{\frac{\tau_{\text{sp}} \cdot G}{2}} \cdot \tau_{\text{phot}} \cdot E_{\text{inj}} \cdot \kappa}_{a} \cdot \underbrace{\sin(\Psi + \arctan(\alpha))}_{\Delta_\phi}. \quad (2.15)$$

G is the optical gain, τ_{phot} the photon lifetime, τ_{sp} the carrier lifetime, α the linewidth enhancement factor and $P_{>\text{thr}}$ the pump parameter above the threshold. The terms can be attributed to the terms of Adler's equation 2.13 as indicated by the braces. The phase difference is proportional to the detuning $\omega \sim \Delta$ and the coupling strength to the injection strength $a \sim \kappa$. Interestingly, the rate equation of a semiconductor laser under optical injection has the same form as the Adler equation.

By a linear stability analysis from the steady state of the rate equations, the locking range is calculated to be [Oht12]:

$$-\frac{\sqrt{1+\alpha^2}}{\tau_{\text{rt}}}\kappa \leq \Delta \leq \frac{1}{\tau_{\text{rt}}}\kappa, \quad (2.16)$$

with the round-trip time τ_{rt} of a photon inside the cavity. Inside the locking range, the slave is fully adapted to the master laser's frequency. The locking range increases linearly with κ and is asymmetric for negative and positive detuning due to the α -factor [Hen82]. The region outside the locking range is called 'four-wave mixing regime' [Nak85a, Len93]. There, the two separated frequencies of master and slave laser mix to higher-order contributions with the frequency $2 \cdot \omega_{\text{slave}} - \omega_{\text{inj}}$ (c.f. section 6.1). So far, the time scales of the relaxation oscillations have not been considered. The Adler equation for semiconductor lasers is valid for low detuning and injection rates $\eta \ll \omega_{\text{RO}} \sqrt{\frac{P_{>\text{thr}}}{1+\alpha^2}}$ with $\eta = \sqrt{\frac{\tau_{\text{sp}} \cdot G}{2}} \cdot \tau_{\text{phot}} \cdot E_{\text{inj}} \cdot \kappa$.

The slave laser frequency ω_{slave} outside the locking range can be approximated as [Ern10]

$$\omega_{\text{slave}} = \omega_0 + \frac{\tau_{\text{phot}}^2 P_{>\text{thr}}^2}{2\Delta (1+\alpha^2)} \quad (2.17)$$

and points out the frequency pulling of the laser frequency of the same form as depicted in 2.11.

Complex Dynamics Induced by Optical Injection

The numerical analysis of the rate equation 2.14 exhibits various regimes that can occur for semiconductor lasers under optical injection. An exemplary locking map for varied

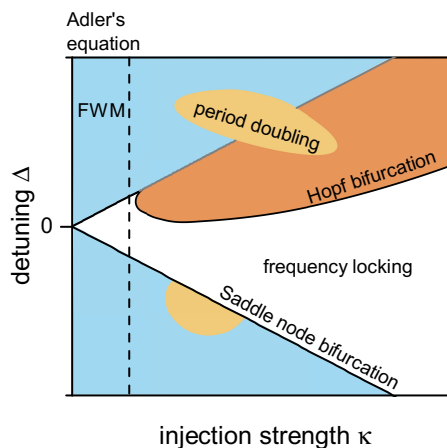


Figure 2.12: Schematic example of a semiconductor locking cone. A stability analysis for varied detuning Δ and injection strength κ can reveal regions of full frequency locking (white), no locking with frequency pulling (light blue), period doubling (yellow). The Adler equation is valid only for small κ .

detuning Δ and injection strength κ is shown in figure 2.12 to discuss some of the effects. For low κ , the slave laser is frequency-locked to the master laser inside the locking range (see eq. 2.16). Outside the locking range, the four-wave mixing region with frequency pulling (light blue) is located. With increasing κ , the Adler equation forfeits its validity. The frequency locked area is asymmetrically larger towards negative detuning where $\omega_{\text{inj}} < \omega_0$. At the edge of the locking region, bifurcation boundaries can be found analytically [Gav97].

A Hopf bifurcation occurs at the upper detuning boundary of the frequency locked region. The optical injection amplifies the relaxation oscillations and a transition from a stable (white) to an unstable state (orange) takes place. The slave laser can start to pulsate, periodically or chaotically. The yellow region marks a period-doubling of (periodical) oscillations. At the lower saddle-node bifurcation boundary, the slave laser experiences a transition from an unbounded state outside to a locked state inside the locking range. It is worth mentioning that other possible stabilities and bifurcations can occur [Ern10] and are not specified in this simplified sketch.

The device parameter for the linewidth enhancement α , the frequency of relaxation oscillations ω_{RO} and the pump parameter above threshold $P_{>\text{thr}}$ determine the arising effects and their location in the locking cone. In high- β microlasers, quantum noise is relevant and chaotic dynamics are diminished compared to conventional semiconductor laser [Wei91, Sat16].

For a further introduction on the locking cones of semiconductor laser in general, [[Wie05](#)] and [[Ern10](#)] are recommended. In particular for lasers with QDs as gain medium, [[Lüd12](#)] and [[Lin15a](#)] are suggested references.

2.4 Photon Statistics

In conventional low β lasers, the intensity is a simple and adequate measure to observe the onset of lasing and dynamical effects. Relaxation oscillations or injection induced dynamics like pulsing or chaotic behavior can be investigated with sufficiently fast photodetectors. Furthermore, the photon statistics of a light source can be explored if the temporal resolution of a detector is better than the coherence time of the emission. However, fast photodetectors with a GHz bandwidth have a low sensitivity and are insufficient to measure microlaser emission with a power in the order of 100 nW with suitably high time resolution. With the smooth transition to lasing and the high fraction of spontaneous emission (c.f. figure 2.7) it may stay uncertain if the device is a microlaser emitting coherent light or a bright nonlinear LED acting as thermal emitter [Kre17]. There exist no detectors with suitably high noise equivalent power to directly access the emission dynamics of high- β microlasers with sub- μ W emission power. In fact, dynamics appear on the time scale of the coherence time τ_{coh} which is at best in the order of GHz ($\tau_{\text{coh}} \approx \text{ns}$), making them inaccessible for a direct measurement with photodetectors.

Because of these reasons, the photon statistics of microlasers is of high interest. Common single photon detectors in the near infrared can be used for this purpose in HBT configuration. Another option is to use a faster streak camera, however at the cost of lower quantum efficiency. Typically, these two detector types are used for microlasers to determine the second-order autocorrelation as a measure of the photon statistics.

In this section, the statistics of thermal (chaotic) and coherent light sources is discussed, following the book 'Quantum optics' from Mark Fox [Fox06].

Coherent Light

Lasers are a source of coherent light. The electric field can be expressed as a plane wave propagating in z -direction by the frequency ω , the phase ϕ and the amplitude E

$$\mathbf{E}(x,t) = E \sin(kz - \omega t + \phi) . \quad (2.18)$$

Coherent light has no intensity fluctuations and a constant average photon flux. However, if a short time segment with a denumerable quantity of photons is considered and the losses are nonzero, the number of photons varies. The probability of n_{ph} photons $P(n)$ in a coherent beam segment of the length L with M subsegments is characterized by a

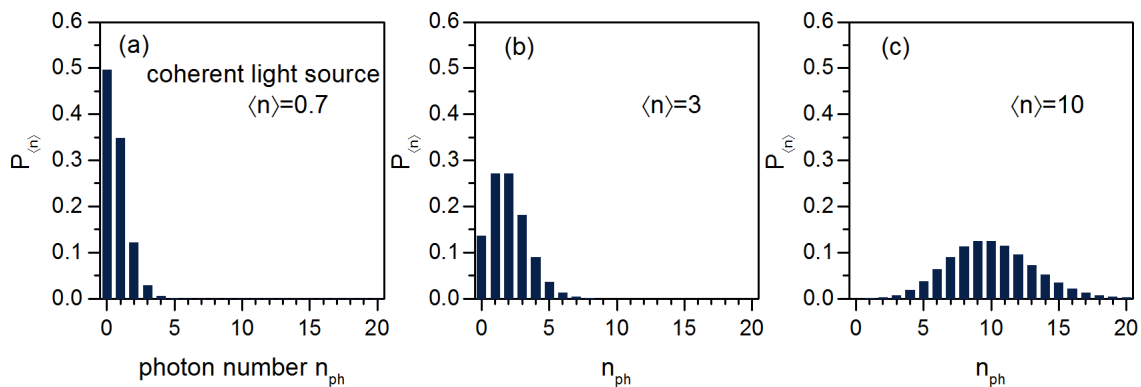


Figure 2.13: Photon number distribution of a coherent distribution after equation 2.20 for three different mean photon numbers $\langle n \rangle = 0.7$, 3 and 10.

binomial distribution:

$$P(n) = \frac{M!}{n_{\text{ph}}!(M - n_{\text{ph}})!} p^{n_{\text{ph}}} (1 - p)^{M - n_{\text{ph}}} . \quad (2.19)$$

p gives the probability to find one photon in a subsegment. From this equation, the Poissonian distribution can be derived for coherent light with constant intensity, i.e. with the mean photon number $\langle n \rangle$ as

$$P(n) = \frac{\langle n \rangle^{n_{\text{ph}}}}{n_{\text{ph}}!} e^{-\langle n \rangle}, \text{ with } n_{\text{ph}} \in \mathbb{Z} . \quad (2.20)$$

Despite the constant intensity, the photon number distribution (PND) is a distribution around the most probable state $\langle n \rangle$ (c.f. 2.13). With increasing mean photon number $\langle n \rangle$, the distribution broadens and becomes more symmetric around the maximum. For a Poisson distribution, the variance is exactly the mean photon number

$$\text{Var}(n_{\text{ph}}) = (\Delta n_{\text{ph}})^2 = \langle n \rangle \quad (2.21)$$

and subsequently the standard deviation is

$$\Delta n_{\text{ph}} = \sqrt{\langle n \rangle} . \quad (2.22)$$

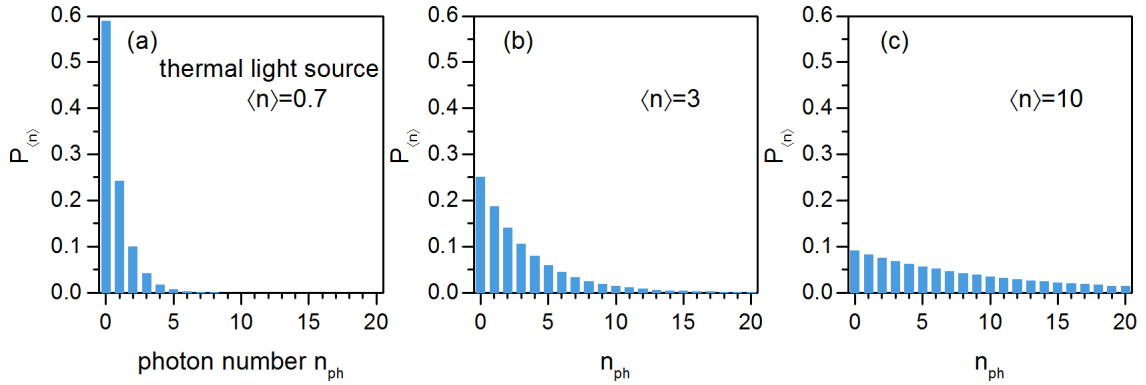


Figure 2.14: Thermal photon number distribution according to equation 2.25 for three different mean photon numbers $\langle n \rangle = 0.7$, 3 and 10.

Thermal Light

The term thermal light has its origin in the description of black-body radiation. Planck's law describes the energy density U_ω for the continuous spectrum emitted by an object of the temperature T within the frequency range $d\omega$:

$$U_\omega(T) d\omega = \frac{8\pi h \omega^3}{c^3} \frac{1}{e^{\left(\frac{h\omega}{k_B T}\right)} - 1} d\omega . \quad (2.23)$$

If only a single mode is contemplated, the probability of n photons in this mode is described by Boltzmann's law

$$P_{\text{ther}}(n) = \frac{e^{\left(\frac{-E_n}{k_B T}\right)}}{\sum_{n=0}^{\infty} e^{\left(\frac{-E_n}{k_B T}\right)}} , \quad (2.24)$$

where the energy in the mode is $E_n = (n + 1/2)\hbar\omega$. The equation has the form of a geometric series and can finally be approximated by the Bose-Einstein distribution

$$P_{\text{ther}}(n_{\text{ph}}) = \frac{\langle n \rangle^{n_{\text{ph}}}}{(\langle n \rangle + 1)^{n_{\text{ph}} + 1}} . \quad (2.25)$$

From the definition of the variance, it is derived to be

$$\text{Var}(n_{\text{ph}}) = (\Delta n_{\text{ph}})^2 = \langle n \rangle + \langle n \rangle^2 \quad (2.26)$$

and is obviously larger than for coherent light (c.f. equation 2.21).

The Bose-Einstein distribution is also called thermal distribution. Three examples for different mean photon numbers $\langle n \rangle$ are shown in figure 2.14 with the identical scaling as the previous figure for coherent emission. A thermal distribution features, independent of $\langle n \rangle$, the highest probability for the zero-photon state and decays exponentially with n_{ph} . Interestingly, for a low mean photon number $\langle n \rangle$, the distribution of coherent and thermal emission (c.f. figure 2.13 (a) 2.14 (a)) do not differ considerably to the eye. With increasing $\langle n \rangle$, the extension for higher photon numbers n_{ph} is enlarged. The intensity fluctuations arise on the time scale of the coherence time τ_{coh} [Lou00].

An interesting example for a thermal emitter is the sun. Also, for sun radiation it is most likely to find zero photons. However, the precondition is a measurement within the coherence length which is only in the order of fs for the broad sun spectrum [Hec98] and explains why this character appears unintuitive to the most. Single light modes of light bulbs or LEDs possess a thermal photon number distribution.

Calculation of the Autocorrelation

An important quantity of photon statistics is the second-order autocorrelation function. It is defined by

$$g^{(2)}(\tau) = \frac{\langle I(t) I(t + \tau) \rangle}{\langle I(t) \rangle \langle I(t + \tau) \rangle} . \quad (2.27)$$

The correlation of the intensity at the time t and after an additional time delay τ is normalized by the mean value of both. For classical light sources $g^{(2)}(0) \geq 1$ and $g^{(2)}(0) \geq g^{(2)}(\tau)$ [Lou00] holds.

Non-classical light sources can exhibit $g^{(2)}(0) \leq 1$. For instance, single-photon sources emit only one photon at a time. Consequently, the correlation for zero time delay $\tau = 0$ vanishes and $g^{(2)}(0) = 0$ applies [Mic00].

A coherent light mode does not suffer from intensity fluctuations leading to

$$g_{\text{coh}}^{(2)}(\tau) = \frac{\langle I(t) I(t + \tau) \rangle}{\langle I(t) \rangle \langle I(t + \tau) \rangle} = \frac{I^2}{I^2} = 1 . \quad (2.28)$$

For thermal light sources with zero-time delay follows from the variance

$$g_{\text{ther}}^{(2)}(0) = 2 . \quad (2.29)$$

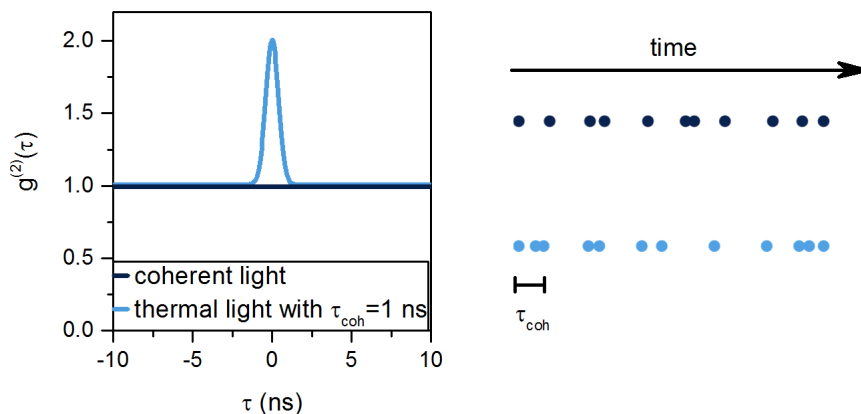


Figure 2.15: Second-order autocorrelation function $g^{(2)}(\tau)$ of coherent light (dark blue) and thermal light (light blue) with a coherence time of $\tau_{\text{coh}} = 1$ ns. The coherent emission is uncorrelated in time while the thermal emission is bunched.

For spectrally Gaussian shaped light, the time dependent second-order autocorrelation is derived as [Lou00]

$$g_{\text{ther}}^{(2)}(\tau) = 1 + e^{\left(-\pi\left(\frac{\tau}{\tau_{\text{coh}}}\right)^2\right)}. \quad (2.30)$$

The second-order autocorrelation $g^{(2)}(\tau)$ for coherent and thermal emission is depicted in figure 2.15. The coherent light reveals a flat $g^{(2)}(\tau)$ independent of the time, being synonymous with no fluctuations of the emission. $g^{(2)}(\tau) > 1$ is called bunching and implies that the emitter is likely to emit another photon after the emission of one photon. A thermal light source shows photon bunching on the time scale of the coherence time τ_{coh} . The measurement of $g^{(2)}(\tau)$ via a Hanbury-Brown and Twiss configuration will be presented in the experimental methods in section 3.3.

In addition to measurements with a Hanbury-Brown and Twiss configuration, the autocorrelation at zero time delay of arbitrary order $g^{(k)}(0)$ can be calculated from the photon number distribution $P(n)$. The autocorrelation for the k -th order is given by [Bar02, Mig13]

$$g^{(k)}(0) = \frac{\sum_{n_{\text{ph}}=1}^{\infty} \prod_{i=0}^{k-1} (n_{\text{ph}} - i) P_n}{\left(\sum_{n_{\text{ph}}=1}^{\infty} n_{\text{ph}} P_n\right)^k}. \quad (2.31)$$

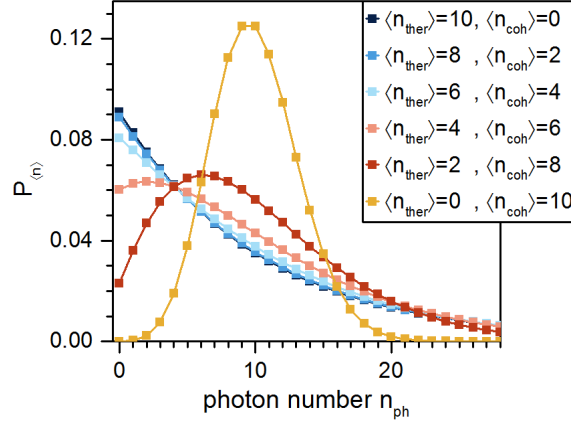


Figure 2.16: Photon number distribution of thermal-coherent superposition state after equation 2.33 for various mean photon numbers $\langle n_{\text{ther}} \rangle$ and $\langle n_{\text{coh}} \rangle$. The total photon number is fixed to $\langle n \rangle = \langle n_{\text{ther}} \rangle + \langle n_{\text{coh}} \rangle = 10$.

For the second-order, the formula can be simplified to

$$g^{(2)}(0) = \frac{\sum_{n_{\text{ph}}=1}^{\infty} n_{\text{ph}}(n_{\text{ph}} - 1)P_n}{\left(\sum_{n_{\text{ph}}=1}^{\infty} n_{\text{ph}}P_n\right)^2} = \frac{\langle n^2 \rangle - \langle n_{\text{ph}} \rangle}{\langle n \rangle^2} = \frac{(\Delta n)^2}{\langle n \rangle^2} \quad (2.32)$$

and depends solely on the mean photon number $\langle n \rangle$ and the variance $(\Delta n_{\text{ph}})^2$ of the photon number distribution. The higher orders depend on the k -th moment of the distribution and are simple to calculate with knowledge of $P(n)$.

Superposition States of Coherent and Chaotic Emission

The emission of a microlaser driven close to the threshold is not purely thermal, but also not fully coherent. The photon number distribution of such a transition state can be described by a mixture of a thermal and a Poissonian distribution. The single photons of such a beam can be regarded as either thermal or coherent. The resulting photon number distribution for a superposition of the fields is of the form [Are66]:

$$P_{\text{superp}}(\langle n_{\text{ther}} \rangle, \langle n_{\text{coh}} \rangle, n_{\text{ph}}) = \frac{\langle n_{\text{ther}} \rangle^{n_{\text{ph}}}}{\langle n_{\text{ther}} + 1 \rangle^{n_{\text{ph}}+1}} \cdot L_{n_{\text{ph}}} \left(\frac{-\langle n_{\text{coh}} \rangle}{(1 + \langle n_{\text{ther}} \rangle)\langle n_{\text{ther}} \rangle} \right) \cdot e^{-\frac{\langle n_{\text{coh}} \rangle}{(1 + \langle n_{\text{ther}} \rangle)}} \quad (2.33)$$

The equation depends on the mean photon number of the thermal part $\langle n_{\text{ther}} \rangle$ and the coherent part $\langle n_{\text{coh}} \rangle$ which also gives a weighting between both distributions. $L_{n_{\text{ph}}}$ is the

Laguerre polynomial of the n_{ph} -th order.

Exemplary photon number distributions are illustrated in figure 2.16. For a large fraction of thermal emission ($\langle n_{\text{ther}} \rangle > \langle n_{\text{coh}} \rangle$), the distribution appears close to a thermal state. With increasing fraction of coherent light, the highest probability shifts to higher photon numbers n_{ph} . With a relevant thermal fraction, the distribution has a longer 'tail' for high photon numbers compared to the pure coherent case.

3 Experimental Methods

In this chapter, the fabrication of microlaser samples and experimental methods are described. The layer design of both kinds of samples, quantum dot micropillars and exciton-polariton micropillars, is discussed in section 3.1. The micro-electroluminescence and -photoluminescence setup and the utilized components are introduced in section 3.2, followed by a description of the experimental methods to measure the photon statistics in section 3.3.

3.1 Sample Fabrication

Quantum Dot Micropillar Lasers

Within this thesis, two QD micropillar laser samples are investigated. The samples were grown and processed at the University of Würzburg [Rei06]. The investigated samples are piece 11.6 of wafer M4072 (sample A) and piece 21.15 of wafer M2977 (Sample B). The epitaxial growth process of both samples is similar, but because of a different layer composition the QD micropillars of sample A emit at 850 nm, while the QD micropillars of sample B show emission at 900 nm. The layer design is depicted as table in the appendix A.

The samples are grown on GaAs substrate by molecular beam epitaxy (MBE). The layer design is shown in figure 3.1. First, a GaAs buffer layer (300 nm) optimizes the growth quality and enables defect free growth. Second, the lower distributed Bragg reflector (DBR) mirror is grown. The DBR structure is composed of alternating layer pairs of AlAs and GaAs. Each layer has an optical thickness of $\lambda_{\text{cav}}/4$ for the desired wavelength. The bottom DBR has 26 layer pairs.

The gain medium consists of InGaAs QDs which are grown in the center of the one- λ_{cav} thick GaAs cavity. The upper DBR consists of 23 layers, where the asymmetric DBR design ensures directional emission to the upper direction. The final layer is composed of GaAs to prevent oxidation of the AlAs. Both DBRs are doped to allow for electrical carrier injection. The substrate and the lower DBR are n-doped with a decreasing density from 3 to $1 \cdot 10^{18} \text{ cm}^{-3}$ towards the intrinsic GaAs cavity. The upper DBR is p-doped

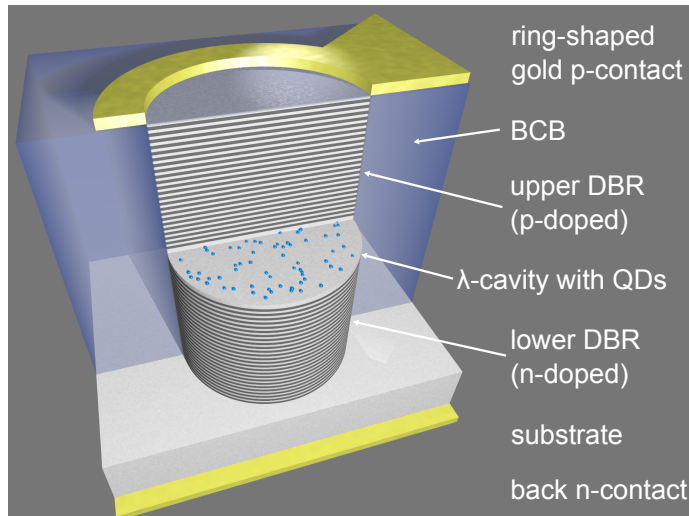


Figure 3.1: Schematic 3D image of a QD micropillar laser. The active medium consists of InGaAs QDs and is embedded in the center of a λ_{cav} -thick cavity in between two DBR mirrors. The pillars are surrounded by BCB where the ring-shaped gold p-contact sits. On the bottom side, the GaAs substrate is contacted with a gold back n-contact.

with a density from 1 to $2 \cdot 10^{19} \text{ cm}^{-3}$ increasing with the distance from the GaAs cavity. At each GaAs/AlGaAs interface, i.e. at the electric field nodes, δ -doping of $1 \cdot 10^{12} \text{ cm}^{-3}$ is implemented to reduce the electrical resistance.

After the growth process, electron beam lithography and plasma etching are used to fabricate the micropillar structure. In the first step, PMMA is deposited on the sample acting as resist. With electron beam lithography circular shapes are structured in the resist which is removed at the patterned position in the development step. Subsequent, a layer of nickel is evaporated on the surface and the residual PMMA is removed with ultrasonics in a lift-off step. Only the circular nickel structures remain on the sample surface and build the etch mask. Finally, the micropillars are structured by reactive-ion etching (ECR-RIE).

Freestanding micropillars cannot be easily contacted. For this reason, the electrically driven micropillar sample first is planarized with benzocyclobutene (BCB), which is electrically isolating and optically transparent, but mechanically stable. Afterwards, ring-shaped gold p-contacts are deposited around the upper micropillar facet via a second electron beam lithography step. A triangular contact links the gold ring with a larger pad for gold bonding. Additionally, a planar gold n-contact is vapedored on the back surface of the sample. For further details on the structuring of QD micropillars the references [Böc08, Lö8] are recommended.

Scanning electron microscope (SEM) images in figure 3.2 show the fully processed sample. Each sample part includes contact pads which can be addressed by gold wire bonding to

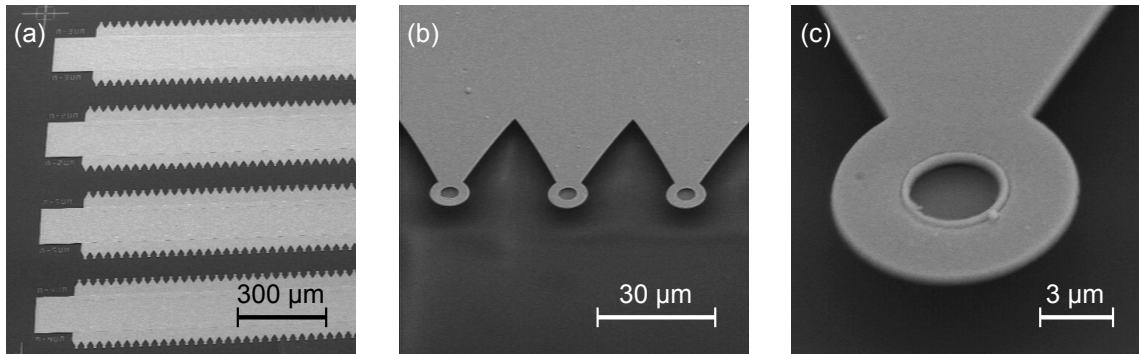


Figure 3.2: SEM image of the QD micropillar sample B. (a) Overview image of the sample. The squares on the left side can be electrically contacted by wire bonding. (b) The zoom-in image shows the configuration of three QD micropillars. (c) Top contact of a QD micropillar with 4 μm diameter. *With courtesy of Monika Emmerling, Technische Physik Würzburg*

enable current injection. One pad contacts 120 pillars in parallel, 60 on each side. Panel (c) shows a zoom-in view of the ring-shaped upper gold contact with the micropillar in the middle which is enclosed by BCB. QD micropillars with 4 and 5 μm diameter are chosen for the experiments.

Exciton Polariton Laser

The measurements presented in section 5.3 are performed with a different class of microcavities which includes 12 layers of GaAs quantum wells (QW) as gain medium. Similar to the previous structures micropillars are patterned on the planar microcavity.

The DBR mirrors of this sample are formed by alternating $\lambda_{\text{cav}}/4$ -layers of $\text{Al}_{0.2}\text{Ga}_{0.8}\text{As}$ and AlAs. The lower DBR has 27 and the upper DBR 23 mirror pairs. The active medium is built of 12 layers of 13 nm thick GaAs QWs. Four of these QWs are placed in a $\lambda_{\text{cav}}/2$ -thick $\text{Al}_{0.2}\text{Ga}_{0.8}\text{As}$ cavity. Four are located in the first upper and four in the lower mirror pair, respectively, to ensure that the active medium is located in the optical antinodes of the electromagnetic field in the cavity for maximum light-matter interaction. The Q-factor is measured to be around 12,000. For the presented experiments, a pillar of 6 μm diameter is selected.

3.2 Micro-Electroluminescence and -Photoluminescence

The experimental setup used for all experiments in this thesis is depicted in figure 3.4. The sample is mounted in a continuous-flow He cryostat (top left corner). With a turbopump (model: HiPace[®]80 from Pfeiffer Vacuum) the sample space is evacuated to 10^{-6} mbar,

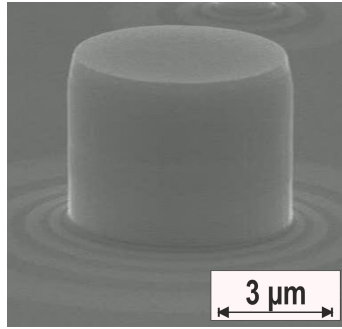


Figure 3.3: SEM image of a QW micropillar with 6 μm diameter (taken from [Kla18b])

which enables an effective sample cooling by a constant flow of liquid helium with a base temperature of 5 K. The optical adjustment of the cryostat to specific QD micropillar lasers is performed by two perpendicularly installed motorized linear stages (model: M-413.1DG from Physik Instrumente).

The electrical contact on the QD micropillar sample addresses 60 micropillars in parallel for the measurements presented in the first part of chapter 6 and 120 for chapter 5 and the second part of chapter 6. The applied injection current is divided by the number of contacted micropillars to estimate the effective current per microlaser (under the assumption that each contact is operational). Electrical excitation is realized by either the constant voltage of a precision source/measurement unit (model: B2902 A from Agilent Keysight), used for continuous wave (CW) experiments in chapter 6 or by a pulse generator (model: 8131A from Hewlett Packard), used in the case of pulsed experiments in chapter 5.

The QW polariton laser sample is optically excited by a Ti:sapphire laser (model: 3900 S Ti:Sa from Spectra-Physics) with broadband optics (not shown in figure 3.4). The laser has a fixed repetition frequency of 80 MHz and emits at 748 nm. For experimentally applying a transition-edge sensor, the repetition frequency is reduced by pulse picking to 10 kHz. This technique is further described in section 5.3.

A collimating lens with a numerical aperture $\text{NA} = 0.5$ or alternatively a microscope objective with $\text{NA} = 0.4$ (model: Plan Apo NIR B 20x from Mitutoyo) is used to collect the emission of the microlaser under study. A linear polarizer in front of the entrance slit, represented by a polarizing beam splitter (PBS), is fixed to the monochromator axis with fewer losses. A motorized $\lambda/2$ waveplate is utilized to align the linearly polarized mode of the emitter on the transmission axis of the linear polarizer / PBS.

Since multiple micropillars are excited simultaneously, a pinhole configuration is used to spatially filter the emission of single micropillars. Here, two achromatic lenses ($f = 10\text{ cm}$) focus and re-collimate the beam. The pinhole with a diameter of 50 μm or 100 μm allows

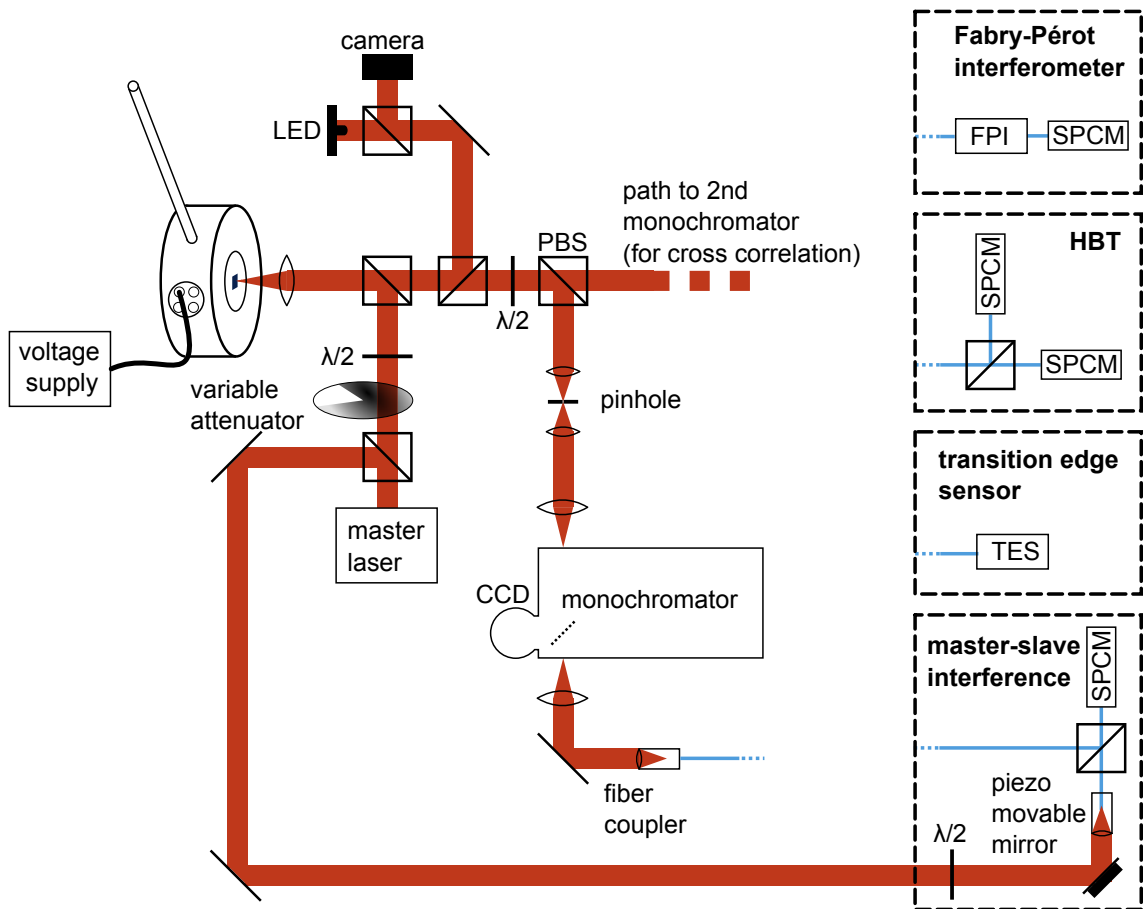


Figure 3.4: Schematic view of the experimental setup. The sample is placed in a cooled cryostat and is electrically excited. The emitted signal is spectrally filtered by a monochromator and can be analyzed by either a CCD, a Fabry-Pérot interferometer, a HBT configuration or a transition-edge sensor based photon number resolving detection system. For optical injection experiments a master laser is directed on the sample and additionally, the master-slave interference can be examined.

one to detect only emission of the chosen micropillar.

A monochromator (model: SP-2750 from Princeton Instruments) with a focal length of 75 cm is used as dispersive element. To obtain a high-resolution micro-electroluminescence or -photoluminescence spectrum with the attached CCD camera (model: PIXIS 400BR from Princeton Instruments), a grating of 1500 lines/mm is chosen, which provides a spectral resolution $27 \mu\text{eV} \cong 6.5 \text{ GHz}$. For fiber-coupled experiments, a grating with 300 lines/mm, leading to a spectral resolution of $170 \mu\text{eV} \cong 41 \text{ GHz}$, is chosen for a higher light throughput.

After the passage through the monochromator, the optical signal is coupled into an optical fiber. Dependent on the application a multi-mode or a polarization-maintaining single

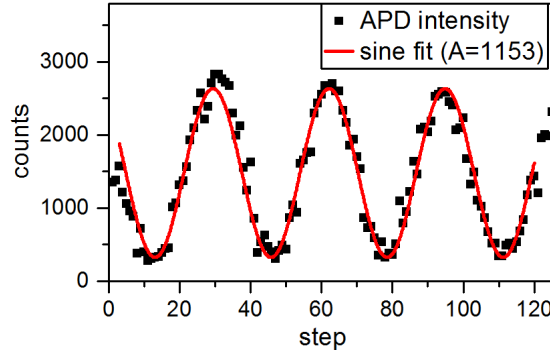


Figure 3.5: Exemplary measurement of the slave’s phase-locking to the master laser. The intensity, measured by an SPCM, is plotted for every step (~ 35 nm) of the piezo-movable mirror. The data is fitted with a sine function and the amplitude A quantifies the phase locking.

mode fiber is chosen. Fiber coupling allows for measuring the optical spectrum in high resolution by a Fabry-Pérot interferometer with a free spectral range of $31 \mu\text{eV} \cong 7.5$ GHz and a resolution of $0.41 \mu\text{eV} \cong 100$ MHz corresponding to a finesse $\mathcal{F} = \frac{\nu_{\text{FSR}}}{\nu_{\text{FWHM}}} = 75$. The measurements with a HBT and TES are described in section 3.3.

Optical Injection

A master laser is included in the setup to investigate the influence of external optical perturbations to the QD micropillar laser acting as slave (c.f. 3.4). The two QD micropillar samples are optimized for different wavelengths and require the use of different master lasers. As master laser in section 6.1 an external cavity laser (model: TEC-520-0850-080 from Sacher Lasertechnik) with a tuning range of 830 – 850 nm, a linewidth $\nu_{\text{FWHM}} < 100$ kHz and a maximum output power of 80 mW is used. For the measurements presented in section 6.2, an external cavity diode laser (model: DL 100 from Toptica) with a tuning range of 875 – 940 nm and a maximum output power of 40 mW is applied.

Built-in optical isolators in the master laser heads assure that no emission from the slave laser (QD micropillar laser) is injected into the master laser. Besides, the emission power of the slave laser is more than four orders of magnitude lower than that of the master laser and additionally 90 : 10 beamsplitter and a neutral density filter are in the beam path. Because of this experimental configuration we can rule out that the slave laser or self-reflection can perturb the master laser.

The injection power is monitored by a power meter and controlled by a neutral density filter wheel with an optical attenuation of 0 – 10 dB (or 0 – 40 dB), depending on the filter angle. A $\lambda/2$ wave-plate is used to turn the polarization angle of the linearly polarized

master laser to the target microlaser modes.

A Mach-Zehnder configuration allows us to examine the phase locking between master and slave laser. In front of the variable attenuator, a beamsplitter directs 10 % of the master laser emission, which a piezo-movable mirror modulates with a fixed frequency (~ 50 Hz), to an optical fiber. The second input arm of the Mach-Zehnder is fed by the slave laser emission after passing the monochromator. The master-slave interference signal is measured by a single-photon counting module (SPCM). Because of the fixed frequency modulation, the interference signal has a sinusoidal shape in time (figure 3.5) where the amplitude yields the phase locking strength.

3.3 Measurement of Photon Statistics

The photon statistics of the microlasers are analyzed by three different methods. The conventional Hanbury-Brown and Twiss (HBT) configuration is used to determine the second-order autocorrelation and cross-correlation function $g^{(2)}(\tau)$. The direct observation of time traces from the QD micropillar modes is accessible with a streak camera which allows us to distinguish statistical fluctuations from mode switching. A transition-edge sensor (TES) gives access to the number of photons in a pulse. It is applied to estimate the histogram of the photon-numbers which reflect the full photon number distribution (PND).

Time Correlation Experiments: Hanbury-Brown and Twiss and Cross-Correlation

The HBT configuration was developed in 1954 and was first used to measure the distance between two stars [HB56]. With SPCMs acting as detectors, this configuration can determine the second-order autocorrelation function $g^{(2)}(\tau)$ of light sources.

As indicated in figure 3.4, the HBT is integrated to the experimental setup in the second box on the right-hand side. After spectral filtering and the coupling to an optical fiber, the signal is split into two equal parts and the two output ports are connected to SPCMs. The chosen multi-mode fibers have a length of 25 m each to temporally shift the SPCM crosstalk by 160 ns. Crosstalk between the detectors is induced by the emission of photons from a SPCM after a detection event and the subsequent carrier avalanche. The two SPCMs (model: ID100-MMF50 from idQuantique) have a temporal resolution of $\tau_{\text{SPCM}} = 40$ ps which leads to a temporal resolution $\sqrt{2} \cdot \tau_{\text{SPCM}} = 56$ ps of the HBT configuration. Single-photon correlation electronics (model: quTAU from qutools) stores the time stamp of photon detection events and allows one to calculate $g^{(2)}(\tau)$.

The figures of merit of such measurements are usually the autocorrelation value at zero

time delay $g^{(2)}(0)$ and the correlation time τ_{cor} . These are obtained by fitting the measured $g^{(2)}(\tau)$ with the theoretical formula $g^{(2)}(\tau) = 1 + (g^{(2)}(0) - 1) \cdot e^{-|\frac{\tau}{\tau_{\text{cor}}|}$ folded by a Gaussian function with the full width half maximum (FWHM) of the time resolution and directly returns the desired values.

In case of cross-correlation measurements, the PBS splits the signal in two linearly polarized components. Each is spectrally filtered by a monochromator and detected by a SPCM. The arrival time of photons in both SPCMs is correlated to estimate $g^{(2)}(\tau)$ analog to the autocorrelation.

Streak Camera

A streak camera is an optical detector for the measurement of fast processes. A monochromator is part of the streak camera and spatially segments the spectral contributions of an optical signal. After the monochromator, a photocathode absorbs the impinging photons and releases electrons which are accelerated by an electrical potential. A modulated transverse electrical potential deflect the electrons dependent on their temporal arrival. The electrons impinge on a 2D phosphor screen and a CMOS camera digitalizes the signal. In single shot operation the spectrum is mapped on one axis of the CCD and the time on the second axis to create 2D maps. The temporal resolution of the streak camera (model: C10910 from Hamamatsu) is $\tau_{\text{res}} = 1$ ps with a quantum efficiency of the detector at 850 nm of $\eta = 0.73\%$ (c.f. chapter 5). A reasonable number of counts per time segment is required for an analysis of the time traces. This limits the significant temporal resolution to 10 ns in a 2 μs window for QD micropillars with an output power around 1 μW .

The streak camera also allows us to study correlations between the emission of the two linearly polarized components of the fundamental mode of a QD micropillar laser. The energy splitting between these two modes is usually much lower than the spectral resolution of the streak camera's spectrograph of about 290 GHz. To overcome this issue, a Wollaston prism is introduced in front of the monochromator to spatially split the two polarization modes and distinguish both on the measured map. This has the additional advantage that the spectrograph can be used in zero order which reduces the optical losses.

Transition-Edge Sensor

The photon number distribution (PND) provides full insight into the photon statistics. For devices with sufficiently emission power (\gg noise-equivalent power), the PND can in principle be determined by a fast photodiode with a temporal resolution faster than the emitter's coherence time. In contrast, the emission power ~ 1 μW of nanophotonic devices is usually not sufficient for the measurement with a photodiode with an adequate time

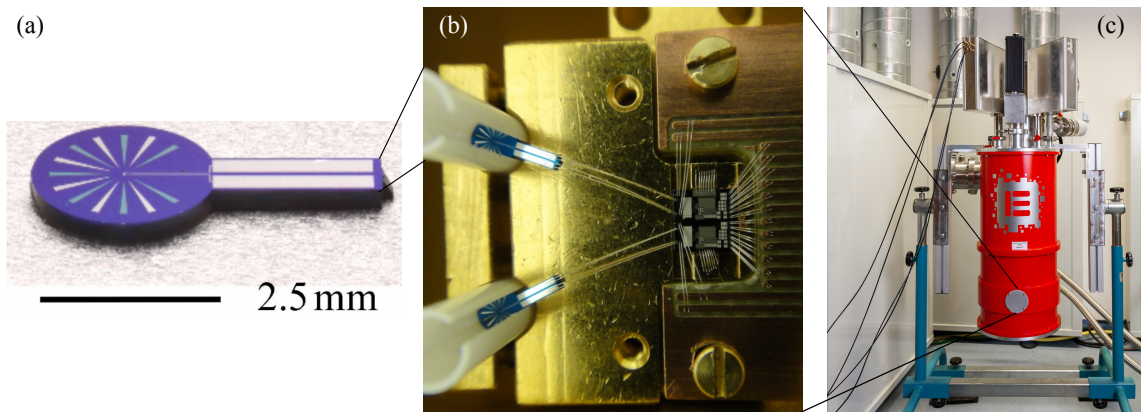


Figure 3.6: (a) The superconducting transition-edge sensor is centered in a circular shaped substrate. Taken from [Mil11] ©2011 Optical Society of America (b) The light is coupled via a single-mode optical fiber to the sensor whose two contacts are bonded to a read-out SQUID. Taken from [DE14] (c) The corpus contains four stages of cooling. ©TU Berlin/PR/Felix Noak

resolution in the order of ns.

In the presented work a photon-number-resolving transition-edge sensor (TES) is used to determine the PND of nanophotonic devices for the first time. A TES is an extremely sensitive calorimetric detector which can identify the number of photons in an optical pulse [Mil03]. These detectors have quantum efficiencies close to unity ($\eta \approx 95\%$ [Lit08]) and photon-number-resolving capability up to tens of photons in a light pulse. More details on TES detectors can be found in references [Irw05, vH17, Sch18c].

The non-commercial detectors which are operated in close collaboration with the Physikalisch-Technische Bundesanstalt Berlin (group of Dr. Jörn Beyer) are placed onto the cold stage of a cryo-free adiabatic demagnetization refrigerator (ADR) pre-cooled by a two-stage pulse tube cooler (first stage at 50 K, second stage at 3 K). A two stage paramagnetic salt pill unit provides base temperatures lower than 50 mK. The cryostat is constructed in a top-down principle. The innermost stage regulates the detector module at $100.000 \text{ mK} \pm 15 \mu\text{K}$.

The TES detector is cooled below its critical temperature $T_{\text{crit}} \approx 150 \text{ mK}$. A constant bias voltage holds the working point at the phase transition between superconducting and normal state. In this situation, the absorption of a photon changes the current through the sensor in the order of $0.1 \mu\text{A}$. The current change depends on the energy in the detected pulse and thereby on the number of absorbed photons and their wavelength. The TES circuit is inductively coupled to a direct current superconducting quantum interference device (SQUID) current sensor to transfer the small current change ($\sim 100 \text{ nA}$) to a voltage change ($\sim 100 \text{ mV}$) that can be measured by data acquisition systems with a suitable

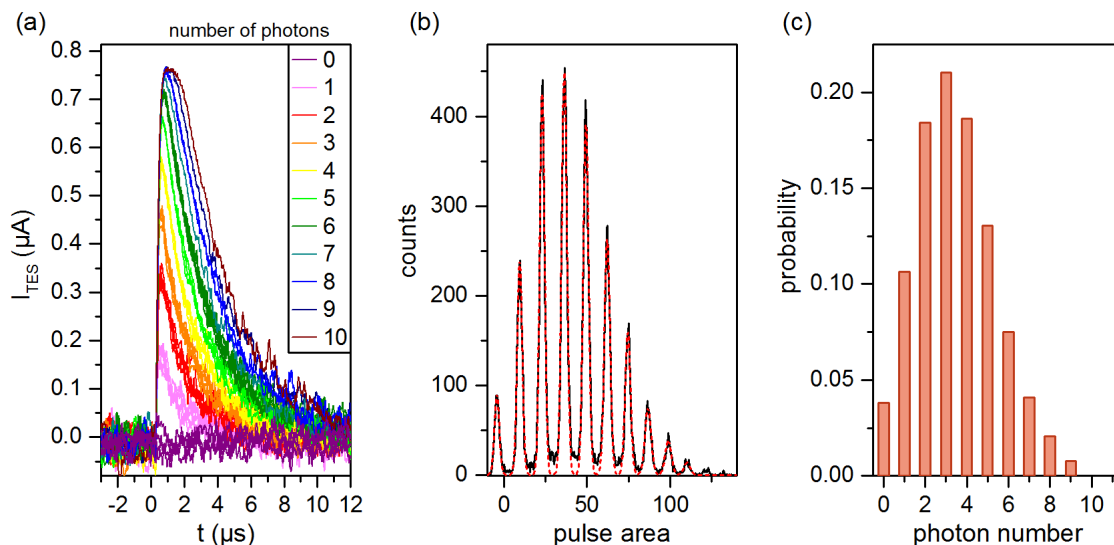


Figure 3.7: (a) Electrical output signal from the SQUID from 35 exemplary time traces of a laser at 650 nm. The distinction of the photon number is feasible by the eye and highlighted by the color coding. (b) Integration over the current signal yields the pulse area histogram. Gauss fits are depicted in the red dotted line. (c) The normalized area of the fitted peaks gives the PND.

analog-to-digital converter input [Dru07].

In the present system, the light is guided via a single-mode optical fiber to the tungsten TES in the present system [Mil11]. The sensitive area ($25 \cdot 25 \mu\text{m}^2$) of the TES is located in the center of a circular silicon disk displayed in figure 3.6 (a). A standard telecommunication fiber ferrule sleeve ensures the precise alignment of the $4.5 \mu\text{m}$ diameter fiber core to the sensitive TES area. Aluminum bonds are used for the inter-chip connections between the TES and the SQUID.

Exemplary analog output signals of the TES detection system under pulsed laser excitation at 650 nm are depicted in figure 3.7 (a). After the absorption of an optical pulse, the signal rises within a few hundreds of ns to the maximum, temporally limited by the SQUID electronics. The signal requires in the example about $\sim 10 \mu\text{s}$ to return to the initial state due to re-cooling of the sensor to base temperature.

The photon numbers can already be distinguished by the peak height of the SQUID signals. Here, the height and signal duration depend on the absorbed number of photons, highlighted in different colors. Three methods for data processing are discussed in [vH17] and [Sch18c]: Pulse height, pulse area, and principal components analysis. Integration over the SQUID pulse gives the pulse area, presented in figure 3.7 (b). Here, well-separated peaks correspond to different numbers of photons in the pulse. The deviation of the pulse

area from the mean value for any photon number n_{ph} is assumed to be random which is why the pulse area histogram is fitted with Gaussian peaks. The area of Gaussian fit functions is normalized to 1 and finally results in the PND, shown in figure 3.7 (c). Using this method, up to 27 photons could be reliably distinguished at a wavelength of 850 nm [vH17]. Noteworthy, the quantum efficiency is larger than 87 % at 850 – 950 nm for the utilized detector [Sch18c].

4 Fundamental Emission Characteristics of Quantum Dot Micropillar Lasers

Bimodal QD micropillar lasers show interesting emission characteristics and stochastic mode switching which is studied with spectroscopic methods in this chapter. The μEL emission spectra and the influence of the spontaneous emission factor β on the input-output dependence are discussed. In high- β microlasers information about the photon statistics is usually required to identify laser emission. Therefore, the second-order autocorrelation of QD micropillar lasers at the transition from spontaneous emission to lasing as well as the stochastic mode switching of bimodal QD micropillar lasers is presented.

4.1 Intensity Characteristics and Bimodal Behavior

Optical Modes of QD Micropillars

The optical modes of QD micropillars are classified as helical modes (HE- and EH-modes). Helical modes have contributions of the electrical and magnetic field in propagation direction. In HE-modes the electric dominates over the magnetic field and vice versa for EH-modes. The fundamental mode HE_{11} exhibits a similar intensity distribution to the fundamental transverse electromagnetic mode TEM_{00} (Gaussian beam) [Eic15]. Due to lateral mode confinement, the energy of higher-order modes is blue-shifted by a few meV if compared to the fundamental mode in micropillars with diameters of only a few μm [Gut98]. The gain spectrum of the QD emission band in the selected micropillars was measured to have an inhomogeneous broadening of about 30 meV [Hol18]. Depending on the spectral and spatial overlap of the QDs in the active layer and the micropillar modes, one or more modes can have sufficient gain to reach the lasing regime. For the following experimental results, QD micropillars with pronounced single-mode emission of the fundamental HE_{11} cavity mode were chosen.

The DBR mirrors of sample A are optimized for an emission wavelength of 850 nm and the width of the stopband is calculated to be around $\nu_{\text{SB}} = 160 \text{ meV} \cong 93 \text{ nm}$ (calculated via the refractive index of the two materials $\frac{\nu_{\text{SB}}}{E_{\text{cav}}} = \frac{4}{\pi} \arcsin \left| \frac{n_{\text{AlAs}} - n_{\text{GaAs}}}{n_{\text{AlAs}} + n_{\text{GaAs}}} \right|$ [Mac86]). The cavity

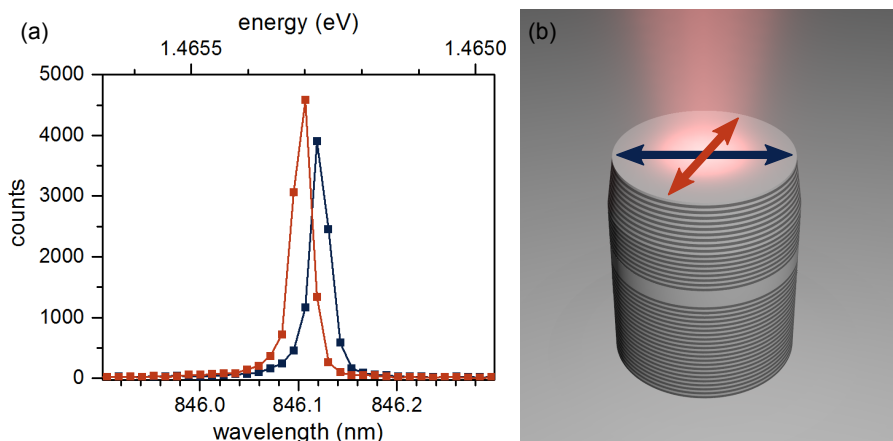


Figure 4.1: (a) Exemplary micro-electroluminescence spectrum of bimodal QD micropillar laser 4-1 with 4 μm diameter at $1.3 I/I_{\text{thr}}$ measured with the spectrometer. The fundamental mode of the laser is split into two linearly polarized mode components, which are energetically split by $30 \mu\text{eV}$. (b) Sketch of a QD micropillar with the two polarization components indicated by arrows.

is grown with a thickness of one λ_{cav} and therefore the formation of multiple longitudinal modes is impeded.

A typical micro-electroluminescence spectrum of a QD micropillar laser (QD micropillar 4-1) without visible higher-order lateral modes and a bright fundamental mode which is split into two orthogonally polarized mode components can be seen in 4.1. The micropillar shape is cylindrical, but the fabrication process can result in small deviations from a perfectly circular shaped crosssection. These asymmetries lift the degeneracy of the fundamental mode [Rei07]. The mode splitting amounts $30 \mu\text{eV}$ for QD micropillar 4-1 with 4 μm diameter (figure 4.1 (a)). The two resulting mode components have orthogonal linear polarization.

The quality factor Q of a planar DBR microcavity depends mainly on the refractive index contrast between the DBR layers n_{eff} , and the number of mirror pairs and is expected to be in the order of 50.000 in our case [Rei10]. The quality factor Q is reduced for micropillar cavities due to lateral losses generated e.g. by light scattering at imperfections on the side-walls [Böc08]. Q -factors exceeding 150,000 were reported [Rei07]. The quality factor Q can be experimentally estimated from the linewidth at transparency via the formula $Q = \frac{E_{\text{mode}}}{\nu_{\text{FWHM}}}$. For the two modes of the presented micropillar 4-1, the quality factors are around $Q = 18,000$.

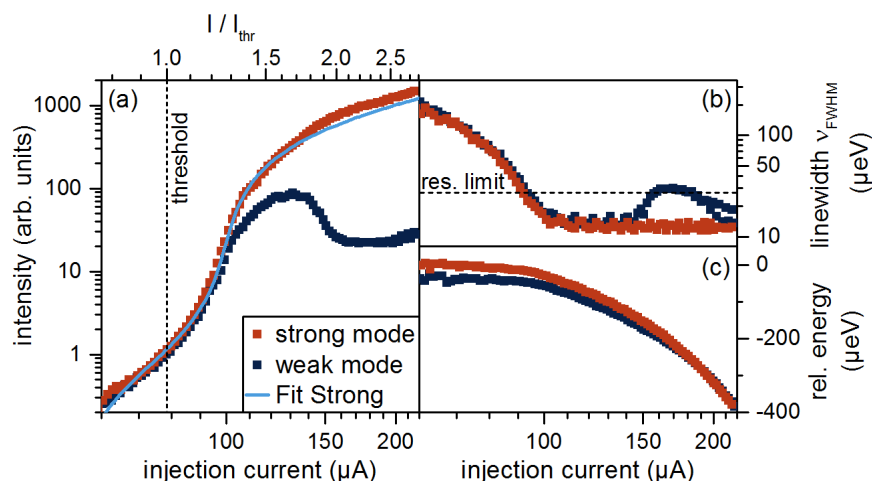


Figure 4.2: Input-output characteristics of bimodal QD micropillar laser 4-1 at 30 K. (a) The intensity of the strong mode (red dots) has an s-shaped behavior in double-logarithmic scaling. The weak mode (blue dots) increases at low injection currents with the pump, but decreases in intensity for $I > 1.7 I_{\text{thr}}$. The light blue line is a fit with $\beta = 0.0041 \pm 0.0003$. (b) Around threshold, both modes' linewidth strongly decreases below the resolution limit (dashed line). For high injection currents, the weak mode broadens significantly. (c) With increasing pump current, the emission shifts towards larger wavelengths due to heating of the sample.

Input-Output Characteristics

The pump dependent intensity, linewidth, and emission energy of QD micropillar 4-1 are shown in a double logarithmic plot in figure 4.2. For low injection current, spontaneous emission dominates and the output intensity of the QD micropillar scales linearly with the pump power in log-log scaling. At the threshold, stimulated emission sets in and the intensity increases superlinearly with the injection current. After the transition region, the intensity increase becomes linear again for high injection currents when the total pump power is converted to stimulated emission and gain-clamping occurs.

The enhanced spontaneous emission in high- β microlasers leads to a smooth s-shaped input-output dependence [Bjö94]. Interestingly, because of gain competition usually only one of the two modes enters the lasing regime [Ley13]. The red data points in figure 4.2, associated with emission of the mode polarized at 82° , from now on called strong mode, show the typical s-shaped microlaser behavior. The second mode polarized on 172° (blue dots), from now on called weak mode, does not reach the lasing regime. The input-output characteristics of the weak and the strong mode are similar up to a pump power of about $1.3 I/I_{\text{thr}}$. With increasing pump strength, the weak mode has lower emission intensity and further decreases at high injection currents. Both modes are amplified by the same charge

carriers and compete for the common gain provided by about 110 QDs in the active layer. Usually, one mode prevails and reduces the available gain for the second polarization component. The threshold is estimated as the matching point of linear regression from the part below threshold and the nonlinear part above threshold. For further analysis, the current is scaled to units of the threshold current I_{thr} .

The excitation power dependence of the linewidth is depicted in figure 4.2 (b). Stimulated emission increases the temporal coherence of the light and consequently leads to a reduction of the emission linewidth. Around laser threshold, the deconvoluted linewidth taking the resolution limit of the monochromator (black dashed horizontal line at $27 \mu\text{eV}$) into account reaches a minimum value of $13 \mu\text{A}$ (full width at half maximum, FWHM) at $1.3 I/I_{\text{thr}}$. The spectral line shape of the microlaser emission above the threshold is Lorentzian. A Voigt profile is fitted to the spectra which describes a convolution of the Lorentzian emission peak with the Gaussian response of the monochromator with a fixed linewidth of $27 \mu\text{eV}$. The weak mode's linewidth increases for $I/I_{\text{thr}} > 1.9$ and its intensity is decreasing in this region which indicates a reduced gain for the weak mode due to stimulated emission and efficient gain coupling of the strong mode.

The emission energy of both modes (figure 4.2 (c)) is constant for low injection currents and redshifts with increasing pump strength due to the heating of the QD micropillar [Jah12].

Estimation of the β Factor

In the presentation of the experimental input-output dependence of micropillar 4-1 a fit is inserted (c.f. figure 4.2 (a) blue line) which includes the β factor as a parameter. In order to describe the input-output characteristics of high- β microlasers, the following approach described in [Rei08a], based on the rate equation model introduced in [Bjö91], is applied to the experimental data. The excitation intensity I_{pump} is given by

$$I_{\text{pump}}(n_{\text{ph}}) = \frac{\hbar \omega_0}{\delta \tau_{\text{phot}}} \frac{1}{\beta} \left(\frac{n_{\text{ph}}}{1 + n_{\text{ph}}} \left(1 + N_0 V_M \frac{\tau_{\text{phot}}}{\tau_{\text{sp}}} \beta \right) \left(1 + \beta n_{\text{ph}} \right) - N_0 V_M \frac{\tau_{\text{phot}}}{\tau_{\text{sp}}} \beta^2 n_{\text{ph}} \right) \quad (4.1)$$

as a function of the photon number n_{ph} . The fitted parameters are the spontaneous emission factor β and the photon conversion efficiency δ which is a scaling factor of the injection current. The other parameters are estimated based on experimental results or after [Red16]. The emission energy $\omega_0 = 355 \text{ THz} \hat{=} 846 \text{ nm}$ and the lifetime of photons in the cavity $\tau_{\text{phot}} = \frac{Q}{2\pi \omega_0} = 8.1 \text{ ps}$ are estimated from the experimental spectra. The carrier concentration at transparency $N_0 = 7000 \mu\text{m}^{-3}$, the mode volume $V_M = 4 \mu\text{m}^3$ and the

spontaneous emission lifetime $\tau_{\text{sp}} = 1$ ns are estimated after [Red16, Sch16].

The measured emission intensity is scaled to the photon number $n_{\text{ph}} = 1$ at the threshold current I_{thr} for the experimental data in figure 4.2 (a). Fitting the experimental data yields $\beta = 0.0041 \pm 0.0003$ and $\delta = 2.93 \cdot 10^{-7} \pm 5 \cdot 10^{-9}$ for the plotted fit (figure 4.2). The determined value $\beta \approx 1\%$ is typical for the 4 and 5 μm micropillar lasers studied in this work. This result is in good agreement with values determined by more advanced modelling based on rate equations [Red16, Sch16, Sch19].

4.2 Temporal Emission Dynamics

Hanbury Brown and Twiss Measurements

Measurements of the second-order autocorrelation function $g^{(2)}(0)$ are crucial to prove coherent emission from microlaser devices. The applied Hanbury Brown and Twiss (HBT) method is introduced in section 3.3. Figure 4.3 (a) presents $g^{(2)}(\tau)$ of the weak mode of QD micropillar laser 4-2 at $1.3 I_{\text{thr}}$. Photon bunching with $g^{(2)}(0) = 1.5$ reveals a significant contribution of thermal light. The data is fitted with the function [Ulr07]

$$g^{(2)}(\tau) = \left(1 + \left(g^{(2)}(0) - 1\right) \cdot e^{-\left|\frac{\tau}{\tau_{\text{cor}}}\right|}\right) \otimes \frac{1}{\sqrt{2\pi\tau_{\text{res}}}} \cdot e^{-\frac{\tau^2}{2\tau_{\text{res}}^2}} \quad (4.2)$$

to take the time resolution $\tau_{\text{res}} = 56$ ps of the SPCMs into account. From the fit, the second-order autocorrelation at zero time delay $g^{(2)}(0)$ and the correlation time τ_{cor} can be extracted. The correlation time is related to the coherence time by $\tau_{\text{coh}} = 2 \cdot \tau_{\text{cor}}$ [Lou00].

The corresponding injection current dependence of $g^{(2)}(0)$ is shown in figure 4.3 (b). The emission of a QD micropillar laser is expected to have a thermal character with $g^{(2)}(0) = 2$ below the threshold. However, the coherence time below the threshold is usually much smaller than the temporal resolution so that the thermal character is often not accessible in HBT experiments [Ulr07]. If $\tau_{\text{coh}} < \tau_{\text{res}}$, the peak height of the measured $g^{(2)}(\tau)$ is lowered because of the convolution with the broader detector response. The buildup of coherence around threshold leads to increasing $g^{(2)}(0)$. For pump powers exceeding the laser threshold, emission of strong mode changes from thermal to coherent emission which leads to a decrease of $g^{(2)}(0)$. The strong mode is clearly in the lasing regime and emits coherent light with $g^{(2)}(0) = 1$ at $1.35 I_{\text{thr}}$ and higher pump strength.

$g^{(2)}(0)$ of the weak mode increases only weakly at threshold. However, $g^{(2)}(0)$ increases further up to a value of 1.85 at $I_{\text{thr}}=1.3$ above which $g^{(2)}(0)$ decreases to 1.15 at high injection currents of $I_{\text{thr}}=1.45$. This progression of the autocorrelation function is a hint for

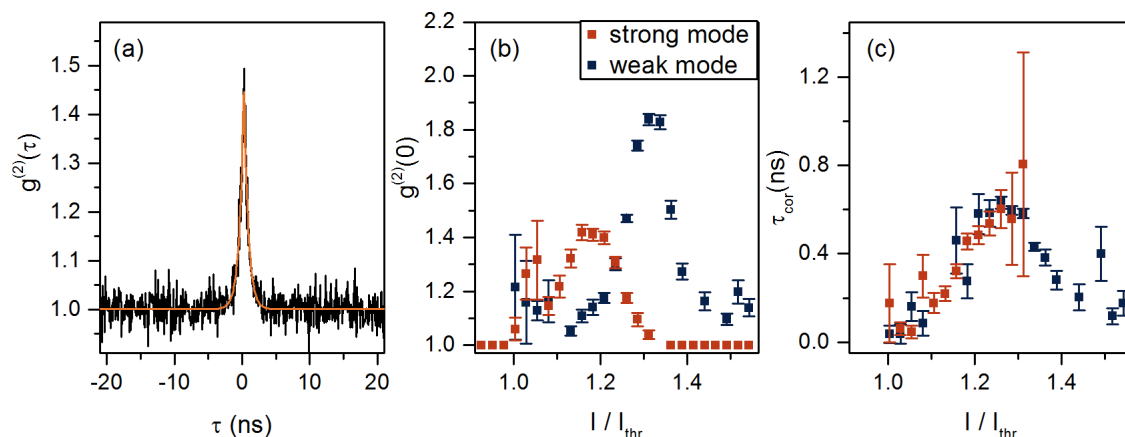


Figure 4.3: Measurement of the second-order autocorrelation function $g^{(2)}(\tau)$ of $\varnothing = 4 \mu\text{m}$ QD micropillar laser 4-2: (a) An exemplary measurement of the weak mode's $g^{(2)}(\tau)$ at $1.3I_{\text{thr}}$ reveals photon bunching with a peak height of 1.5. (b) $g^{(2)}(0)$ as a function of the injection current is 1 below threshold and starts to increase around the threshold for both modes. $g^{(2)}(0)$ of the strong mode decreases for $I/I_{\text{thr}} > 1.2$ to 1 for coherent emission. $g^{(2)}(0)$ of the weak mode reaches higher values up to 1.85 at $1.3 I_{\text{thr}}$, which can be a hint for dynamical mode switching. (c) The width of the autocorrelation function τ_{cor} is related to the coherence time of emission.

stochastic switching of laser emission between the strong and weak mode [Ley13, Mar18]. In bimodal lasers, where the modes compete for the same gain, intensity fluctuations can result in a switch of lasing from one to the other mode. The related statistical fluctuations lead to stochastic switching.

The weak mode is mostly emitting on a low intensity level, but a switch can bring the weak mode to lasing for a short time. If so, the weak mode's emission intensity is clearly temporally correlated via emission of laser pulses and $g^{(2)}(0)$ increases. In this case, the correlation time τ_{cor} (c.f. figure 4.1 (c)) is attributed to the residence time, also called dwell time τ_{dwell} , of pulsed lasing action of the weak mode. Equal correlation times τ_{cor} for the weak and the strong mode affirm the assumption of mode switching in the bimodal micropillar. The dwell time and the occurrence of switching processes are strongly dependent on the pump power [Vir13]. For high pumping with $I/I_{\text{thr}} > 1.4$, no further evidence of switching events is given which indicates the strong mode shows stable laser emission. The weak mode's emission is in a mixed state of thermal and coherent emission, shown by constant $g^{(2)}(0) \approx 1.15$ and $\tau_{\text{cor}} \approx 0.2$ ns.

Bimodal lasers can also be realized with other laser systems than VCSELs and QD micropillar lasers. Ring lasers can possess co- and counterpropagating modes which influence each other and can result in stochastic mode switching [MT78, Sin79]. In photonic crystal

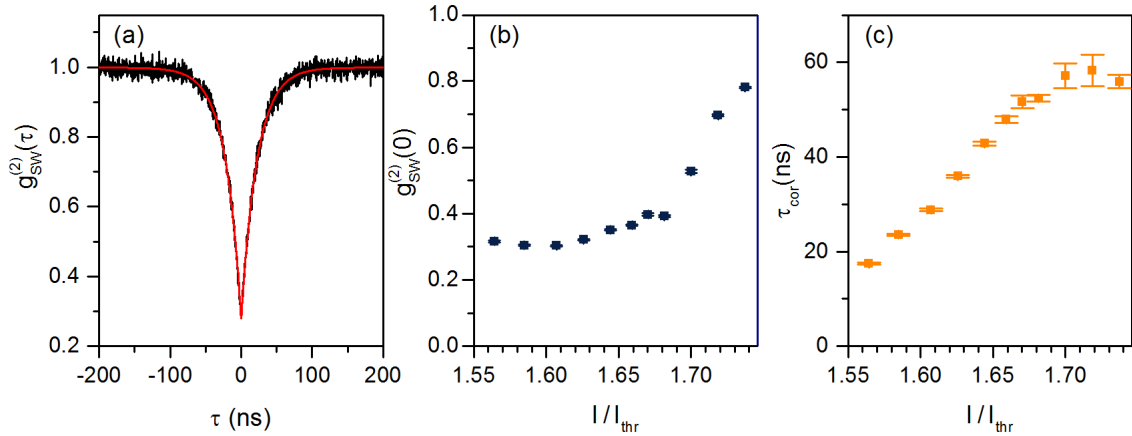


Figure 4.4: (a) Exemplary cross-correlation measurement $g_{SW}^{(2)}(\tau)$ between the two modes of $\varnothing = 4 \mu\text{m}$ QD micropillar laser 4-1 at $1.6 I_{thr}$ exhibiting a strong antibunching which indicates mode switching between the weak and the strong mode. (b) $g_{SW}^{(2)}(0)$ in dependence of the injection current increases in the region where the intensity drop of the weak mode is dominant (cf. 4.2). (d) The correlation time τ_{cor} is associated with the dwell time τ_{dwell} .

lasers two cavities can be coupled to reveal mode switching [Mar16, Mar18].

Cross-Correlation Measurements

The second-order autocorrelation function of a QD micropillar laser can provide an indication of stochastic mode switching. Cross-correlation measurements are performed to verify this behavior. Therefore, the emission of the weak and the strong mode is detected independently by two SPCMs and temporally correlated (c.f. section 3.3).

The measured cross-correlation function $g_{SW}^{(2)}(\tau)$ between weak and strong mode of QD micropillar laser 4-1 shows antibunching in the case of temporal correlation as exemplarily shown in figure 4.4 (a). The anticorrelation proves that either one mode can reach the lasing regime at a time and emit with high intensity. Then lasing operation 'switches' stochastically from one mode to the other. If the cross-correlation function at zero time delay $g_{SW}^{(2)}(0)$ is larger than 0, the mode in the non-lasing state is not fully dark and emits light with reduced intensity compared to the lasing state. The width of the function is related to the dwell time τ_{dwell} . The cross-correlation $g_{SW}^{(2)}(\tau)$ can be fitted by the same equation as the autocorrelation (4.2).

The cross-correlation function at zero time delay $g_{SW}^{(2)}(0)$ is depicted in 4.4 (b). Switching effects are most pronounced in the minimum of 1.3 between 1.55 and 1.65 I/I_{thr} . $g_{SW}^{(2)}(0)$ increases with the pump strength. The correlation time τ_{cor} in panel (c) increases with the

injection current up to 60 ns. The spontaneous emission decreases with increasing pump strength and mode switches are less probable and longer [Red16]. The QD micropillar laser 4-1 under study is different from microlaser 4-2 for which the autocorrelation measurement in figure 4.3 was obtained, where the maximum switching occurs at lower pump powers. The switching dynamics vary for the individual laser because the dynamics are very sensitive to the device parameters and the excitation strength [Vir13].

Streak Camera Measurements

QD micropillar laser 4-1 presented in this chapter shows switching on large time scales (~ 100 ns) and thus enables a direct measurement with a Streak camera (c.f. section 3.3). The presented experimental results were performed jointly with Sören Kreinberg and Steffen Holzinger and are published in [Red16].

The streak camera is used in single shot mode which allows the measurement of single μ EL transients shown in figure 4.5. The x-axis is the time in a 2μ s window on which the strong and the weak mode emission appear as horizontal lines. Randomly distributed detection events are due to dark counts. The pump current of $1.7 I_{\text{thr}}$ was chosen because the cross-correlation measurement (c.f. figure 4.4) revealed a quantitatively long correlation time $\tau_{\text{cor}} \approx 60$ ns and a low correlation $g_{\text{WS}}^{(2)}(0) \approx 0.4$ and thus a hint for frequent switching.

In the time trace presented in figure 4.5, the weak mode intensity dominates in the first 70 ns before switching occurs and the strong mode shows laser emission. Two further switches from the strong to the weak mode appear at 170 ns and 1230 ns. Obviously, only one mode is lasing at a time which is mainly related to gain competition of the two modes. In the lower panel, the integrated intensity of emission from the weak (blue) and the strong mode (red) can be seen. Comparing the average intensity of the weak and the strong mode in the lasing and non-lasing state, respectively, the strong mode is brighter. However, the dominating strong mode is in a metastable state and intensity fluctuations can lead to an intensity transfer to the weak mode.

In summary, this chapter presented fundamental measurements of bimodal QD micropillar lasers. The spectra of a bimodal QD micropillar show two polarization contributions of the fundamental cavity mode. The input-output characteristics of the two contributions reveal that one, the strong mode, has an s-shaped characteristic of high- β microlasers while the other component, the weak mode, has a lower emission intensity. HBT measurements prove the transition to lasing of the strong mode. Pronounced antibunching in cross-correlation measurements between the weak and the strong mode of a QD micropillar

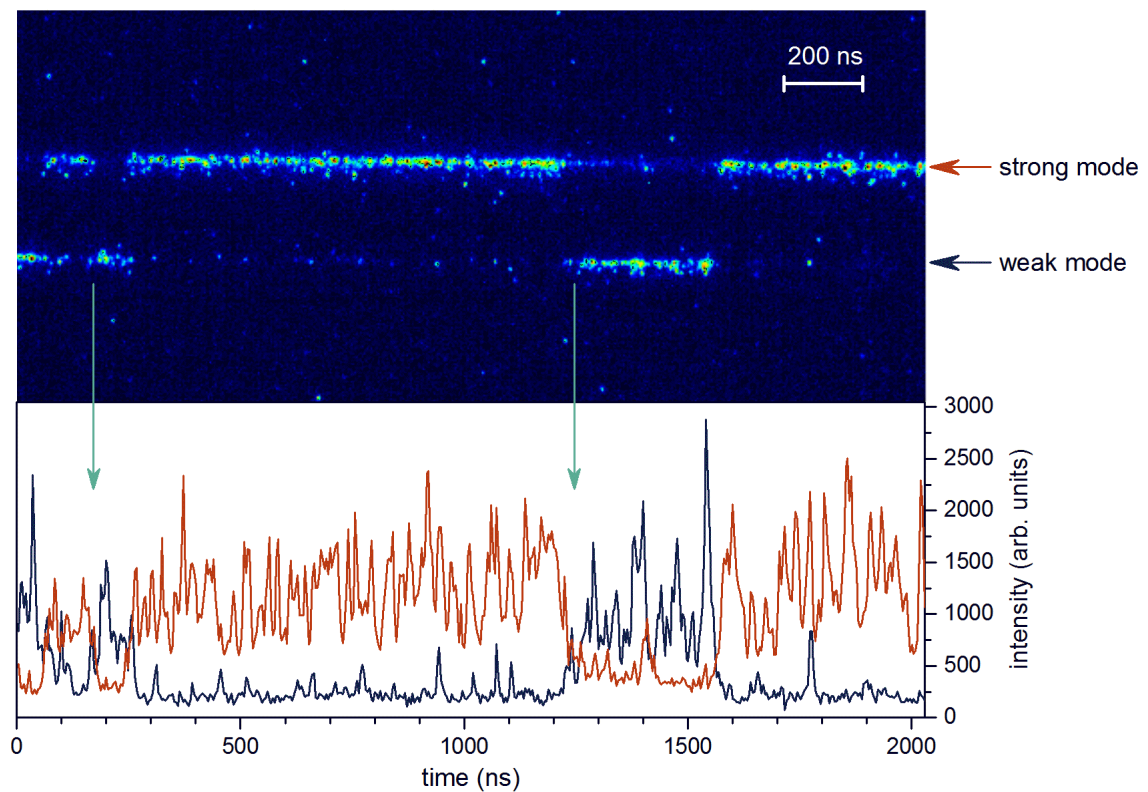


Figure 4.5: Single shot time trace taken with a Streak camera showing the intensity of weak and strong mode of QD micropillar laser 4-1 at $1.7 I_{\text{thr}}$. Within this $2 \mu\text{s}$ time frame the lasing switches twice from the strong to the weak mode and back. The lower panel depicts the integrated intensity of both modes.

laser indicate stochastic mode switching due to gain competition which is directly shown in time traces measured by a streak camera.

5 Photon Number Distribution of Microlasers

In the previous chapter, the measurement of the second-order autocorrelation function $g^{(2)}(\tau)$ for the verification of lasing of QD micropillar lasers was presented. This chapter goes beyond and demonstrates the full photon statistics of QD micropillar lasers and exciton-polariton lasers. A transition-edge sensor based photon number resolving detection system enables the measurement of the photon number distribution to obtain in-depth insight into the emission dynamics

In section 5.1, the temporal and spectral response of electrically driven QD micropillars is investigated. Their photon number distribution is determined via a transition-edge sensor and discussed in section 5.2. Two bimodal microlasers with non-switching (micropillar 4-2) and switching (micropillar 4-3) characteristics, both from sample A (c.f. section 3.1 and A.1), are contrasted with each other. The results presented in this section are published in [Sch18b].

Exciton-polariton lasers are based on stimulation scattering of polariton quasi-particles to the ground state. In section 5.3, the photon number distribution of exciton-polariton lasers in transition to coherent emission, published in [Kla18b], is discussed.

5.1 Pulsed Electrical Excitation

Characteristics of the Electrical and Optical Pulses

The emission behavior of the $\varnothing = 4 \mu\text{m}$ QD micropillar laser 4-2 at 30 K under pulsed electrical excitation is discussed in the following. Its emission wavelength is at 849.9 nm. The electrical pulse shape of the pulse generator measured with an oscilloscope is depicted in figure 5.1 (a) for the maximum specified output voltage (5.1 V) of the source. The turn-on and turn-off time of the output voltage is approximately 1 ns. For pulses $\tau_{\text{pulse}} > 5 \text{ ns}$, the turn-on time plays a minor role and the pulses are nearly rectangular.

Figure 5.1 (b) shows exemplarily the emission pulse shape of QD micropillar laser 4-2 for electrical excitation with $\tau_{\text{pulse}} = 10 \text{ ns}$ and a nominal pulse height of 5.0 V. For all subsequent measurements, an additional DC offset of 1.5 V was chosen to bias the device close to the onset of EL emission. As such, the microlaser emission at 1.5 DC voltage is

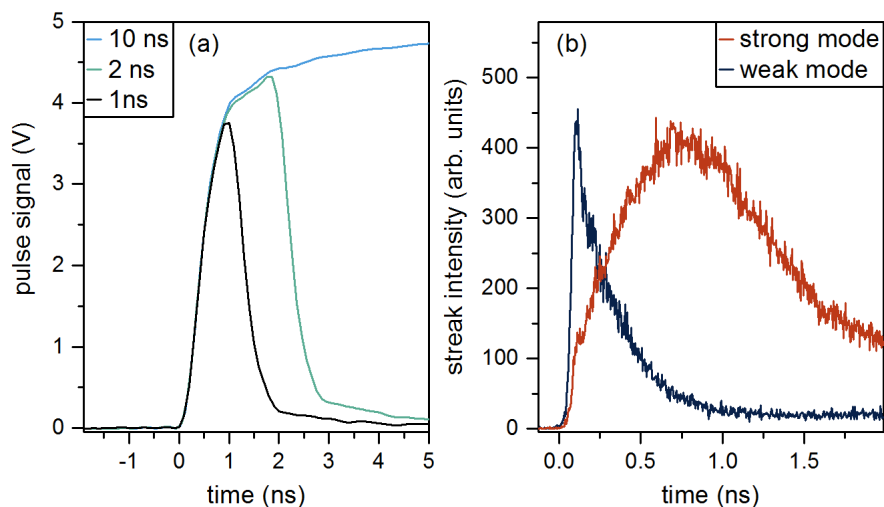


Figure 5.1: (a) Electrical output of the pulse generator (HP 8131A) for a pulse height of 5.1 V and a pulse length of $\tau_{\text{pulse}} = 1, 2$ and 10 ns measured with an oscilloscope. (b) Optical pulse shape of both polarization modes from QD micropillar laser 4-2 with 4 μm diameter measured with a streak camera (integration mode). The sample is electrically excited with a pulse height of 5 V and a pulse duration of 10 ns. After the turn-on of the electrical pulse at 0 ns, emission of both modes is detected. The intensity of the weak mode increases quickly with a rise time of 18 ps while the rise of the strong mode is delayed and shows a rise time of 320 ns. After 0.25 ns the strong mode takes over.

negligible, but enables a larger excitation range with the maximum pulse height of 5.1 V. The measurement is taken with a streak camera in integration mode (q.v. section 3.3). Both polarization modes of the laser increase within tens of ps in intensity after the turn-on of the electrical pulse. Interestingly, the weak mode turn-on reaches the maximum intensity after 110 ps while the strong mode attains the maximum after 400 ps. The weak mode intensity decreases after 110 ps and stabilizes at a low intensity. In contrast, the strong mode intensity decreases further and is almost constant after 1.5 ns. This intensity dynamics can be interpreted as follows [Ley17]: The weak mode has higher gain coupling and can, therefore, increase much faster in intensity. However, the intermode kinetics can favor the strong mode. Thus, the weak mode 'loses' intensity to the strong mode and amplifies it. The slower, but enduring, intensity increase of the strong mode supports this interpretation. It is worth mentioning that this temporal intensity characteristic was seen by several bimodal QD micropillars of this particular sample, but it is not a general characteristic for QD micropillars as it depends sensitively on the mode and gain coupling factors.

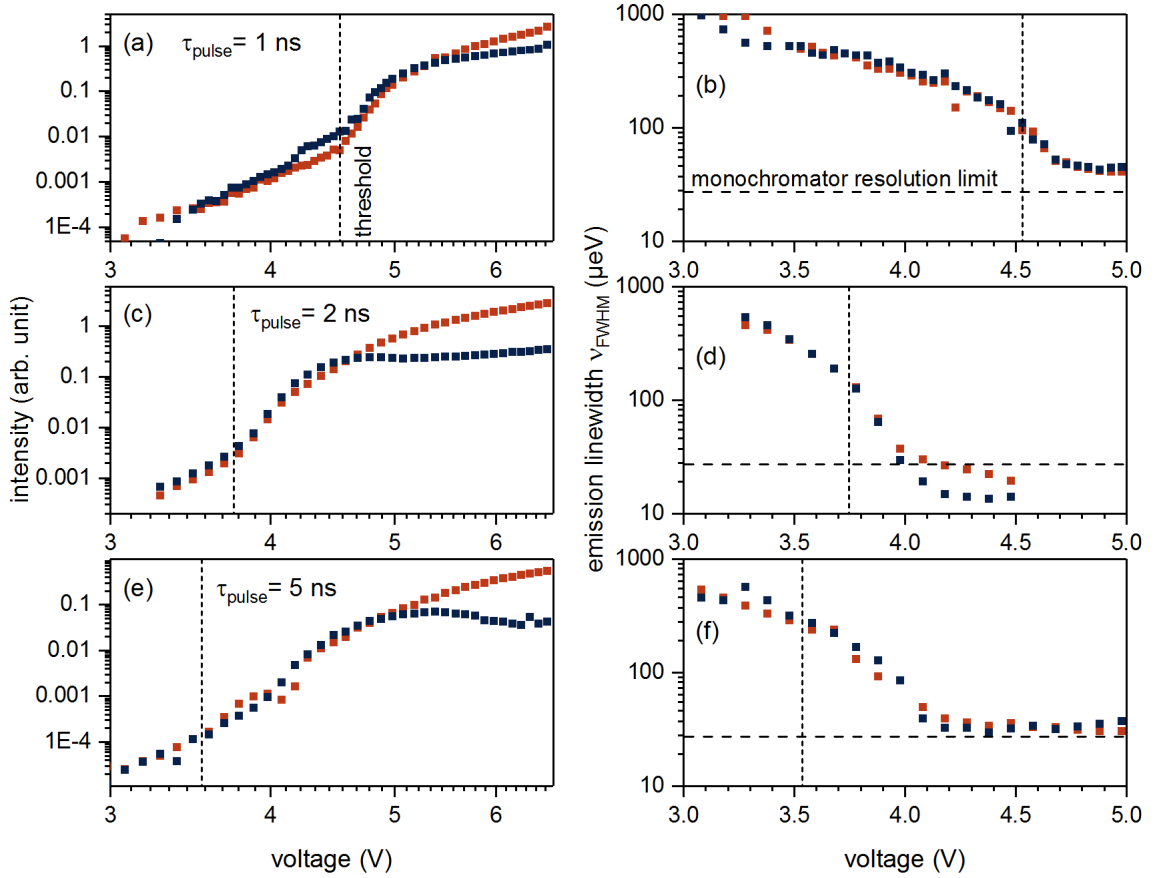


Figure 5.2: Input-output characteristics (left) and emission linewidth (right) of QD micropillar laser 4-2 under pulsed excitation with pulse lengths of $\tau_{\text{pulse}} = 1, 2$ and 5 ns. The distinct s-shape reveals a decreasing threshold V_{thr} with increasing τ_{pulse} while the intensity difference between the weak and the strong mode is enlarged. The linewidth reduction sets in at lower voltage for longer pulses.

Optical Response of a QD Micropillar Laser under Pulsed Excitation

In the following, QD micropillar laser 4-2 from the same sample as micropillar laser 4-1 is studied under pulsed electrical excitation. The corresponding input-output characteristics with $\tau_{\text{pulse}} = 1, 2$ and 5 ns (figure 5.2 left side) show pronounced s-shaped behavior with lasing action for the strong mode. The lasing threshold is $V_{\text{thr}} = 3.5$ V for pulses with $\tau_{\text{pulse}} = 5$ ns and increases for reduced pulse lengths to $V_{\text{thr}} = 3.75$ V for $\tau_{\text{pulse}} = 2$ ns and $V_{\text{thr}} = 4.5$ V for $\tau_{\text{pulse}} = 1$ ns. The threshold is estimated conventionally as the matching point of linear regression from the part below and above threshold. The shape and the height of the electrical pulse were shown to be dependent on the pulse length in figure 5.1 which also affects the input-output characteristics in a non-trivial way.

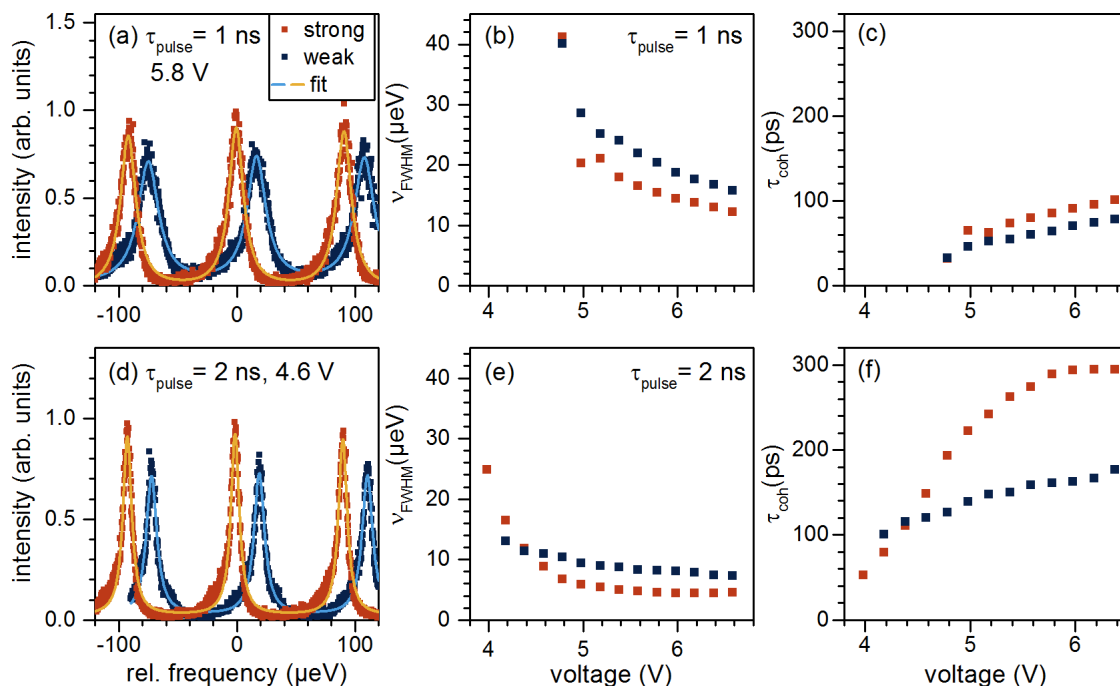


Figure 5.3: Emission spectra of the weak and the strong mode from QD micropillar 4-2 measured with a FPI for pulsed excitation with (a) $\tau_{\text{pulse}} = 1$ ns and (d) $\tau_{\text{pulse}} = 2$ ns for varied pump voltage. From the corresponding fit (line) the linewidth, (b) and (e), is extracted. The linewidth decrease sets in at lower voltage for $\tau_{\text{pulse}} = 2$ ns and reaches overall lower values. (c) and (f): The coherence time τ_{coh} increases with the applied pulse height up to $\tau_{\text{coh}} = 100$ ps for $\tau_{\text{pulse}} = 1$ ns and $\tau_{\text{coh}} = 300$ ps for $\tau_{\text{pulse}} = 2$ ns.

For the chosen pulse lengths τ_{pulse} , the weak mode has a slightly higher intensity than the strong mode up to a voltage of 4.5 or 5 V. This is in good agreement with the description of the optical pulse shape for figure 5.1 and the assumed better gain coupling of the weak mode. Around 5 V the strong mode takes over. For short pulses with $\tau_{\text{pulse}} = 1$ ns, the intensity difference between weak and strong mode has a factor of 2. For longer pulses with $\tau_{\text{pulse}} = 2$ and 5 ns, the intensity difference increases up to a factor of 7 and 14, respectively. The intensity dependence on the pulse length can be explained by the optical pulse shape (c.f. figure 5.1 (b)) where the weak mode has a larger intensity than the strong mode in the first 0.5 ns after the turn-on before it stabilizes at low intensity.

The linewidth is shown in figure 5.2 on the right-hand side. For short pulses of $\tau_{\text{pulse}} = 1$ ns in panel (b) the linewidth decreases slowly while for panels (d) and (f) it reaches the resolution limit at around 4 V. The set in of the linewidth reduction is in good agreement of the estimated threshold.

As will be discussed in the following in more detail the measured photon statistics depends

on the coherence time compared to the excitation pulse length. The coherence time can be estimated via the linewidth assuming negligible influence of inhomogeneous broadening on the linewidth. For this reason, high-resolution spectra were recorded with an FPI and analyzed. The utilized FPI enables the reliable determination of the linewidth down to $100 \text{ MHz} \cong 0.4 \text{ } \mu\text{eV}$ corresponding to a coherence time of about 10 ns.

Figure 5.3 (a) and (d) show exemplary spectra of QD micropillar 4-2 measured with the FPI. Three FSRs are plotted with the corresponding Lorentzian fits. The linewidth extracted from the fit (panel (b) and (e)) is in agreement with the linewidth measured with a spectrometer in figure 5.2. The linewidth of the strong mode decreases to $12 \text{ } \mu\text{eV}$ for pulses with $\tau_{\text{pulse}} = 1 \text{ ns}$ and to $5 \text{ } \mu\text{eV}$ for $\tau_{\text{pulse}} = 1 \text{ ns}$. The linewidth of the weak mode is in both cases $3 \text{ } \mu\text{eV}$ larger.

The coherence time can be estimated for Lorentzian shaped peaks by the formula [Lou83]

$$\tau_{\text{coh}} = \frac{1}{\pi \nu_{\text{FWHM}}} \quad (5.1)$$

and depends solely on the emission linewidth ν_{FWHM} . For the here discussed QD micropillar 4-2, the coherence time increases with the applied voltage, as shown in figures 5.3 (c) and (f). For $\tau_{\text{pulse}} = 2 \text{ ns}$, the determined coherence time τ_{coh} at high voltage is 300 ps for the strong mode and 170 ps for the weak mode, respectively. For $\tau_{\text{pulse}} = 1 \text{ ns}$ pulses, τ_{coh} does not exceed 100 ps. The micropillar modes redshift with increasing pump power due to heating (c.f. figure 4.2 (c)) which also causes a spectral shift within the pulse duration under pulsed excitation and possibly leads to an overestimation of the emission linewidth. Although the weak mode is not lasing, the linewidth of both modes are locked due to incoherent coupling which leads to a mixing of the cavity-mode frequencies. Consequently, the weak mode has a coherence time in the same order than the strong mode [Kha15].

5.2 Measurement of the Photon Number Distribution

The photon statistics of QD micropillar lasers can contribute to a deep understanding of their emission processes. Pulsed excitation of a QD micropillar laser enables the measurement of the photon number with a TES and the determination of the PND. Details on this special experimental method are discussed in 3.3. The PND of $\varnothing = 4 \text{ } \mu\text{m}$ QD micropillar laser 4-2 is exemplarily shown in figure 5.4 at three characteristic points of the input-output curve (c.f. 5.2 (c)) with a pulse length of $\tau_{\text{pulse}} = 2 \text{ ns}$. The three characteristics points are 4.0 V, slightly above threshold, 4.4 V is at the second kink of the input-output curve and at 6.4 V the strong mode is clearly in the lasing regime.

At the lowest pump voltage in (a) and (b) the PND of the weak and the strong mode ap-

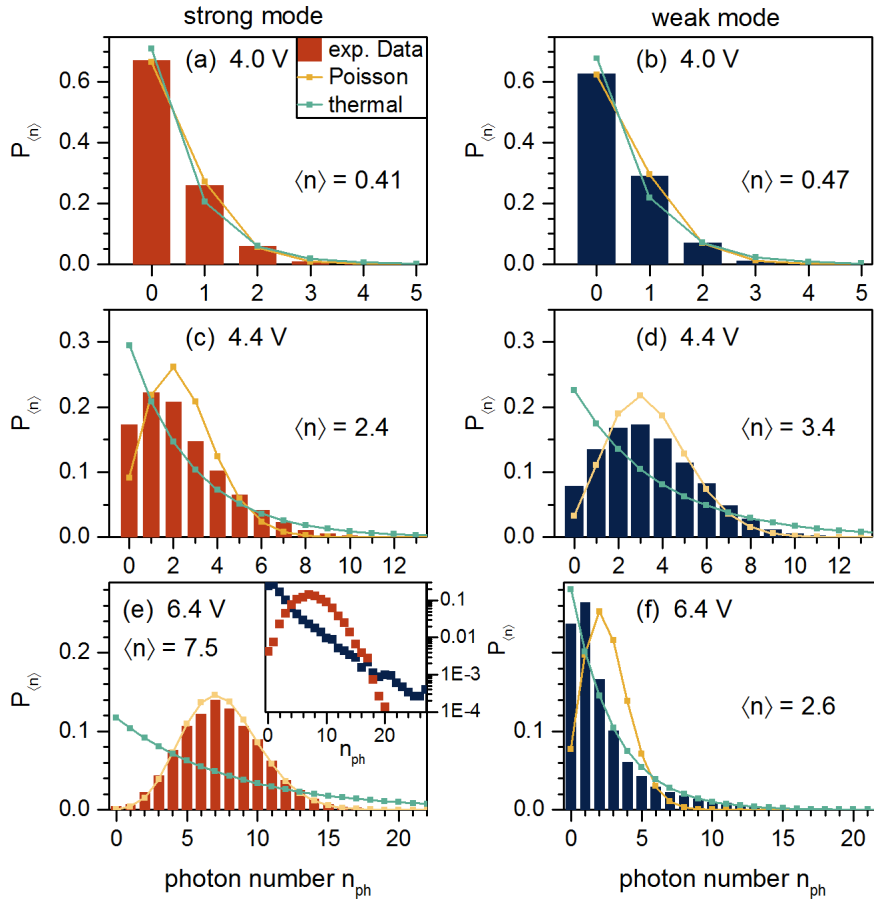


Figure 5.4: Photon number distribution $P_{\langle n \rangle}$ of QD micropillar laser 4-2 for three different pump voltages of the strong mode (left) and weak mode (right). The bars represent the experimental data. For each graph, a Poissonian distribution and a thermal distribution with the same mean photon number $\langle n \rangle$ are plotted. (a) and (b): For low voltage, the measured distribution is Poissonian due to the coherence time limitation. (c) and (d): For intermediate voltages, both modes show a mixed state of thermal and coherent emission. (e) and (f): Under strong pumping, the strong mode has a Poissonian and the weak mode a thermal statistic. The inset shows the data of both modes in logarithmic scaling.

pear to the eye like a thermal distribution with the highest probability for the zero-photon state. For a comparison of the experimental data, a Poissonian (yellow dots and line) and thermal (green dots and line) distribution with the same mean photon number $\langle n \rangle$ are plotted in the same graph. For the low mean photon number (a) $\langle n \rangle = 0.41$ and (b) $\langle n \rangle = 0.47$, the Poissonian and thermal distribution are not very different, especially for photon numbers n_{ph} of 2 or higher. The Poissonian distribution is in good agreement with the experimental data. Around the laser threshold, the microlaser emission is expected to show thermal statistics, but as discussed for figure 4.3 the short coherence time τ_{coh}

inhibits the measurement of this characteristic. This aspect will be further addressed later in figure 5.7.

The PNDs of the strong and weak mode are similar for intermediate pump powers of 4.4 V presented in figure 5.4 (c) and (d). The main difference is the mean photon number of $\langle n \rangle = 2.4$ and $\langle n \rangle = 3.4$ in panels (c) and (d), respectively. The PND of the microlaser exceeds the Poissonian distribution for photon numbers $n_{\text{ph}} < 2$ and $n_{\text{ph}} > 6$. Both modes are in a mixed state of thermal and coherent emission [Are66].

Far above the threshold at 6.4 V, the PNDs of the strong mode (e) and the weak mode (f) differ distinctly. The strong mode is in a pure coherent laser state. A neutral density filter (NDF) with an optical density of 0.5 was introduced to shift the highest identified photon number to 23 into the detection range of about 27 photons of the TES. The character of a distribution is not changed by an NDF, only the mean photon number $\langle n \rangle$ is reduced. The mean photon numbers in panels (e) and (f) are $\langle n \rangle = 7.5$ and $\langle n \rangle = 2.6$, respectively. The weak mode is close to a thermal emitter with a very long 'tail' for high photon numbers n_{ph} up to approximately 27, while the brighter coherent emission has only non-neglectable probability up to $n_{\text{ph}} = 20$ which can be seen in the inset of figure 5.4 (e). However, the weak mode in panel (f) has slight deviations from thermal statistics due to coherence time limitations. The coherence time $\tau_{\text{coh}} \approx 300$ ps (c.f. 5.3 (d)) is shorter than the pulse length $\tau_{\text{pulse}} = 2$ ns and the distribution gets a more Poissonian-like character.

Photon Statistics Evolution of a Non-Switching Bimodal QD Micropillar Laser

The evolution of the PND of QD micropillar laser 4-2 from low to high excitation strength is depicted in figure 5.5. Below 4.1 V, the mean photon number is $\langle n \rangle < 1$ and differentiation of thermal and coherent emission is not feasible by the eye. Up to 4.6 V, the PNDs of the weak and the strong mode are similar which is in agreement with the associated input-out-characteristics presented in figure 5.2 (c). Both modes are in a mixed state of thermal and coherent emission. Furthermore, the coherence time limitation shifts the PND towards a Poissonian distribution (c.f. figure 5.7). After 5 V, the PND of both modes varies and evolves to a lasing for the strong mode and a non-lasing state for the weak mode, respectively. The strong mode has a pure coherent character and only $\langle n \rangle$ changes with the pumping strength. The weak mode transforms from a mixed state towards a predominantly thermal state.

The excitation power dependence of the second-order autocorrelation $g^{(2)}(0)$ is well known for QD micropillar lasers and easy to calculate with knowledge of the PND. The results of the PND are compared with measurements of the HBT and discussed quantitatively. As described in the theory section 2.4 in formula 2.31 the autocorrelation can be calculated

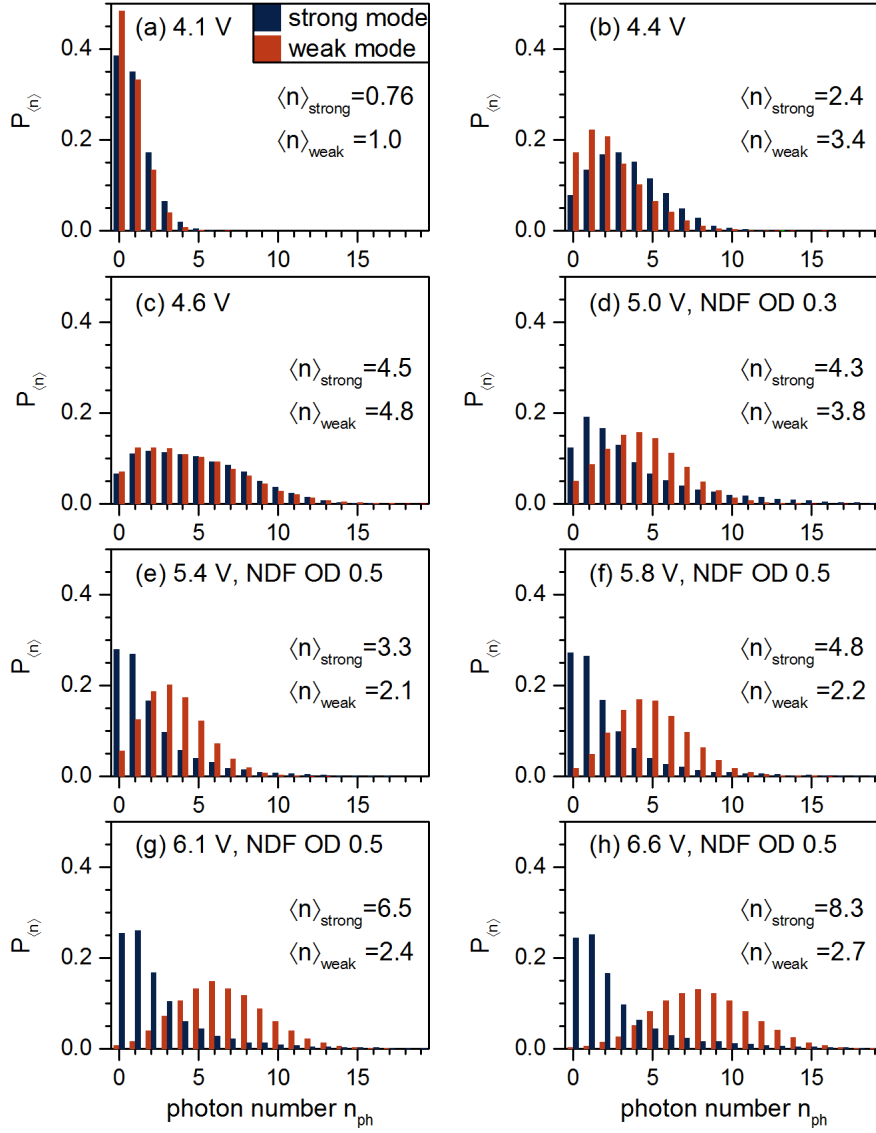


Figure 5.5: PND of both modes of QD micropillar laser 4-2 for pulses with a voltage between 4.1 and 6.6 V and $\tau_{\text{pulse}} = 2$ ns. (a)-(c) For low bias voltage, both modes show a similar PND and are in a mixed state of coherent and thermal emission. (d)-(h) With increasing pump voltage the strong mode (dark red) increases in intensity and has a Poissonian distribution while the PND of the weak mode has a lower mean photon number $\langle n \rangle$ and a predominantly thermal character. NDF OD indicates the optical density of a neutral density filter used to attenuate the optical signal under high pump strength.

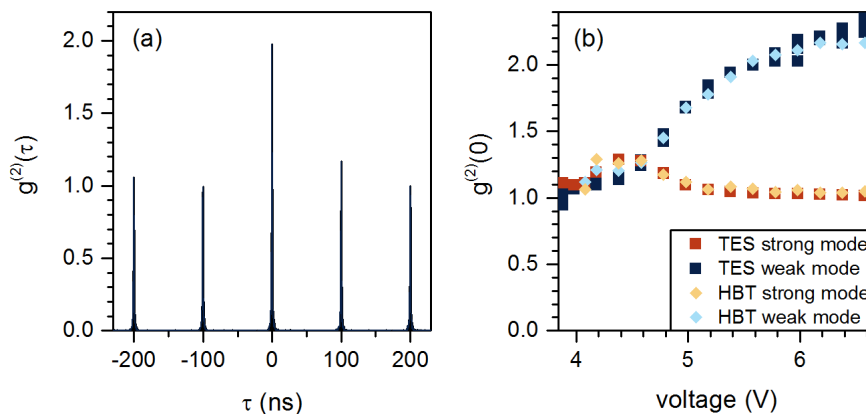


Figure 5.6: (a) Exemplary HBT measurement of $g^{(2)}(\tau)$ under pulsed excitation ($\tau_{\text{pulse}} = 2$ ns) from the weak mode of micropillar 4-2 at 5 V. The peak area of the central peak is normalized by the adjacent peaks to determine $g^{(2)}(0)$. (b) Comparison of $g^{(2)}(0)$ measured with an HBT (bright blue and yellow rhombs) and calculated from the PND (blue and red squares).

in any order from the PND. To recapitulate, the second-order autocorrelation is given by

$$g^{(2)}(0) = 1 + \frac{\text{Var}(n_{\text{ph}}) - \langle n \rangle}{\langle n \rangle^2} \quad (5.2)$$

and only depends on the mean photon number $\langle n \rangle$ and variance $\text{Var}(n_{\text{ph}})$ of the PND. $g^{(2)}(0)$ is additionally determined by a standard HBT measurement to prove the accuracy of the PND by the comparison with a well-established method. An exemplary measurement of $g^{(2)}(\tau)$ measured with the HBT of the weak mode at 5 V is shown in figure 5.6 (a). The repetition frequency is set to 10 MHz (100 ns pulse distance) to have multiple pulses within the time window of the time-to-digital converter. The pulse distance is long enough to suspend memory effects of the microlaser. The central peak area is normalized by the average area of the other peaks to calculate the $g^{(2)}(0)$.

The results of $g^{(2)}(0)$ estimated with the HBT and the TES are compared with each other in figure 5.6 (b). The bigger squares in the background are associated with the data obtained from the PND and the smaller rhombs with the data from the HBT. The data points of both methods are in very good agreement and prove that a TES-based photon number resolved measurements is an excellent method to determine the photon statistics of nanophotonic devices like QD micropillar lasers.

Around 4.0 V, $g^{(2)}(0)$ is 1, indicating coherent emission. For low pump strength, the QD micropillar emission is expected to have a thermal character. However, for $\tau_{\text{coh}} \ll \tau_{\text{pulse}}$

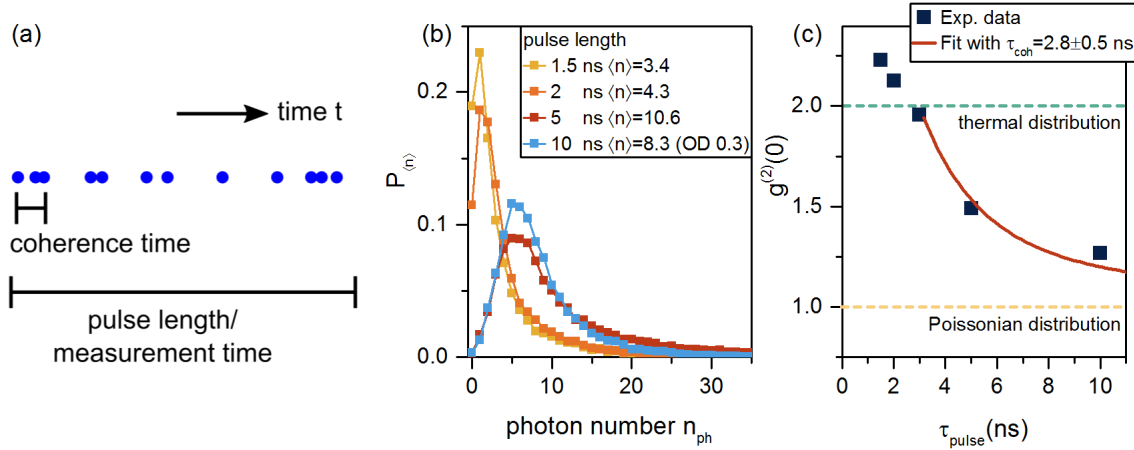


Figure 5.7: (a) Sketch to illustrate the correlation of coherence time τ_{coh} and pulse length τ_{pulse} . Photon bunching of thermal emission arises within the coherence time. Longer τ_{pulse} averages over several bunching events and the emission artificially appears coherent. (b) PND of thermal emission of QD micropillar laser 4-2 with varied pulse length τ_{pulse} for a pump voltage of 6 V. With increasing pulse length, the mean photon number $\langle n \rangle$ increases, while the probability $P_{\langle n \rangle}$ for larger photon numbers n_{ph} decreases, proving the inaccessibility of the thermal character. (c) The corresponding second-order autocorrelation $g^{(2)}(0)$ decreases with τ_{pulse} .

the emission appears coherent. This mechanism is equivalent to a limited temporal resolution of the SPCMs with CW excitation (c.f. figure 4.3) when $\tau_{\text{coh}} \ll \tau_{\text{res}}$.

The autocorrelation at zero time delay $g^{(2)}(0)$ begins to rise at approximately 4.2 V. The coherence buildup in the microlaser (c.f. figure 5.3 (d)) enables to measure the mixed state of thermal and coherent emission for both modes, as discussed for figure 5.4. The strong mode is in a stable lasing state with $g^{(2)}(0) \approx 1$ after 5.2 V, whereas $g^{(2)}(0)$ of the weak mode further increases up to a value around 2, indicating thermal emission. The fact that $g^{(2)}(0)$ has values slightly above 2 at high pump strength can be a hint for stochastic switching or intensity fluctuations [Red16]. The PND in figure 5.5 (h) is close to a thermal distribution for the weak mode which supports the interpretation that intensity fluctuations cause $g^{(2)}(0) > 2$.

The sketch in figure 5.7 (a) aims to clarify the influence of the coherence time τ_{coh} on the results of TES-based measurements of the photon statistics. Blue dots symbolize photons emitted by a thermal light source. Thermal light produces bunched photons, which means that after the emission of one photon the emission probability for another photon is increased on the time scale of the coherence time τ_{coh} . If $\tau_{\text{pulse}} > \tau_{\text{coh}}$, the measurement process averages over several bunching events. As a result, the photon bunching cannot be resolved and the emission appears uncorrelated leading to an (artificially) Poissonian-like

PND.

The PND and $g^{(2)}(0)$ of thermal emission from the weak mode of QD micropillar laser 4-2 is presented for different τ_{pulse} in figure 5.7 (b) and (c). The PND for short pulses of $\tau_{\text{pulse}} = 1.5$ ns is close to that of a thermal distribution. Values of $g^{(2)}(0)$ slightly exceed 2 which, in this case, can be attributed to fluctuations mainly caused by turn-on and -off effects through the electrical pulses. Indeed, the optical pulse shape in figure 5.1 (b) reveals a non-constant intensity over the pulse length. The corresponding intensity changes can lead to $g^{(2)}(0)$ exceeding the thermal value of 2.

With increasing τ_{pulse} , the mean photon number $\langle n \rangle$ rises which impedes a clear discrimination of the thermal characteristics. The probability of observing high photon numbers $n_{\text{ph}} > 20$ decreases from $\tau_{\text{pulse}} = 5$ to 10 ns. This is clear evidence for a seemingly vanishing thermal character. The decreasing $g^{(2)}(0)$ as a function of the pulse length, presented in figure 5.7 (c), confirms the less pronounced thermal character with increasing pulse length τ_{pulse} . The dependence of $g^{(2)}(0)$ on the pulse length for thermal light can be described by [Lou00]

$$g_{\text{therm}}^{(2)}(0) = -\frac{\tau_{\text{coh}}}{2 \tau_{\text{pulse}}} \left(e^{-2 \frac{\tau_{\text{pulse}}}{\tau_{\text{coh}}}} - 1 \right) + 1 . \quad (5.3)$$

The equation is used to model the experimental data from the excitation power where $g^{(2)}(0) < 2$. The coherence time is estimated to be $\tau_{\text{coh}} \approx 2.5 \pm 0.5$ ns. This value is larger than the lower limit of the coherence time $\tau_{\text{coh}} \approx 170$ ps of the weak mode for $\tau_{\text{pulse}} = 2$ ns (c.f. figure 5.3 (d)) as determined from the emission linewidth. This apparent discrepancy is explained by the fact that the linewidth of the emission spectra is potentially overestimated because equation 5.1 does not consider additional inhomogeneous broadening caused by transient spectral shifts due to the pulsed excitation scheme applied in the experiment.

Higher-Order Photon Autocorrelation Functions

Equally to the second-order autocorrelation function $g^{(2)}(0)$, higher orders of the autocorrelation can be calculated from the PND according to formula 2.31. The autocorrelation of k -th order depends on the distribution's moments up to the k -th order. The 'skewness' of a distribution is determined by the third-order moment, respectively the 'kurtosis' by the fourth-order moment. Higher-order autocorrelations are for instance interesting for a better understanding of the laser threshold [Ley14].

Experimental access to higher-order ($k > 2$) photon correlations is in general not easily accessible for nanophotonic devices, because of their low emission intensity. An HBT

configuration with an additional beamsplitter and a third SPCM provides one possibility to measure the third-order autocorrelation $g^{(3)}(0)$ which was demonstrated in reference [Hor10] for an exciton-polariton condensate. M. Aßmann et al. developed another method to measure multiple photon events which provide access to the higher-order photon correlations using a streak camera equipped with a dual time-base module in single-shot mode. Applying this technique, they were able to determine the autocorrelation of an exciton-polariton condensate up to the fourth order [Aßm09, Wie09]. Alternatively, the autocorrelation of higher orders is directly accessible with a TES, by measuring the PND for nanophotonic devices.

Figure 5.8 depicts the second-, third- and fourth-order autocorrelation $g^{(k)}(0)$ as a function of the voltage for QD micropillar laser 4-2. From the experimental data, the autocorrelation up to the order of the highest measured photon number $k = n_{\text{ph}}$ can be calculated. The data is presented only up to the fourth order since the higher orders describe the similar trend. As discussed for figure 5.6, $g^{(2)}(0)$ of the strong mode increases above the threshold between 4 and 5 V. The autocorrelation value $g^{(2)}(0)$ does not exceed 1.3 while the other orders have the maximum at $g^{(3)}(0) = 2.0$ and $g^{(4)}(0) = 3.2$. This indicates that the strong mode is in a mixed state of thermal and coherent emission between 4 and 5 V. Thermal emission takes values of $k!$ for the k 's order ($g_{\text{therm}}^{(2)}(0) = 2$, $g_{\text{therm}}^{(3)}(0) = 6$, $g_{\text{therm}}^{(4)}(0) = 24$, ...) which increases $g^{(k)}(0)$ of a mixed state with k .

The non-lasing weak mode in figure 5.8 (b) converges to a thermal state with $g^{(2)}(0) \approx 2.2$. The value of the third-order autocorrelation function $g^{(3)}(0)$ increases up to 10 and $g^{(4)}(0)$ to 50 which is significantly super-thermal above the thermal limit of $k!$, 6 and 24, respectively. This behavior can be interpreted in the sense that the PND does not reveal a pure thermal state with a coherence time τ_{coh} limitation. Additional intensity fluctuations in the turn-on and -off processes (c.f. figure 5.3) can cause deviations from the thermal limit which are more pronounced for higher orders. This nicely demonstrates the benefit of studying also higher-order correlations which are more sensitive on deviations from pure thermal or coherent light states than the easily accessible $g^{(2)}$ function.

To compare the different orders of the autocorrelation with each other, the values for coherent and thermal emission are projected on each other. For this purpose, a scaling is applied which was first introduced by Aßmann et. al [Aßm09]

$$g_{\text{scale}}^{(k)}(0) = \frac{\left(g^{(k)}(0) - 1\right)}{k! - 1}. \quad (5.4)$$

Using this scaling, the value of $g^{(k)}(0)$ for thermal emission is projected to 1 and for coherent emission to zero for all orders k . As a result, the strong mode shows decreased

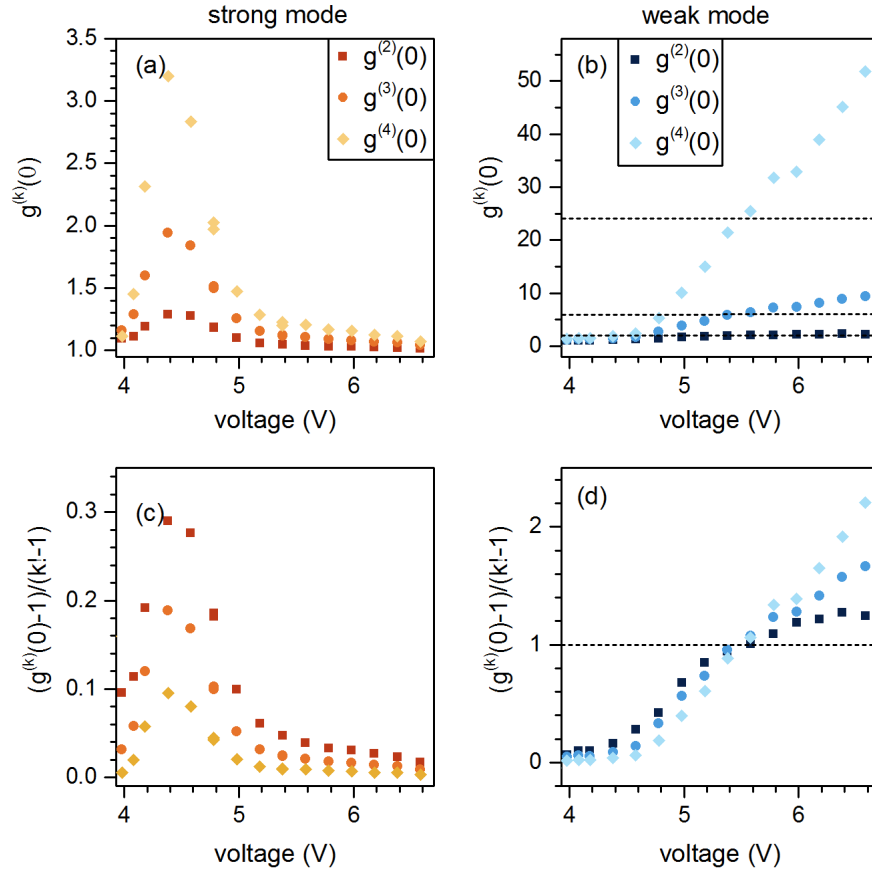


Figure 5.8: Higher-order autocorrelation $g^{(k)}(0)$ for (a) the strong mode and (b) the weak mode of QD micropillar laser 4-2 as a function of the applied bias voltage. $g^{(k)}(0)$ of the strong mode rises between 4 and 5 V for all orders, more pronounced with increasing order. $g^{(k)}(0)$ of the weak mode increases with the pump strength. Dashed lines display the value $k!$ for thermal emission. (c) and (d) show the data normalized after eq. 5.4. With the scaling, the autocorrelation of the high orders of the weak mode increase for high voltage.

bunching in 5.8 (c). The third and fourth-order autocorrelation are close to zero for a high pump strength confirming the coherent character of emission. The opposite is found for the weak mode. Fluctuations in the low intensity of the weak mode lead to an asymmetric PND which is uncovered by $g_{\text{scale}}^{(k)}(0)$ of higher order than 2. Below 5.5 V, the second-order $g_{\text{scale}}^{(2)}(0)$ is larger than the fourth-order autocorrelation $g_{\text{scale}}^{(4)}(0)$. For higher voltages, this behavior is inverted and $g_{\text{scale}}^{(4)}(0)$ increases up to 2.2, indicating the asymmetry of the PND. In general, the increasing values for the higher-order autocorrelations can be attributed to intensity fluctuations.

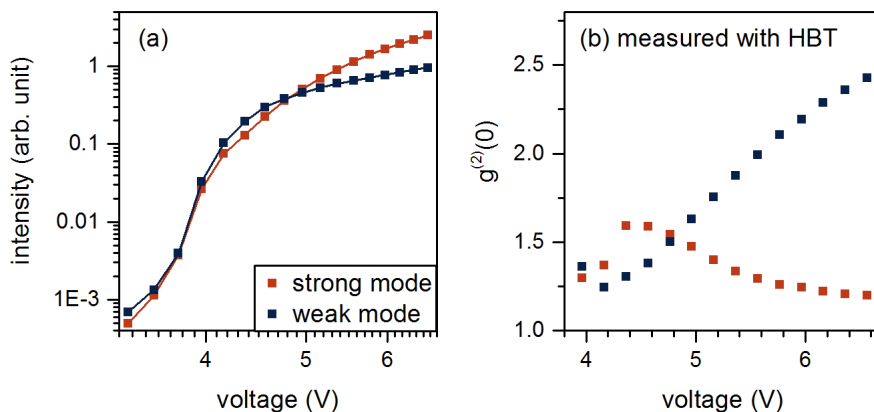


Figure 5.9: (a) Input-output characteristics of QD micropillar laser 4-3 under pulsed excitation with $\tau_{\text{pulse}} = 1.5$ ns. The behavior is very similar to that of microlaser 4-2 presented in figure 5.2. For injection current above the laser the threshold, the weak mode has a slightly higher intensity. The strong mode's input-output curve is s-shaped. (b) Corresponding $g^{(2)}(0)$ values in dependence of the applied voltage. For injection current above the threshold, the $g^{(2)}(0)$ of the strong mode decreases while the weak mode increases to values close to thermal emission.

Photon Statistics of a Switching QD Micropillar Laser

The importance of measuring the full photon number distribution are highlighted by experiments performed on QD micropillar laser 4-3 which has similar input-output and $g^{(2)}(0)$ characteristics than QD micropillar laser 4-2 (c.f. figure 5.2), but a very different PND. The emission intensity is plotted in figure 5.9 (a) in dependence of the bias voltage. The input-output characteristics of the strong mode is s-shaped as expected for a microlaser. The weak mode has a slightly higher intensity up to 4.7 V, above which saturation sets in. Autocorrelation values $g^{(2)}(0)$ of both modes, determined by an HBT, increase around 4 V. At high excitation currents, $g^{(2)}(0)$ of the strong mode approaches 1 indicating coherent emission of light. In contrast, $g^{(2)}(0)$ values of the weak mode increase with injection current which is either caused by thermal emission of the weak mode or a bistable behavior. The PND for QD micropillar laser 4-3 is presented in figure 5.10 for a bias voltage of 5.5 V. The PND of both, the weak and the strong mode, has two maxima at $n_{\text{ph}} = 0$ and $n_{\text{ph}} = 8 - 9$. Interestingly, the two contributions are both a thermal distribution with a low mean photon number $\langle n \rangle$ and a Poissonian distribution with a maximum at a photon number $n_{\text{ph}} = 8$ or 9 photons. This linear combination is caused by a bistable turn-on process of the QD micropillar laser: The majority of the electrical pulses drive the strong mode into the lasing regime, while the weak mode emits thermal light. However, due to

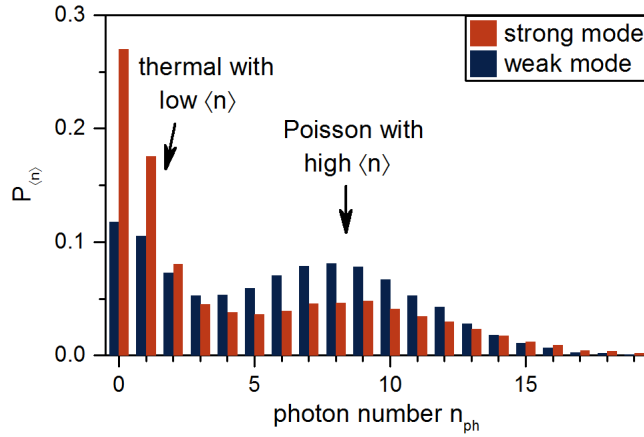


Figure 5.10: PND at a bias voltage of 5.5 V with $\tau_{\text{pulse}} = 1.5$ ns of QD micropillar laser 4-3. Both, the weak and the strong mode show a PND corresponding to a thermal distribution with a low $\langle n \rangle$ and a Poissonian distribution with a large $\langle n \rangle$.

the rather weak bistability it can also occur that the weak mode wins the gain competition upon electrical trigger and reaches the lasing regime whereas the strong mode emits thermal light with low intensity.

The equivalent process under CW excitation is stochastic temporal mode switching as presented and discussed for figure 4.5 in the previous chapter. The observation of two contributions to the PND is possible if two conditions are met: a) both modes have to be able to reach the lasing regime and b) the dwell time τ_{dwell} of the weak mode needs to be larger than the pulse duration τ_{pulse} . For $\tau_{\text{dwell}} < \tau_{\text{pulse}}$, a mode switch can appear within one excitation pulse. In this case, the resulting PND was a mixed state of thermal and coherent emission and no linear combination of both distributions would be measured.

The development of the PND for increasing bias voltage is shown in figure 5.11. In (a) and (b) the distribution is comparable to a mixed state between thermal and coherent emission (c.f. 5.5 (a) and (b)). For $V > 4.8$ V (c), the two contributions in the PND can be separated. A Poissonian distribution occurs with a monotonously increasing $\langle n \rangle$ and a thermal distribution.

Further insight into the emission statistics of QD micropillar laser 4-3 can be obtained by a fit of the PND with a linear combination of a thermal and a coherent distribution according to

$$P(n_{\text{ph}}) = x \cdot \frac{(\langle n \rangle_{\text{coh}})^{n_{\text{ph}}}}{n_{\text{ph}}!} e^{-\langle n \rangle_{\text{coh}}} + (1 - x) \cdot \frac{(\langle n \rangle_{\text{ther}})^{n_{\text{ph}}}}{(\langle n \rangle_{\text{ther}} + 1)^{n_{\text{ph}} + 1}}. \quad (5.5)$$

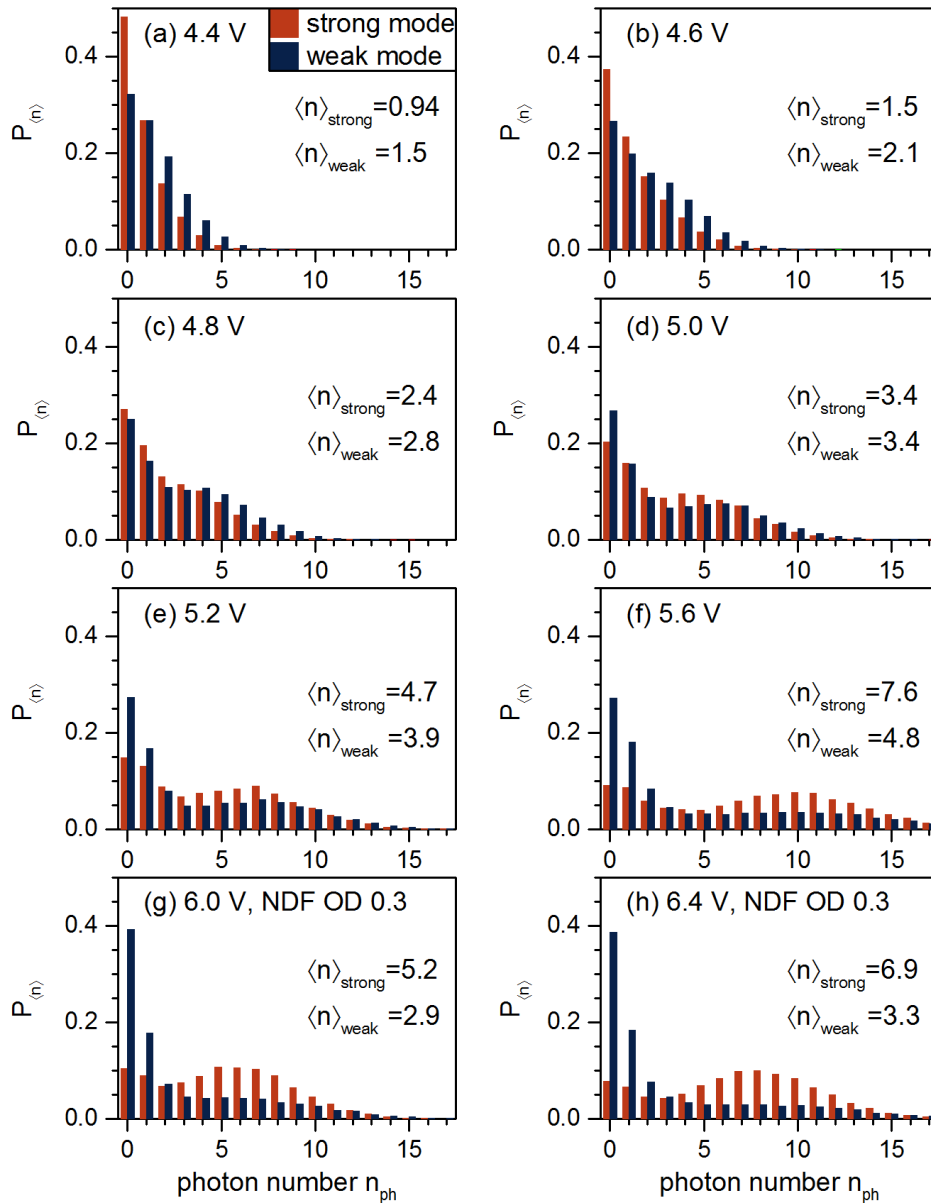


Figure 5.11: PND evolution for the bistable QD micropillar laser 4-3 between 4.4 and 6.4 V for $\tau_{\text{pulse}} = 1.5$ ns. For bias voltages larger than 4.8 V, bistable emission contributions of a thermal and Poissonian distribution can be identified in the PND. The maximum of the coherent part shifts to larger $\langle n \rangle$ with increasing bias voltage.

The fit includes the mean photon numbers $\langle n \rangle_{\text{coh}}$ and $\langle n \rangle_{\text{ther}}$, of the thermal and coherent part, respectively, and the weighting x , giving the percentage of the Poissonian part. An exemplary fit in figure 5.12 (a) illustrates the very good agreement between the experimental data and the model.

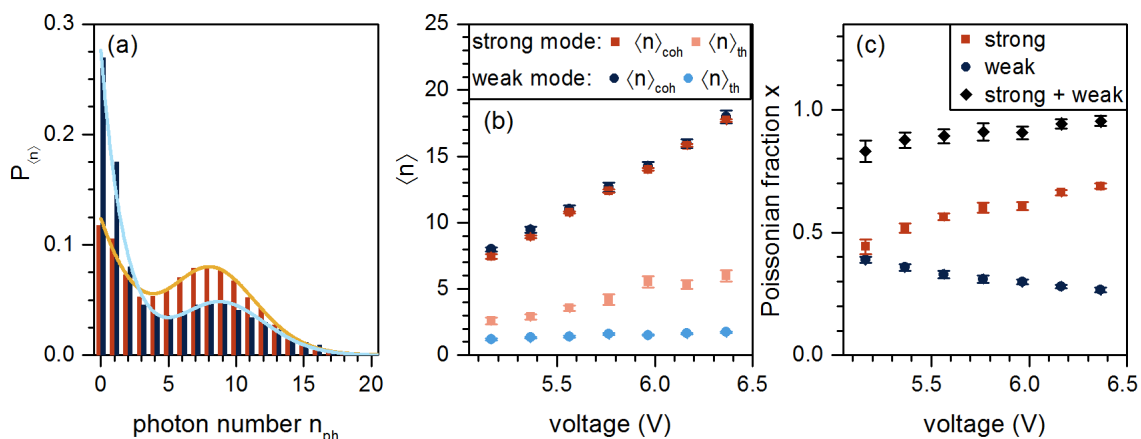


Figure 5.12: (a) Exemplary fit of both microlaser modes with a linear combination of a thermal and a coherent distribution at 5.4 V showing good agreement with the experimental data. The fit parameters are (b) the mean photon numbers $\langle n \rangle_{\text{coh}}$ and $\langle n \rangle_{\text{ther}}$ of both contributions and (c) the Poissonian fraction x . With increasing voltage, the strong mode reaches more often the lasing regime.

The mean photon number of the Poissonian part $\langle n \rangle_{\text{coh}}$ for the bias voltage dependent measurement of the PND is very similar for the weak mode (dark blue) and the strong mode (dark red), shown in figure 5.12 (b), and increases from $\langle n \rangle_{\text{coh}} = 8$ to 18 with increases bias voltage. Interestingly, the mean photon number of the thermal distribution $\langle n \rangle_{\text{ther}}$ in figure 5.12 (b) is different for the weak and the strong mode. $\langle n \rangle_{\text{ther}}$ of the weak mode has an almost constant value of 1.5, independent of the voltage. Meanwhile, the strong mode's $\langle n \rangle_{\text{ther}}$ is monotonically increasing. A possible reason for this peculiar behavior can be a non-neglectable pump dependent probability of a mode switch from the weak to the strong mode within the pulse duration τ_{pulse} . CW experiments of VCSELs have shown a high dependency of the dwell time from the pump power [Vir13]. In the case of mode switching during an excitation pulse, $\langle n \rangle_{\text{coh,weak}}$ is expected to decrease with the increase of $\langle n \rangle_{\text{ther,strong}}$.

The Poissonian fraction x in figure 5.12 (c) indicates the probability of each mode to reach the lasing regime. The likeliness of the strong mode to enter a lasing state is monotonously increasing with the pump strength from 0.45 to 0.7. Although it is expected that one mode at a time is in the lasing regime, the sum of the Poissonian fraction of both modes is lower than 1 and the coherent part appears underestimated. This underestimation can be a hint for mode switching within a pulse. A mode switch leads to an intermediate photon number for both modes and accordingly to a misclassification of the Poissonian part.

Equal to the first case of a stable microlaser, presented in figure 5.8, the higher orders

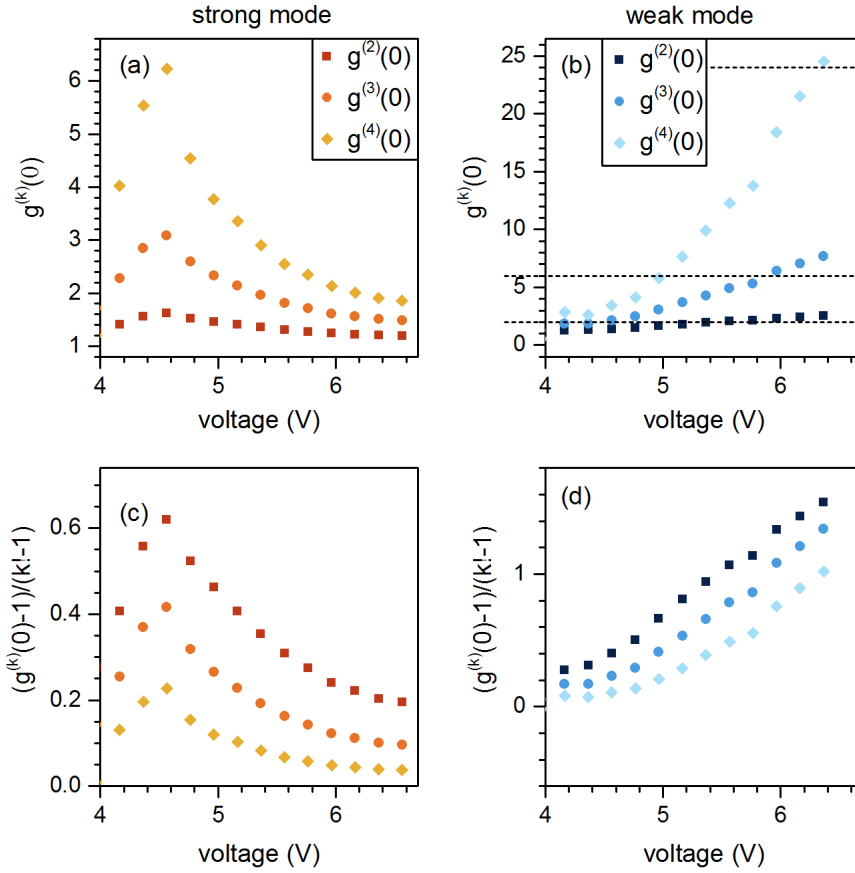


Figure 5.13: Second-, third- and fourth-order autocorrelation for zero time delay of the bistable QD micropillar laser 4-3 as a function of the bias voltage with $\tau_{\text{pulse}} = 1.5$ ns. $g^{(k)}(0)$ values of the strong mode (a) and the weak mode (b) show larger values for higher orders. With a comparative scaling in (c) and (d), the higher orders exhibit a reduced magnitude.

of the autocorrelation are presented for the bistable microlaser 4-3 in figure 5.13. The strong mode's behavior of $g^{(k)}(0)$ (a) is very similar for the stable and bistable microlaser. However, the $g^{(k)}(0)$ of the bistable QD micropillar laser 4-3 with values up to 3 (6) for the third (fourth) order are higher and the transition to lasing is smoother. With the scaling of formula 5.4, shown in figure 5.13 (c), the second order is always larger than the fourth order, as for the stable case.

The trend of $g^{(k)}(0)$ for the weak mode, depicted in figure 5.13 (b) appears also similar for both microlasers, however, the overshoot of the thermal limit (indicated by dashed lines) is much lower for the bistable microlaser 4-3 with $g^{(3)}(0) = 9.3$ and $g^{(4)}(0) = 24.5$. In contrast to the previous case, the scaled $g_{\text{scale}}^{(k)}(0)$ reveals lower values with increasing order.

Comparing of the photon statistics of the switching and the non-switching QD micropillar laser, 4-3 and 4-2, respectively, shows clearly that the $g^{(2)}(0)$ is not sufficient to describe photon statistics of the device. Many effects like mode competition [Ley13, Red16], superradiance [Jah16], gain saturation [Jag18] or dissipative coupling [Fan16] can generate deviations in the photon statistics which are not revealed by simple HBT-based $g^{(2)}(0)$. This clearly highlights the importance of determining higher-order photon correlations by photon number resolving TES detector systems.

It is worth emphasizing that the photon statistics of bimodal ring-lasers has been analyzed by photomultiplier tubes [MT78]. These detectors are able to estimate the probability of a mode intensity $P(I)$ in photon counting mode, but as they do not provide photon number resolution, thus, the PND is not accessible. Consequently, with photomultiplier tubes the photon statistics of quantum emitters and microlasers cannot be measured.

5.3 Photon Statistics of Exciton-Polariton Lasers

Exciton-polariton lasers are a specific kind of microlasers whose characteristics feature intriguing physics and promise record low threshold pump powers due to the buildup of coherence by Bose-Einstein condensation without the need of population inversion. In fact, exciton-polariton quasi-particles condensate by stimulated scattering into the energetic ground state and enable coherent emission. The condensation process is not completely understood, and studies of the photon statistics can contribute to deeper comprehension. The photon number distribution of an exciton-polariton laser is presented in this section. The exciton-polariton laser device is presented in the methods chapter in section 3.1 and A.3. In the first part, the fundamental emission characteristics of an exciton-polariton laser are introduced. Afterwards, the excitation power dependent PND and the model of mixed states of thermal and coherent emission of an exciton-polariton laser are discussed. The results of this section originate from a joint work with Martin Klaas from the University of Würzburg. The results of this section are published in [Kla18b].

Coherent Emission from Exciton-Polariton Devices

Strong coupling of quantum well (QW) excitons to an electromagnetic field leads to the formation of exciton-polariton quasi-particles. Exciton-polaritons were observed for the first time in 1992 [Wei92]. Polaritons possess a bosonic character and consequently, an arbitrary number of these quasi-particles can be in the same energetic state. The transition of many bosons to the ground state of a system is called Bose-Einstein condensation and has also been observed for exciton-polaritons [Den02, Kas06]. Such devices resemble photon lasers because exciton-polaritons decay under the radiation of coherent emission. In our case, the light-matter coupling is realized in microcavities build by DBR-structures which are processed to micropillars (see section 3.1). The chosen micropillar structure 6-1 has a diameter of 6 μm . The exciton-polariton sample is optically excited by a pulsed Ti:sapphire laser at 1.66 eV=748 nm with a repetition frequency of 80 MHz.

The energy dispersion relation presented in figure 5.14 exhibits the emission properties of an exciton-polariton device under optical excitation [Lai07, Den10]. Fourier spectroscopy is used to measure the energy-momentum dispersion of the exciton-polaritons. For this purpose, a lens is added to the setup (not shown) to image the back focal plane on the CCD [Lai07]. The grating of the monochromator splits the emission on its frequency contributions on the second axis and the full energy-momentum dispersion can be measured. In figure 5.14 (a) the energy dispersion is shown for a pump power of $0.2 I_{\text{thr}}$. Free excitonic emission can be seen as low intensity, energetically broad, dispersionless band

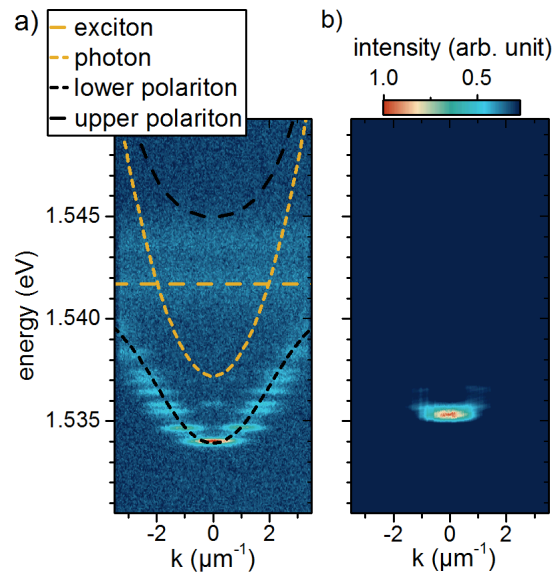


Figure 5.14: Measured energy dispersion of the $\varnothing = 6 \mu\text{m}$ exciton-polariton device 6-1 at 10 K. (a) Below threshold at $0.2 P/P_{\text{thr}}$, the yellow parabolic dashed line indicates the photon dispersion of the cavity mode and the constant dashes line indicates the exciton dispersion. The black dashed lines represent the dispersion of the lower and upper polariton branch. Emission appears at discrete energies on the lower polariton branch due to the three-dimensional confinement of the cavity modes. (b) Above threshold at $2 P/P_{\text{thr}}$, the exciton-polaritons condensate in the ground state and are blue-shifted due to repulsive polariton-polariton interaction in the condensate. The data was measured by M. Klaas at the Technische Physik Würzburg and is published in [Kla18b].

around 1.542 eV and 1.544 eV (803 nm and 804 nm).

The energy-momentum dispersion of polaritonic emission has parabolic characteristics for low momentum k and approaches the constant excitonic energy with increasing k . The lower polariton branch has reduced energy compared to the excitonic emission due to light-matter interaction in the strongly coupled system. The upper polariton branch is likewise parabolic with the minimum energy at 1.545 eV (802.5 nm) and is not occupied due to the high Q factor of 12,000 [Kul10]. Emission from the polariton branch has discrete states which originate from the three-dimensional confinement of the cavity modes similar to QD micropillars. The Hopfield coefficients are calculated via the energy splitting between the bare exciton and photon mode $\Delta E = 4.5 \text{ meV}$, [Hop58, Kav17] which indicate the emission to be around 70 % photonic and 30 % excitonic.

Figure 5.14 (b) shows the energy dispersion above threshold at $2 P/P_{\text{thr}}$. Here, solely emission from the ground mode is visible. The large pump power leads to stimulated scattering of the exciton-polaritons into the macroscopic ground state. The condensed exciton-polaritons emit coherent emission and the device is termed 'exciton-polariton

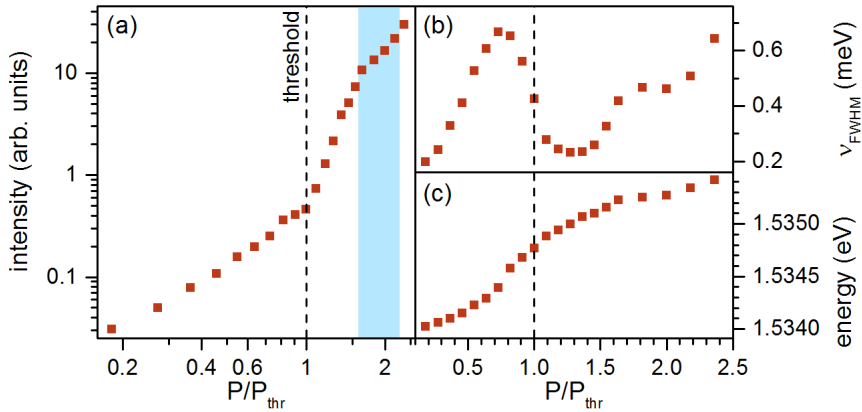


Figure 5.15: Input-output characteristics of the exciton-polariton laser. (a) The double-logarithmic plotted input-output dependence is s-shaped, and thus resembles the characteristic of a conventional photon laser. The light blue-shaded region marks the excitation power range of the TES measurements. (b) The linewidth ν_{FWHM} decreases around threshold (dashed line) and increases above $1.3 P/P_{\text{thr}}$. (c) The emission energy shows a continuous blue-shift due to polariton-polariton interaction in the condensate.

laser’ [Ima96].

The emission peaks from the dispersion measurements are fitted with Lorentzian lineshape in energy. The extracted parameters of the intensity, the linewidth ν_{FWHM} and the energy are plotted in figure 5.15 as a function of the excitation power. A common fingerprint of microlasers is the s-shaped input-output characteristic [Bjö94]. The s-shape also holds for exciton-polariton lasers although it is caused by the onset of stimulated scattering to the polariton ground state and not by population inversion. The required pump powers for exciton-polariton lasers are typically smaller than for photon lasers [Den03]. The s-shape is usually followed by a second nonlinearity at higher pump powers beyond the Mott density indicating the onset of conventional photon lasing [Tem12]. The threshold P_{thr} is determined to be at the start of the nonlinear intensity increase in figure 5.15 (a). The blue-shaded area indicates the range of measurements with the TES.

Two important hints for polariton lasing can be seen in the analysis of the emission linewidth ν_{FWHM} and the energy in figure 5.15 (b) and (c) [Bal07]. Around threshold, the linewidth strongly decreases because of the coherence buildup in the exciton-polariton condensate. With increasing pump power, more polaritons condensate and increase the polariton-polariton interactions [Lov08]. For this reason, the linewidth increases with the pump power below $0.7 P/P_{\text{thr}}$ and above $1.3 P/P_{\text{thr}}$ and is solely reduced in the range of coherence buildup.

The emission energy of the exciton-polariton laser is around 1.535 eV, correspondingly 808 nm. The blue-shift above threshold is caused by increasing polariton-polariton interactions inside the condensate and, mainly below the threshold, also interactions of the exciton-polaritons with excitons [Ciu98, Fer11]. The blue-shift of the exciton-polariton laser supports that the device possesses a polaritonic character above threshold.

Measurement of the Photon Statistics of Exciton-Polariton Lasers

The PND of exciton-polariton lasers is studied to gain more information about the coherence buildup in these devices beyond usual $g^{(1)}(\tau)$ and $g^{(2)}(\tau)$ measurements. Different to the QD micropillar samples in this thesis, the exciton-polariton lasers are optically excited. The pulsed optical excitation necessitates changes in the setup which was presented in section 3.2.

The Ti:Sapphire laser, which excites the exciton-polariton sample, has a fixed repetition frequency of 80 MHz. A pulse picking system based on an acousto-optical modulator (AOM) passes 1:8,000 pulses and thus reduces the excitation frequency to 10 kHz.

The excitation laser pulse intensity varies randomly because of non-perfect pulse picking and is monitored by a photodiode. The present TES measurement includes 40,000,000 pulses (integration time: 100 min) and assigns a photon number n_{ph} to the measured excitation power P for each pulse. With the available data from one single measurement, the PND can be determined for any excitation power P within the measurement range of 1.6 to 2.2 P/P_{thr} .

Pump Power Dependence of the Photon Number Distribution

Figure 5.16 depicts the PND of exciton-polariton laser 6-1 for varied pump powers (c.f. the light blue-shaded area in the input-output characteristics in Fig 5.15). A neutral density filter (NDF) with an optical density (OD) of 0.5 was utilized in the detection path. Panels (a) to (f) show the PND for increasing excitation power. In panel (a), the maximum of the PND is at zero photons and decreases monotonously with n_{ph} . With increasing excitation power shifts the maximum of the PND to a larger photon number n_{ph} which proves the transition to a coherent state.

The simple model of mixed states of thermal and coherent emission, introduced in equation 2.33, is applied to each PND. The parameter $a = \frac{\langle n \rangle_{\text{coh}}}{\langle n \rangle_{\text{coh}} + \langle n \rangle_{\text{ther}}}$ describes the fraction of coherent emission. The model is a good fit for the measured PND with small deviations as can be seen in figures 5.16 (b) to (d). Here, the PND is underrated for $n_{\text{ph}} = 1$ and 2 and overrated for higher photon numbers around $n_{\text{ph}} = 5$.

The fraction of coherent emission a of the exciton-polariton laser 6-1 is plotted in fig-

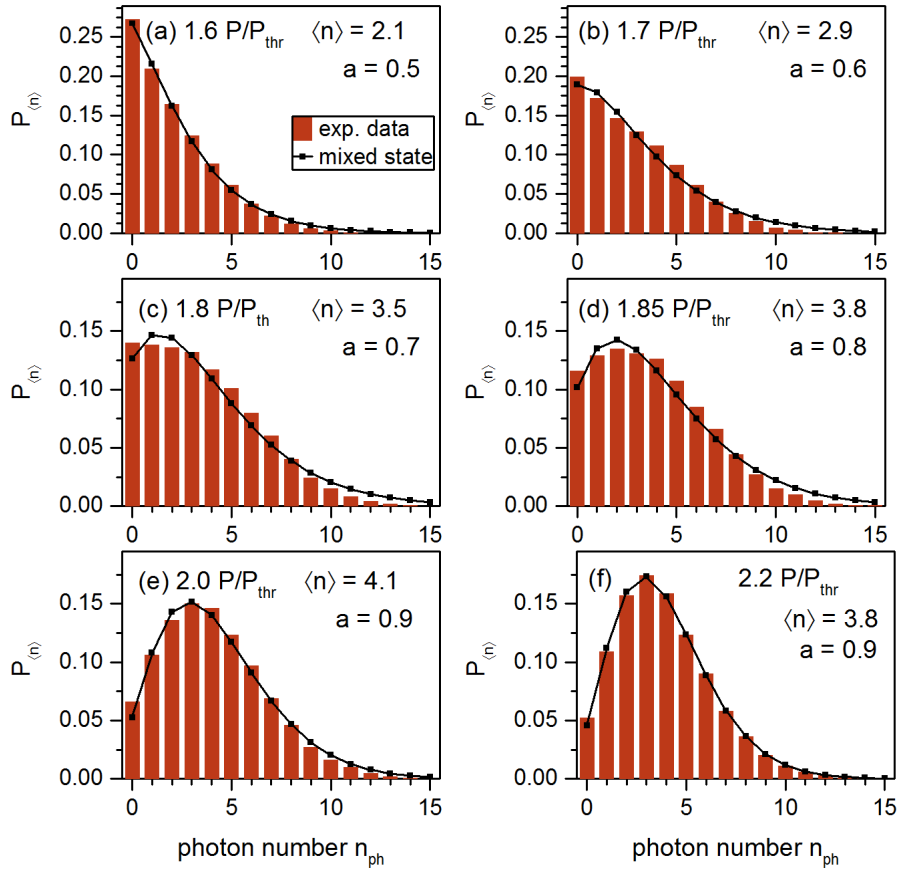


Figure 5.16: PND of exciton-polariton laser 6-1 at excitation powers from $1.6 P/P_{\text{thr}}$ to $2.2 P/P_{\text{thr}}$ with NDF OD 0.5 in the detection path. Mixed states of thermal and coherent emission with the fraction of coherent emission a are fitted to the data and plotted as black dots and solid line, respectively. With increasing pump power, the PND receives a mostly coherent character up to $a = 0.9$.

ure 5.17 in dependence of the pump power. The coherent part increases monotonously from $P/P_{\text{thr}}=1.6$ to 2. Above $P/P_{\text{thr}}=2$, the coherent fraction reaches a constant value of approximately 0.93, i.e. 7% of the emission remains thermal for a high pump power. This finding is in agreement with previous results obtained for exciton-polariton lasers [Hor10, Aßm11, Kla18a].

A second measurement of the PND was taken without an NDF to further analyze the deviations of the model from the experimental data for intermediate excitation powers. In figure 5.18 the PND of exciton-polariton laser 6-1 is shown for the same pump powers as in figure 5.16. Here, the mean photon number $\langle n \rangle$ is larger. Panels (a) and (b) show a decrease of the PND with increasing photon number n_{ph} . A plateau of the PND can be

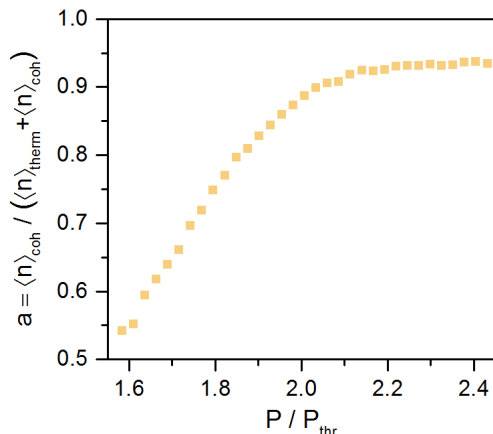


Figure 5.17: Fraction of coherent emission a over the pump power calculated by Hugo Flayac and published in [Kla18b]. The coherent fraction increases between 1.6 and 1.9 P/P_{thr} before it converges to 0.93 for high pump powers.

seen around $n_{\text{ph}} = 5$ and 10 in panel (c) and (d). The model of mixed states is applied to the PND. At a low pump power of 1.6 P/P_{thr} presented in figure 5.18 (a) and for a high pump power of 2.2 P/P_{thr} in panel (f), the fit is in good agreement with the mixed states of thermal and coherent emission. The deviations of the measured PND from the model for excitations powers between 1.7 P/P_{thr} and 2.0 P/P_{thr} are more pronounced in the measurement without a NDF and higher mean photon numbers $\langle n \rangle$. Two possible reasons for the deviations can be identified.

One reason might be of technical nature and caused by the AOM. The excitation pulses are assigned to a pump power by a measurement with a power meter. The AOM influences also the spatial orientation of the laser pulse. It is possible that two pulses with a different spatial profile are assigned to the same pump power but excite the exciton-polariton laser differently. Such a property can cause a PND with two maxima or a plateau which is measured in 5.18 (c) and (d). This explanation is not confirmed with certainty because the spatial profile of the single pulses cannot be determined.

A second reason for the deviations of the PND from mixed states can be the simplicity of the applied model. The condensation in exciton-polariton lasers is very complex and, so far, not fully understood. It is still an open question whether the coherence buildup behaves photon-laser-like or if it rather resembles the condensation in atomic BEC [Byr14]. Correlations between the ground state and excited state of the exciton-polaritons are attributed to a behavior close to a photon laser [Lau04]. Moreover, particle correlations can lead to strong deviations from the classical photon statistics [Sch08].

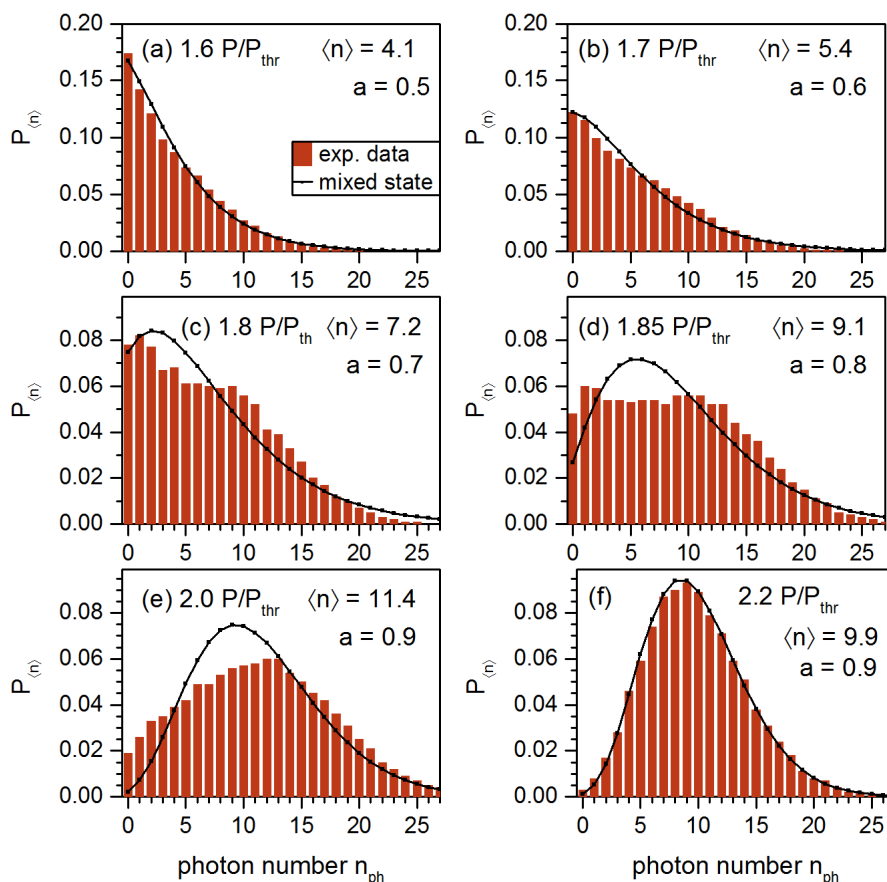


Figure 5.18: PND of exciton-polariton laser 6-1 at excitation powers from $1.6 P/P_{\text{thr}}$ to $2.2 P/P_{\text{thr}}$. The fit of a mixed state of thermal and coherent emission is plotted as black dots and line with the fraction of coherent emission a . For a low pump power of 1.6 and $1.7 P/P_{\text{thr}}$, the PND decreases with the photon number n_{ph} . The PND in panels (c) and (d) shows a plateau and deviations from the mixed state. At a high pump power of $2.2 P/P_{\text{thr}}$, the PND reveals a state with a predominantly coherent character.

The here presented PND provides the opportunity to test various models for the coherence buildup in exciton-polariton lasers. Mixed states of thermal and coherent emission are employed here. Other possibilities are the Scully-Lamb model [Scu67] or different models including interactions in the Bose gas [Kav17].

Although the exciton-polariton device transits to a lasing state (supported by figure 5.15), the mean photon number $\langle n \rangle$ of the PND does not drastically increase with the pump power which can be attributed to a variable effective setup efficiency, as explained in the following. The mean photon number $\langle n \rangle$ is calculated from the PND for each pump power and depicted in figure 5.19. Above $2 P/P_{\text{thr}}$ the mean photon number $\langle n \rangle$ decreases

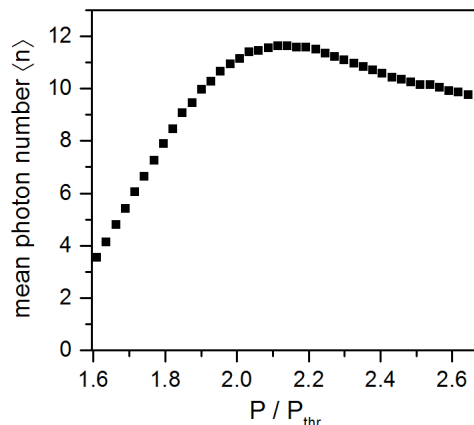


Figure 5.19: Mean photon number $\langle n \rangle$ extracted from the PND of laser 6-1 in dependence of the pump power. The mean photon number $\langle n \rangle$ increases up to $2 P/P_{\text{thr}}$ and further decreases for increasing excitation power.

which is in contradiction to the input-output characteristics in figure 5.15 (a). The mode blue-shifts in energy by about $200 \mu\text{eV}$ (c.f. figure 5.15 (c)) within the pump range of the PND measurements. The spectral shift is converted to a spatial shift of about $20 \mu\text{m}$ by the monochromator which reduces the coupling efficiency to the optical fiber with a core diameter of $5 \mu\text{m}$ after the exit slit (with a width of $50 \mu\text{m}$) of the monochromator. Consequently, the intensity decrease is caused by the non-optimal coupling. However, since the emission linewidth of the exciton-polariton laser $\nu_{\text{FWHM}} \approx 500 \mu\text{eV}$ is larger than the spectral shift, the PND can be determined over a large excitation power range. The setup efficiency changes the mean photon number $\langle n \rangle$ of the PND, but the underlying photon statistics is independent of it.

Second- and Higher-Order Autocorrelation

The autocorrelation function is of particular interest for the understanding of the condensation in exciton-polariton lasers. The second-order autocorrelation function $g^{(2)}(\tau)$ of exciton-polariton lasers has been studied with an HBT in various references with different results. After a coherence buildup and an initially low value of $g^{(2)}(\tau)$, references [Kas08, Aßm11] reported an increase of $g^{(2)}(0)$ with increasing pump power. Other experiments indicated a stable value or decrease of $g^{(2)}(0)$ with increasing pump power [Den02, Lov08, Aßm11, Kla18a]. All of these publications have reported $g^{(2)}(0) > 1$ for high pump powers, indicating that the exciton-polariton laser emission is not purely coherent. The discussed reasons for this behavior are increasing polariton-polariton interactions

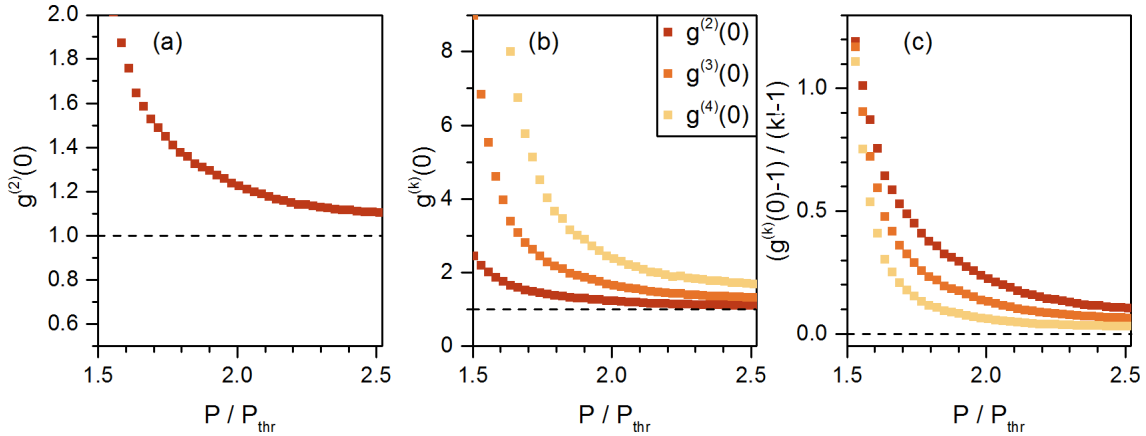


Figure 5.20: (a) Second-order autocorrelation $g^{(2)}(0)$ and (b) autocorrelation $g^{(k)}(0)$ up the fourth order of exciton-polariton laser 6-1, extracted from the PND, in dependence of the excitation power without and (c) with scaling after eq. 5.4. $g^{(2)}(0)$ decreases with the pump power and converges to 1.1. The higher-order autocorrelations follow the same trend with larger values. With a scaling for a comparison of all orders, the higher-order $g^{(k)}(0)$ have lower values.

inside the condensate [Kas08, Lov08], interactions with excitons and polaritons which are non-condensed [Kas08, Lov08, Hor10, Kla18a] as well as the onset of polarized emission [Aßm11].

The calculation of the second-order autocorrelation $g^{(2)}(0)$ and the autocorrelation of k -th order $g^{(k)}(0)$ from the PND via equation 2.31 is introduced in section 2.4. Figure 5.20 (a) shows $g^{(2)}(0)$ of exciton-polariton laser 6-1 in dependence of the excitation power. The autocorrelation values $g^{(2)}(0)$ continuously decrease with increasing pump power and stabilize at a value of approximately $g^{(2)}(0) = 1.1$. The remaining thermal contribution of the emission is in agreement with the model of mixed states and the fraction of coherent emission $a = 0.93$ in figure 5.17. The knowledge of $g^{(2)}(0)$ does not give access to an analysis of the origin of the partly thermal emission at high pump powers. For a deeper insight into the underlying physics, more information about the photon statistics is important. So far, two techniques have been applied to obtain more information about the photon statistics of exciton-polariton lasers. In reference [Hor10] the HBT was expanded for a measurement of the third-order autocorrelation function $g^{(3)}(\tau)$ with an additional beam-splitter and SPCM. The correlations $g^{(2)}(0)$ and $g^{(3)}(0)$ close to 1 around threshold and a slight increase to 1.4, respectively 2.5, for increasing pump caused by polariton scattering was reported.

To compare the autocorrelation functions of different orders with each other, a scaling

which maps the coherent emission for all orders to 0 and thermal emission to 1 was established. The scaling is introduced and discussed in equation 5.4.

In figure 5.20 (b), $g^{(k)}(0)$ up to the fourth order is depicted for exciton-polariton laser 6-1 in dependence of the excitation strength. The observed values are higher with increasing order k . For large pump power we observe $g^{(3)}(0) = 1.3$ and $g^{(4)}(0) = 1.7$. In contrast, with the scaling, $g_{\text{scale}}^{(k)}(0)$ is lower for increasing order k which implies a decrease of the deviation from a coherent state with the order k . The scaling was not applied in reference [Hor10], but one can see that the third-order autocorrelation $g^{(3)}(0)$ behaves similar to our experimental results in figure 5.20 (c). In contrast, the results presented in [Aßm09] report an increase with the order k when the scaling is applied. Both references used simple planar samples without lateral confinement. In [Aßm09], the device showed strong coupling below threshold and a transition to the weak coupling regime with increasing pump, while our device operates in the strong coupling regimes for all applied excitation powers. Thus, we attribute the different behavior of the autocorrelation to the different sample characteristics.

The exciton-polariton laser 6-1 is found to be well described, with some deviations, by the mixed states of thermal and coherent emission. The behavior of $g^{(2)}(0)$ is close to that of a photon laser. The results are in good agreement with the mainly photonic character of the emission (70 %). Overall, the TES-based photon number resolved measurements of exciton-polariton lasers enable important additional insight in the photon statistics which cannot be obtained by simple HBT measurements. We consider this technique very interesting for further investigations of various polariton lasers to gain more understanding of the manifold effects involved in the condensation and emission processes.

In conclusion, the photon statistics of QD micropillar lasers and exciton-polariton lasers have been studied in this chapter. The QD micropillar laser sample is excited by electrical pulses whose influence on the input-output characteristics was discussed. The PND was determined for a stable and a bistable bimodal QD micropillar lasers. The stable microlaser showed a transition from thermal to coherent statistics for the strong mode and to thermal statistics with fluctuations for the weak mode. In contrast, the bistable microlaser revealed a linear combination of a thermal and a coherent distribution for both modes. The difference between the emission behavior of the two lasers was not accessible by HBT based $g^{(2)}(\tau)$ measurements and could only be revealed by photon number resolved measurements using a TES detection system, which clearly highlights the huge potential of this advanced quantum optical measurement technique for the in-depth study of nanophotonic devices.

Beyond the study of conventional photon lasers, the PND of the exciton-polariton laser was determined to gain the full photon statistics of emission for this type of semiconductor laser. The evaluation of the experimental data reveals a transition from thermal to coherent emission and is described by the model of mixed states of thermal and coherent emission. The studied laser device has a mainly photonic character which is in agreement with the model.

6 Optical Injection Experiments in Quantum Dot Micropillar Lasers

Spontaneous emission enhanced QD micropillar lasers are excellent candidates to investigate nonlinear dynamics in the low-power regime. Dynamics can be induced by external perturbations, e.g. optical injection. In this chapter, we present optical properties of electrically driven QD micropillar lasers under optical injection by an external tunable laser. In the first section 6.1, experiments with a single mode QD micropillar laser are performed. The fundamental mode of QD micropillar lasers has usually two polarization components. In the single mode case, the second polarization component was very low in intensity and could be neglected. The QD micropillar laser is injection locked to the master laser within the locking range. Close to the locking range the new effect of partial injection locking is observed in the high- β microlaser and is investigated by spectral and temporal measurements. The results of this section are published in [Sch16].

Section 6.2 focuses on bimodal QD micropillar lasers which two polarization components of the fundamental emission mode show competing intensities. Either the lasing strong or non-lasing weak mode are subject to optical injection and the response of both modes is analyzed. Injection into the non-lasing weak mode can provoke stochastic switching events between the weak and the strong mode. The results of this section are published in [Sch19].

6.1 Optical Injection in Single QD Mode Micropillar Lasers

The measurements in this section are performed on QD micropillar laser 5-1 from sample A (q.v. section 3.1) with a diameter of $5\mu\text{m}$ at a temperature of 13 K. First, the input-output characteristics of the microlaser are discussed. Subsequent, maps of the phase-locking and optical spectra of QD micropillar laser 5-1 under optical injection are presented. The section closes with measurements of the second-order autocorrelation.

The input-output characteristics of QD micropillar 5-1 are presented in figure 6.1. Panel (a) shows a spectrum of the two microlaser modes with an emission wavelength of approximately 848.85 nm. The intensity is scaled to an intracavity photon number of $\langle n_{\text{ph}} \rangle = 1$ at

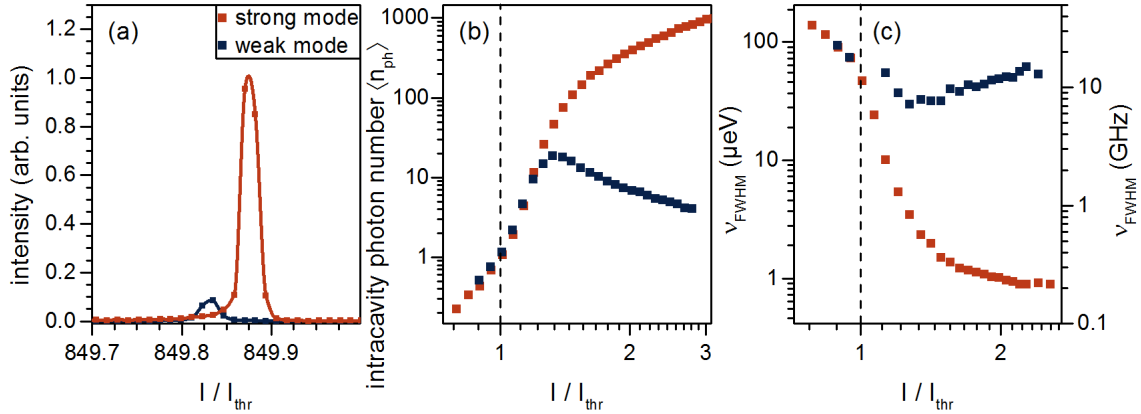


Figure 6.1: (a) Emission spectrum at $1.6 I/I_{thr}$ shows emission of the strong mode at 849.88 nm and the weak mode at 849.8 nm. (a) Emission intensity and (b) linewidth characteristic of QD micropillar 5-1 at 13 K in dependence of the excitation power. The input-output curve follows the typical s-shape. The linewidth strongly reduces around the threshold (dashed line).

the threshold of $I_{thr} = 23.5 \mu\text{A}$ (dashed line). The strong mode shows the typical s-shape for microlasers. The weak mode increases superlinearly in intensity at the threshold, but decreases above $1.3 I/I_{thr}$ and is suppressed by more than -20 dB compared to the strong mode for pump currents above $2 I/I_{thr}$. The weak mode is not considered in the experiments of this section because of its low intensity and the QD micropillar is considered as single mode laser.

The linewidth of the QD micropillar laser's strong mode narrows with the pump strength and reaches the resolution limit (6.5 GHz) of the spectrometer around the threshold. The data above threshold is measured with an FPI (0.1 GHz resolution) and decrease to $\nu_{FWHM} = 0.2 \text{ GHz}$ at $I/I_{thr} = 2.2$. The β factor of QD micropillar 5-1 is estimated by rate equations to $\beta = 0.02$ [Sch16]. The Q factor of the microlaser mode is determined to $Q \sim 21,000$. The α -factor is estimated via numerical modeling of the QD micropillar laser in agreement with the experimental above-threshold linewidth to amount $\alpha = 2$ [Sch16].

Phase-Locking: Locking Cone

For the injection locking experiments, QD micropillar 5-1 acts as slave laser and is optically injected by an external tunable master laser. The optical signals of the master and the microlaser are interfered to investigate phase-locking. The master laser is linearly polarized and aligned to match the strong mode polarization angle of the QD micropillar laser. Details on the used experimental scheme are given in section 3.2. The amplitude of the

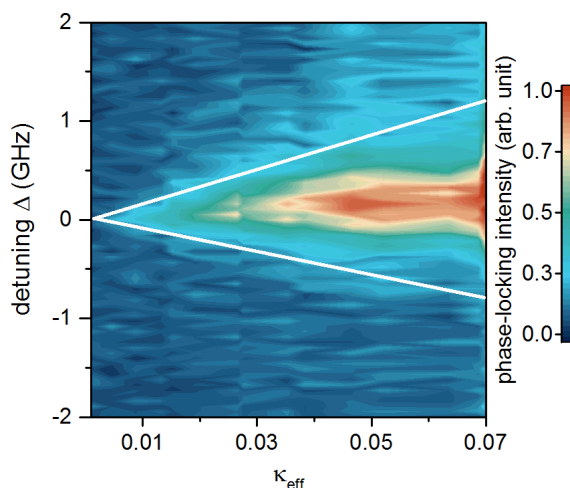


Figure 6.2: Phase-locking map of single mode QD micropillar laser 5-1 at $I/I_{\text{thr}} = 1.6$. The microlaser shows slightly asymmetric phase-locking around zero detuning. The range of phase-locking is indicated with white lines and increases with the injection strength κ_{eff} .

interference pattern is a measure for the phase-locking of the slave to the master laser. The amplitude is plotted in linear color code in dependence of the effective injection strength κ_{eff} and the detuning Δ in figure 6.2. The detuning is defined as the difference between master and slave frequency $\Delta = \omega_{\text{inj}} - \omega_{\text{S}}$. The injection strength is defined by

$$\kappa = \sqrt{\frac{P_{\text{inj}}}{P_{\text{S}}}} \quad (6.1)$$

and depends on the measured emission power of the slave laser P_{S} and the master laser P_{inj} . The pump current was set to $I/I_{\text{thr}} = 1.6$ which leads to $P_{\text{S}} = 470$ nW in the injection experiments. The effective injection strength $\kappa_{\text{eff}} = 0.1 \kappa$ is estimated by theoretical simulations of the locking cone and considers reflections on the micropillar surface and non-ideal incoupling of the injected laser signal [Sch16].

The locking cone in figure 6.2 shows the phase-locking intensity in linear color code. For $\kappa_{\text{eff}} = 0.07$, the micropillar laser is slightly asymmetric phase-locked to the master between $-0.8 \text{ GHz} < \Delta < 1.2 \text{ GHz}$. The locking width increases with κ_{eff} as discussed in the theory chapter 2.3.

Optical Spectrum of a QD Micropillar Laser under Optical Injection

To investigate the frequency locking of QD micropillar laser 5-1, high resolution spectra were measured with an FPI (100 MHz resolution). The master laser and slave laser emis-

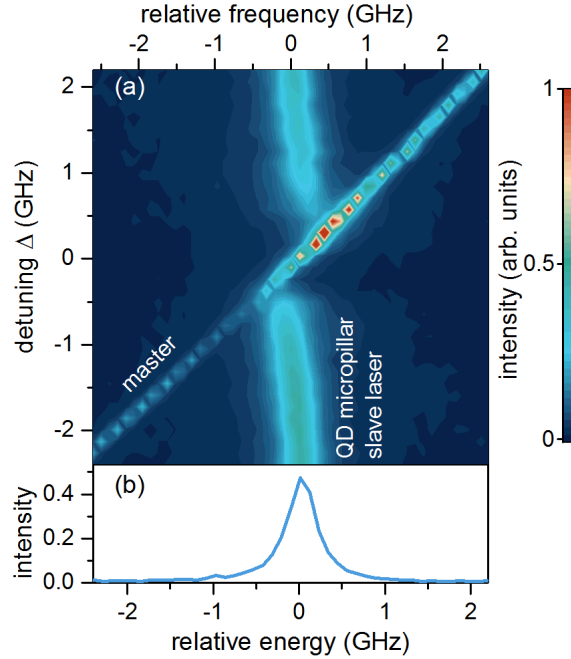


Figure 6.3: (a) Intensity heat map of QD micropillar laser 5-1 at $1.6 I/I_{\text{thr}}$ injected by a master laser with $\kappa_{\text{eff}} = 0.054$. The master laser is tuned from -2.6 to +2.6 GHz corresponds to the diagonal line. The slave laser is pulled towards the master laser at small detunings and decreases in intensity with reduced detuning $|\Delta|$. The master laser intensity is enhanced between -0.5 and 1 GHz. (b) Spectrum of the non-injected QD micropillar laser.

sion are well separated in the spectra. Frequency, intensity and linewidth of the peaks in the spectra are analyzed and discussed in the following.

Partial Injection Locking

For an optimal presentation of the emission spectra of QD micropillar 5-1, the intensity is plotted in linear color code in dependence of the relative frequency and the detuning Δ in figure 6.3 (a). The microlaser is driven at $1.6 I/I_{\text{thr}}$ and a spectrum of the non-injected micropillar emission is plotted in panel (b). The relative frequency is set to zero at the slave laser frequency. The master laser with an injection strength of $\kappa_{\text{eff}} = 0.054$ is tuned in frequency from -2.6 to +2.6 GHz relative to the slave laser frequency.

The master laser emission in the heat map in figure 6.3 (a) appears as a diagonal line. The micropillar laser has a broad linewidth of about $\nu_{\text{FWHM}} = 0.39$ GHz compared to the resolution limited signal of the master laser (100 MHz). For detunings $|\Delta| < \pm 2$, the slave laser is pulled towards the master laser frequency. The intensity of the master laser increases in a detuning range of $\Delta = -0.5$ and 1.5 GHz up to a factor of 6.

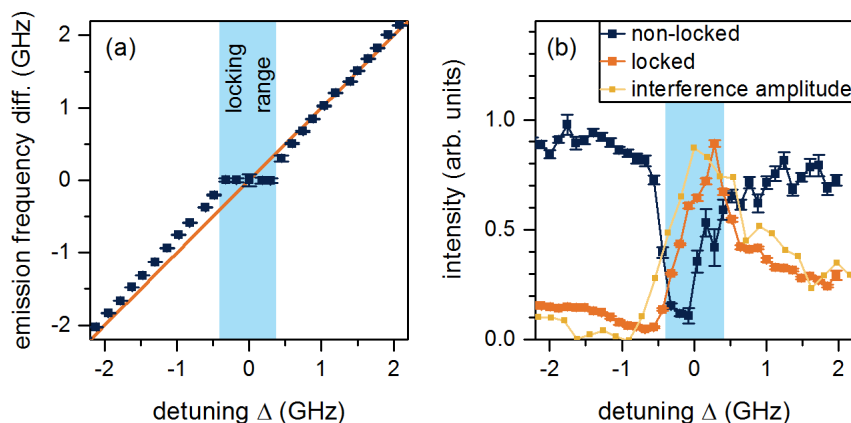


Figure 6.4: (b) Difference of the master and slave emission energies with $\kappa_{\text{eff}} = 0.054$ in dependence of the detuning Δ shows the frequency locking between ± 0.4 GHz. (a) Intensity of the locked and non-locked emission peaks from the spectra presented in figure 6.3 in dependence of the detuning Δ . The locked intensity (orange) is in good agreement with the interference amplitude (yellow) extracted from figure 6.2. The locked intensity increases in a larger range than the suppression of the non-locked emission.

The locking range is defined as the range, where the slave laser is adapted to the master laser's frequency. Interestingly, the master laser is also enhanced outside the locking range for positive detuning Δ while the slave laser decreases in intensity. In this region, the micropillar laser emits simultaneously on its 'non-locked' frequency and the 'locked' master frequency. We term this behavior 'partial injection locking' [Sch16].

This partial locking behavior has not been reported previously for conventional low- β lasers. In multimode lasers, e.g. with additional polarization modes [Val07] [Gat06] or higher-order modes in a VCSEL [Hon02] an incomplete suppression of these modes was observed by optical injection because of a gain shift towards the master laser. The injected mode in the discussed references is either not locked or fully locked to the master laser, but not partially locked. In contrast, the here presented measurements are performed with a single mode laser.

The emission peaks of the master laser and the QD micropillar slave laser in the spectra presented in figure 6.3 (a) are fitted with a Lorentzian lineshape to extract the emission intensity and frequency. Figure 6.4 (a) shows the measured frequency difference $\omega_{\text{inj}} - \omega_{\text{sl,nl}}$ in dependence of the nominal detuning $\Delta = \omega_{\text{inj}} - \omega_{\text{sl,0}}$. Hereby, $\omega_{\text{sl,0}}$ is the solitary QD micropillar laser frequency without injection and $\omega_{\text{sl,nl}}$ the QD micropillar laser frequency determined from the spectra. Over a large range of detunings, the absolute value of the emission frequency difference is lower than the nominal detuning between master and slave

laser and reduced to zero in the locking range between -0.4 and 0.4 GHz. The locking range is expected to depend on the linewidth enhancement factor α via [Pet88, Oht12]

$$-\Delta_{LC}\sqrt{1+\alpha} < \Delta < \Delta_{LC} . \quad (6.2)$$

Δ_{LC} describes the extent of the locking cone in positive detuning direction. However, the locking range of QD micropillar laser 5-1 is found to be nearly symmetric around the detuning Δ and the estimated $\alpha = 2$ appears to be overestimated.

The intensity in dependence of the detuning is depicted in figure 6.4 (b). The non-locked part of the QD micropillar emission (dark blue line and dots) is sharply suppressed between a detuning of $\Delta = -0.5$ GHz and 0 GHz. For positive detunings, the non-locked intensity increases slowly between 0 and 1 GHz. The locked part (orange) enhances the master laser emission between -0.5 and 1 GHz. This pattern is in very good agreement with the interference amplitude of master and slave emission (c.f. 6.2) plotted in yellow. A simultaneous emission of the locked and non-locked part occurs between a detuning of $0 \text{ GHz} < \Delta < 0.5 \text{ GHz}$.

Noteworthy is the suppression of the master laser for small negative detunings $-1 \text{ GHz} < \Delta < 0 \text{ GHz}$. The intensity of the master laser differs outside the locking region for negative $\Delta < -1 \text{ GHz}$ and positive detunings $\Delta > 1 \text{ GHz}$. The intensity deviation of the master laser in these regions can be attributed to destructive interference between emission of the cavity and the reflected master laser signal from the micropillar surface.

The effect of partial injection locking in high- β microlasers is further investigated by spectra of QD micropillar laser 5-1 under optical injection taken at a fixed detuning of $\Delta = 0.5 \text{ GHz}$ and varied injection strength κ_{eff} . The 2D map of the spectra is depicted in figure 6.5 (a). At low injection strength of $\kappa_{\text{eff}}=0.01$, the non-locked emission is bright while the master laser is not visible in the spectrum. With increasing κ_{eff} , the non-locked intensity decreases while the locked intensity increases. Simultaneously, the QD micropillar slave laser is frequency pulled towards the master with increasing injection strength as predicted from Adler's equation (c.f. figure 2.11, the frequency pulling depends on the coupling strength a). Between $\kappa_{\text{eff}} = 0.02$ and 0.045, non-locked and locked emission is clearly visible in the spectra and the QD micropillar laser is partially locked.

Similar to figure 6.2, the emission peaks of master and slave are fitted with Lorentzian lineshapes and the extracted intensities are plotted in figure 6.5 (b) as function of the injection strength. For low and high injection strength κ_{eff} , the intensity of the non-locked part decreases weakly. Between $\kappa_{\text{eff}} = 0.04$ and 0.045, the non-locked intensity decreases strongly. The locking range increases with the injection power κ_{eff} and locks the QD micropillar laser with a fixed detuning of $\Delta = 0.5 \text{ GHz}$ around $\kappa_{\text{eff}} = 0.45$.

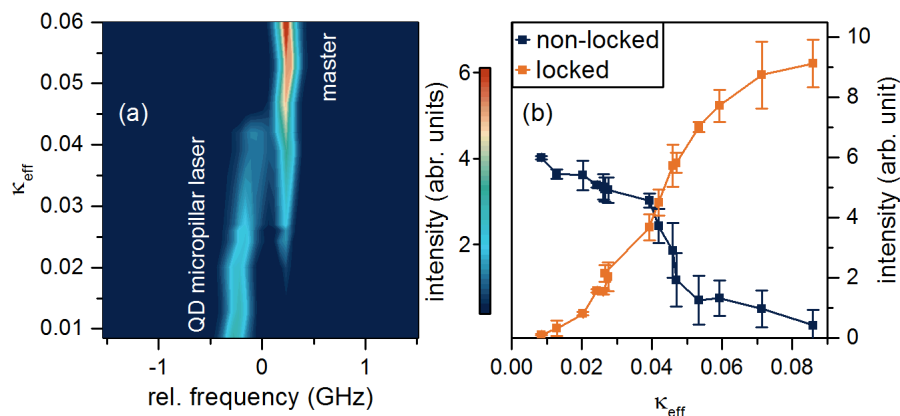


Figure 6.5: (a) Heat map of spectra from QD micropillar laser 5-1 under optical injection with a fixed detuning $\Delta = 0.5$ GHz and varied injection strength κ_{eff} . The non-locked intensity decreases continuously with increasing κ_{eff} and is pulled towards the master laser frequency. (b) The intensity of the locked emission increases and the non-locked microlaser emission decreases with increasing injection strength κ_{eff} .

Numerical Calculation of the Laser Intensity under Optical Injection for Varied β Factors

Semiclassical rate equations are used to model the QD micropillar laser intensity and gain. The model includes electron scattering mechanisms into the QD [Lin15b]. The noise modeling is based on the quantum Langevin approach in the weak coupling regime. The simulations are conducted for different β factors to study the influence of the spontaneous emission on the emission behavior under optical injection. The numerical model was developed and the simulations were performed by Benjamin Lingnau and Kathy Lüdge from Technical University of Berlin. A detailed description of the model can be found in [Sch16]. In figure 6.6 (a), the fraction of the locked intensity I_{locked} and the total intensity $I_{\text{total}} = I_{\text{locked}} + I_{\text{non-locked}}$ is depicted in dependence of the injection strength κ_{eff} for the experimental data and the theoretical simulations. The locked intensity increases with κ_{eff} for all β factors. For lower β factors, the laser has a critical injection strength κ_{crit} at which the locked intensity I_{locked} increases fast. The injected laser is fully locked to the master laser when $I_{\text{locked}}/I_{\text{total}} = 1$. For high β factors between 0.02 and 1, the fraction $I_{\text{locked}}/I_{\text{total}}$ is significantly lower than for low β factors. For example at $\kappa_{\text{eff}} = 0.1$, the fraction of locked emission $I_{\text{locked}}/I_{\text{total}}$ is 0.3 or 0.04 for $\beta = 0.2$ or 1, respectively, and the laser emits mostly on its solitary frequency.

The simulations of the input-output characteristics for QD micropillar laser 5-1 revealed $\beta = 0.02$ and are in very good agreement with the injection locking experiments. The simulations support the important result that the partial injection locking is an effect

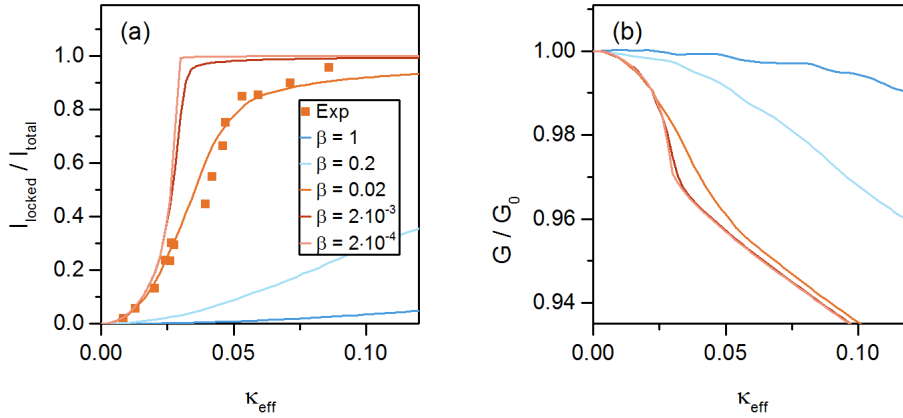


Figure 6.6: (a) Locked intensity I_{locked} scaled to the total intensity I_{total} of a laser under optical injection at fixed detuning $\Delta = 0.5$ GHz in dependence of the injection strength κ_{eff} . The dots correspond to the experimental data of QD micropillar laser 5-1 and the lines to theoretical simulations for different β factors. Low β factors lead to a rather abrupt increase of I_{locked} , while for large β the intensity is not fully locked in the whole range of injection strengths. (b) Simulated gain of the QD micropillar laser G scaled to the gain without injection G_0 for varied κ_{eff} . G decreases fast at $\kappa_{\text{eff}} \approx 0.025$ for low β . The gain is significantly less influenced for increasing β .

caused by the large fraction of spontaneous emission and does not occur for conventional low β lasers.

The simulated gain of the QD micropillar normalized to the gain without injection G/G_0 is depicted in figure 6.6 (b). The gain is strongly reduced for low β factors at the critical injection strength $\kappa_{\text{eff}} = 0.025$ while it decreases weakly for larger β . This progression leads to an explanation for the occurrence of partial injection locking for high- β lasers. Because of the high spontaneous emission in cQED enhanced microlasers, lasing on the master lasers frequency of the locked emission is achieved already at a low threshold I_{thr} and the gain is clamped at a low value. The available gain for emission on the solitary slave laser frequency is less reduced than for conventional low β lasers. Hence, more emission remains non-locked with increasing β . In contrast, the gain of the locked emission is clamped to a larger value for low β factors. Significantly less gain is available for the non-locked emission and partial injection locking is not observed for low β -lasers.

Temporal Dynamics of QD Micropillar Lasers under Optical Injection

The simultaneous emission of the QD micropillar laser on two frequencies is to be proven by measurements of the temporal dynamics with an HBT configuration. For the first measurement, the optical signal is spectrally filtered by a monochromator. In this case, the

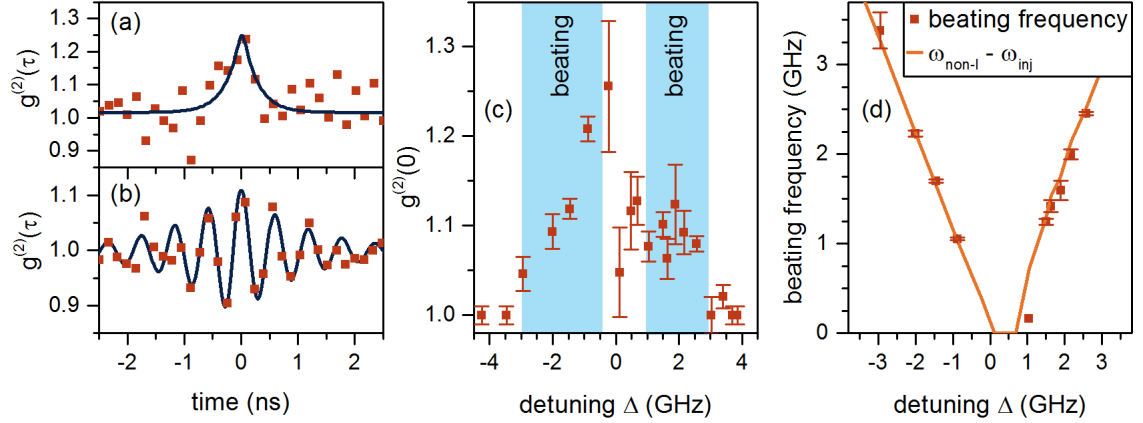


Figure 6.7: Second-order autocorrelation function of QD micropillar 5-1 at $1.6 I/I_{\text{thr}}$ under optical injection with $\kappa_{\text{eff}} = 0.064$. (a) Exemplary $g^{(2)}(\tau)$ at $\Delta = -0.2$ GHz. The microlaser is locked to the master and $g^{(2)}(0) = 1.26$. (b) $g^{(2)}(\tau)$ at $\Delta = -1.5$ GHz. In the partial locking regime, master and non-locked slave emission interfere and show a beating which is fitted with a sinusoidal function. (c) $g^{(2)}(0)$ in dependence of the detuning. The blue shaded region indicates the regime of beating. (d) The beating frequency (red squares) from the sinusoidal fit and the frequency difference $\omega_{\text{non-l}} - \omega_{\text{inj}}$ (orange line) determined from the FPI spectra are in agreement.

signal includes the master and the non-locked slave laser emission. In a second measurement, the HBT measurement is performed after a high-resolution FPI to separate master and non-locked slave laser emission and records the individual photon statistics.

Photon Correlation of the Combined Master and Slave Laser Emission

The emission signal of the QD micropillar laser and the master laser is filtered by a monochromator with a resolution of 6.5 GHz and connected to a HBT configuration. Thus, the contributions of master and slave are not separated and the combined emission is detected.

Two exemplary HBT measurements are presented in figure 6.7. Panel (a) shows $g^{(2)}(\tau)$ inside the locking range at $\Delta = -0.2$ GHz. $g^{(2)}(\tau)$ is fitted with equation 4.2 and $g^{(2)}(0) = 1.26$ is extracted. For panel (b), $g^{(2)}(\tau)$ is measured close to the locking range at $\Delta = -1.5$ GHz. $g^{(2)}(0)$ describes a damped sinusoidal function and is fitted with the formula $g^{(2)}(\tau) = 1 + A \cdot \sin\left(\frac{f_{\text{beat}}}{2\pi} \cdot \tau\right) \cdot e^{-|\tau/\tau_{\text{damping}}|}$. Two interfering emission contributions, non-locked slave laser emission and master laser emission, are beating. The beating frequency f_{beat} depends on the frequency difference of both and the damping on the coherence time. The occurrence of beating is a clear evidence of a simultaneous emission of

the injected QD micropillar laser at its solitary frequency and the master frequency. $g^{(2)}(0)$ is plotted in dependence of the detuning in figure 6.7 (c). Beating occurs in the blue shaded region and $g^{(2)}(0)$ corresponds to the amplitude of the sinusoidal fit. For larger detunings $|\Delta| > 3$ GHz beating is still expected, but cannot be resolved with the single-photon detectors with a timing resolution of $\tau_{\text{res}} = 56$ ps. Inside the locking range for $|\Delta| < 1$ GHz, the QD micropillar laser is fully locked to the master laser and coherent emission is expected. Interestingly, $g^{(2)}(0)$ is larger than 1 in the locking range. However, the error bars of $g^{(2)}(0)$ are large and the origin of $g^{(2)}(0) > 1$ remains ambiguous. Hints for chaotic laser dynamics at the edge of the locking cone, e.g. $g^{(2)}(0) > 2$, are not observed in the present experiments. This could be explained by the fact that quantum fluctuations are enhanced in microlasers [Wim14, Sat16] and are known to strongly suppress chaotic dynamics as discussed for dynamics in optomechanical systems [Bak15]. The beating frequency (red squares) and the frequency difference $\omega_{n-1} - \omega_{\text{inj}}$, extracted from FPI spectra, are plotted in figure 6.7 (c) in dependence of the detuning Δ . The frequencies match perfectly and support the explanation of the experimental data in terms of the interference of master and non-locked slave laser emission. The beating is not measurable for detunings $|\Delta| > 3$ GHz because of a beating faster than the temporal resolution of the HBT and the resulting $g^{(2)}(\tau) = 1$.

Photon Correlation of the Individual Master and Slave Emission

The photon statistics of the individual master and QD micropillar laser emission can be determined via an HBT measurement with spectral filtering by a high resolution FPI. An exemplary spectrum and the used filter width of the FPI (shaded region) are depicted in figure 6.8 (a).

The photon autocorrelation function $g^{(2)}(\tau)$ is fitted with equation 4.2 and the extracted $g^{(2)}(0)$ values are plotted in 6.8 in dependence of (b) the detuning Δ and (c) the injection strength κ_{eff} . The master laser is a coherent light source with $g^{(2)}(0) \approx 1$ independent of the detuning and clarified by a dashed orange line in panel (b). Without injection, the slave laser has $g^{(2)}(0)=1.6$ as presented in panel (b) and $g^{(2)}(0)=1$ depicted in panel (c). Between both measurements, the sample experienced a cool-down cycle leading to slightly different emission characteristics. The pump current was set for both measurements to 42 μA , but the emission linewidth of the QD micropillar laser was 310 MHz for the measurement in figure 6.8 (b), respectively 160 MHz for the measurement presented in panel (c). The varying linewidths and the trace of $g^{(2)}(0)$ imply that the injection experiments result in a mixed state of thermal and coherent emission of the QD micropillar for the data presented in panel (b) and in a predominantly coherent state in case of the results shown in panel

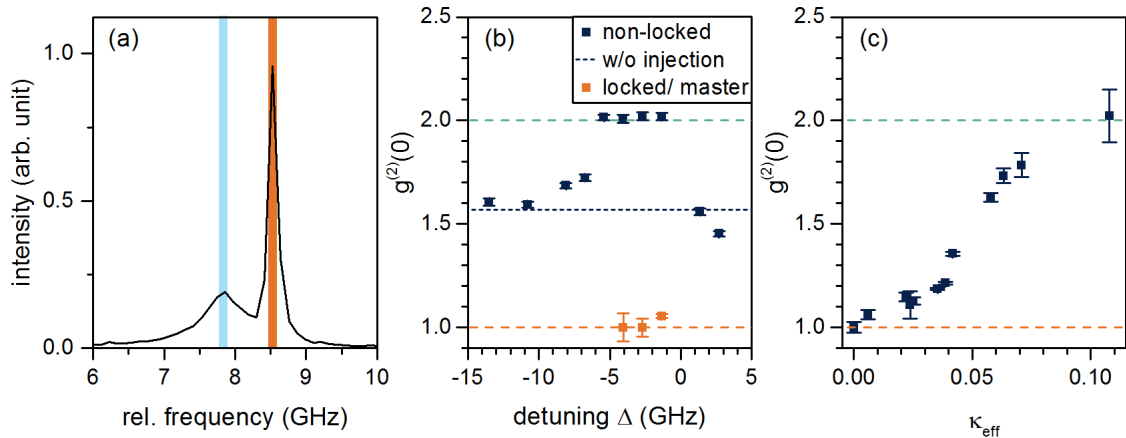


Figure 6.8: Second-order autocorrelation $g^{(2)}(0)$ of the individual master and slave emission of QD micropillar 5-1. (a) Exemplary FPI spectrum of the optically injected QD micropillar 5-1 in the regime of partial injection locking. The shaded regions indicate the filtered range for the following HBT measurement in light blue for the slave and in orange for the master laser. (b) $g^{(2)}(0)$ in dependence of the detuning Δ for $\kappa_{\text{eff}} = 0.04$. The dashed line at $g^{(2)}(0) = 1.57$ indicates the autocorrelation of the microlaser without injection. $g^{(2)}(0)$ of the microlaser increases for negative detuning up to the thermal limit of 2 for $-7 \text{ GHz} < \Delta < 0$. (c) $g^{(2)}(0)$ in dependence of the injection strength κ_{eff} for a fixed detuning $\Delta = -3.3 \text{ GHz}$. The correlation value $g^{(2)}(0)$ increases from coherent to thermal emission with increasing κ_{eff} .

(c).

The autocorrelation values $g^{(2)}(0)$ in dependence of the detuning are depicted in figure 6.8 (b). $g^{(2)}(0)$ increases between $\Delta = -7$ and 0 GHz to the maximum of $g^{(2)}(0) = 2$ which indicates a thermal character of the non-locked microlaser emission in this detuning range. Panel (c) shows $g^{(2)}(0)$ in dependence of the injection strength κ_{eff} for a detuning $\Delta = -3.3 \text{ GHz}$. With increasing injection strength κ_{eff} , $g^{(2)}(0)$ of the non-locked QD micropillar emission increases continuously from 1 to 2 until the slave laser reaches the thermal limit of 2.

We can conclude that the QD micropillar laser is partially locked and the remaining non-locked emission at a high injection strength $\kappa_{\text{eff}} = 10$ is caused by spontaneous emission. The master laser reduces the available gain on the non-locked frequency and disrupts the stimulated emission. However, the remaining gain leads to spontaneous emission on the QD micropillar laser frequency with a thermal character and high temporal coherence inherited from the locked mode component. Panel (c) shows that the photon statistics of a high- β microlaser can be tailored with optical injection.

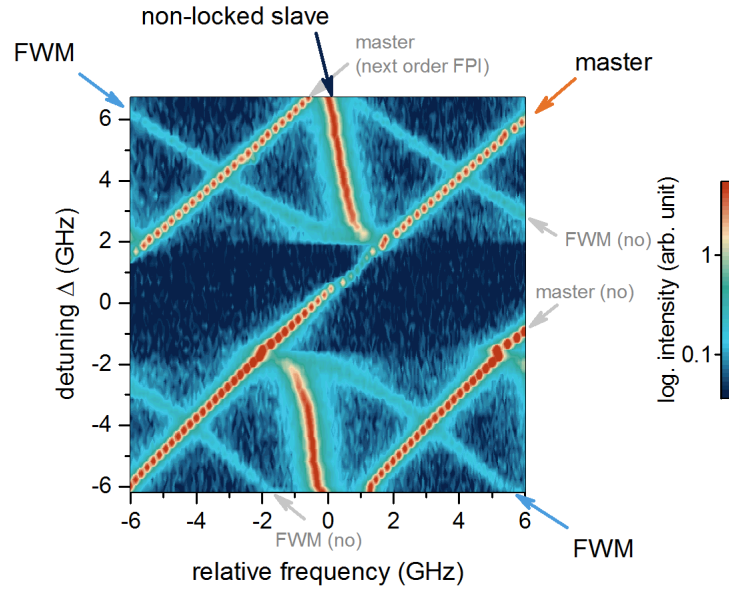


Figure 6.9: Intensity heat map of QD micropillar laser 5-1 at $1.6 I/I_{\text{thr}}$ with $\kappa_{\text{eff}} = 0.066$ in logarithmic scaling. The contributions of the next FPI orders are labeled in grey and should be disregarded. The unperturbed microlaser emission is observed at a relative frequency of 0 GHz. The master laser is tuned in frequency. Outside the locking range of ± 2 GHz, contributions of FWM are visible at $\omega_{\text{FWM}} = 2 \cdot \omega_{n-1} - \omega_{\text{inj}}$.

Four Wave Mixing in Injection Locking Experiments on QD Micropillar Lasers

Two emission frequencies in the nonlinear semiconductor material lead to four-wave mixing (FWM) and the appearance of a third emission frequency [Nak85a, Nie89]. With optical injection in a semiconductor laser, FWM is expected to occur outside the locking area due to a mixing of the master and the slave laser emission. In the heat map of QD micropillar 5-1 presented in figure 6.3 with $\kappa_{\text{eff}} = 0.054$, no contributions of FWM are visible in linear and logarithmic (not shown) scaling of the intensity. With a slightly higher injection strength of $\kappa_{\text{eff}} = 0.066$ and a logarithmic intensity scaling in figure 6.9, FWM clearly appears in the emission spectra. Outside the locking range, the emission spectra exhibit the frequencies of the QD micropillar slave laser, the master laser and FWM.

Figure 6.9 shows the intensity of QD micropillar laser 5-1 under optical injection with $\kappa_{\text{eff}} = 0.066$ in logarithmic color code in dependence of the relative frequency and the detuning Δ . The relative frequency is set to zero at the non-injected microlaser emission frequency. The shown detuning range of ± 6 GHz is larger than the free spectral range of the FPI (FSR= 7.5 GHz). The emission peaks of the adjacent orders of the FPI appear in the spectra and are marked with grey labels. The QD micropillar laser is locked to

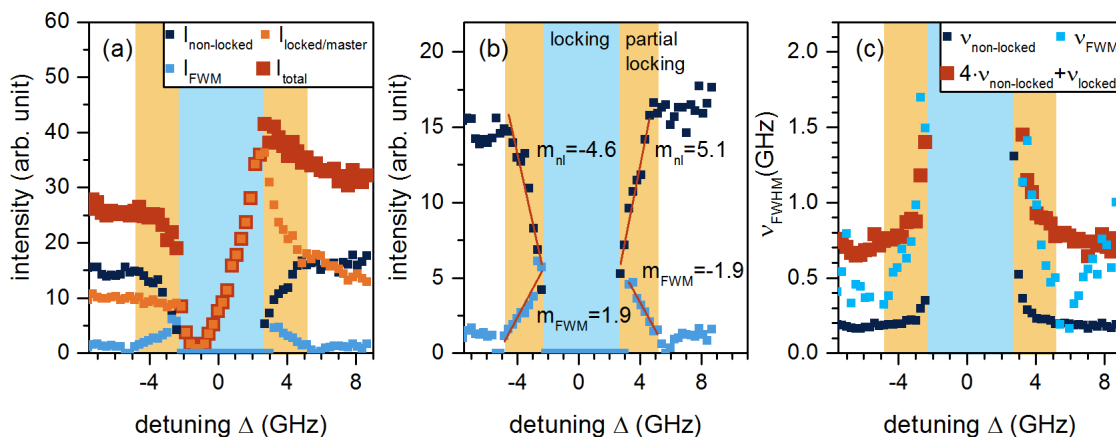


Figure 6.10: (a) Intensity of QD micropillar 5-1 under optical injection with $\kappa_{\text{eff}} = 0.066$ in dependence of the detuning Δ . The frequency components of the non-locked intensity I_{n-1} are plotted in dark blue, master intensity I_{inj} in orange and the FWM intensity I_{FWM} in blue. The total intensity $I_{\text{total}} = I_{n-1} + I_{\text{inj}} + I_{\text{FWM}}$ is plotted in red. I_{FWM} increases with decreasing detuning $|\Delta| < 5$ GHz. (b) The intensity of the non-locked slave laser emission and the FWM is linearly fitted nearby the locking range. (c) The linewidth of the non-locked QD micropillar emission and the FWM increases close to the locking range for detunings $|\Delta| < 4$ GHz. The measured FWM linewidth ν_{FWHM} (light blue dots) is compared to the linewidth calculated after equation 6.3 (big red dots).

the master laser in a locking range of about ± 2 GHz and is frequency pulled towards the master frequency outside the locking range.

A third emission peak is visible outside the locking range and is attributed to FWM due to its frequency of $\omega_{\text{FWM}} = 2 \cdot \omega_{n-1} - \omega_{\text{inj}}$ [Ern10]. Three spectral components in a nonlinear optical medium enhance the intensity of an additional frequency component. In degenerate FWM, two frequency components are identical which is the case here for the non-locked frequency. For further analysis, the three occurring frequency components are fitted with Lorentzian lineshape and the parameters of the intensity and linewidth are extracted.

The intensity of the individual spectral components is plotted in figure 6.10 (a) in dependence of the detuning Δ . As discussed for a slightly lower injection strength $\kappa_{\text{eff}} = 0.054$ in figure 6.4, the master laser emission is enhanced for positive detunings. The non-locked micropillar emission is reduced at the edge of the locking range which we attribute to partial injection locking of the high- β microlaser.

The FWM has a low, but constant intensity at large detunings $-6 \text{ GHz} < \Delta$ and $\Delta < 6 \text{ GHz}$. In the region of partial injection locking, indicated by the yellow area, the intensity I_{FWM} increases by a factor of 4. Although the FWM results from a mixture of master and

slave laser emission, the FWM intensity I_{FWM} increases while the total intensity I_{total} decreases. Close to the locking range, the gain is stronger influenced by the injected master laser and consequently the refractive index change is larger which leads to an increased intensity of the FWM [Liu94].

Obviously, the intensity decreases linearly close to the locking range. A linear fit of the non-locked slave intensity and the FWM intensity is performed in this region, see figure 6.10 (b). The non-locked intensity has a slope of $m_{n-1} = -4.6 \pm 0.7$, respectively $m_{n-1} = 5.1 \pm 0.4$, while the FWM changes its intensity with $m_{\text{FWM}} = 1.91 \pm 0.26$, respectively $m_{\text{FWM}} = -1.85 \pm 0.16$ as function of κ_{eff}^2 . The values are similar for negative and positive detunings within the experimental uncertainties. The quotient of non-locked to FWM emission is $m_{n-1}/m_{\text{FWM}} = -2.6 \pm 0.5$. The applied fit does not rely on a physical model and it will be interesting to develop a suitable theory in the future to describe the observed behavior. The intensity change of FWM in the region of partial injection locking can be hint for a different characteristic of FWM in high- β QD micropillar lasers compared to conventional low β semiconductor lasers.

The linewidth of the non-locked QD micropillar emission and the FWM is depicted in 6.10 (c). With lower detuning Δ , both emission contributions, the non-locked slave laser and the FWM emission, start to broaden. This indicates that with less available gain for the non-locked slave emission, the emission has a less coherent character and consequently the linewidth is enlarged. The linewidth of the FWM can be estimated by [Hui92]

$$\nu_{\text{FWM}} = 4 \cdot \nu_{\text{sl}} + \nu_{\text{inj}} \quad (6.3)$$

and is also plotted in figure 6.10 (c) as function of the detuning Δ . The linewidth of the master laser is resolution limited and is estimated to be $\nu_{\text{inj}} = 100$ kHz from the device specification (c.f. section 3.2). The calculated FWM linewidth is slightly larger than the measured ν_{FWM} , but the progression with the detuning is similar.

In a second measurement of the injected QD micropillar 5-1, the FWM is analyzed for fixed detuning of $\Delta = 2.8$ GHz and increasing injection strength κ_{eff} . The intensity of the FWM is known to increase quadratically with κ_{eff} for semiconductor lasers [Nie89] due to a modulation of the refractive index by the master laser. The FWM emission intensity is plotted in dependence of κ_{eff}^2 in figure 6.3 (a). $I_{\text{FWM}}/I_{\text{inj}}$ is evaluated for a comparison with the resulting master intensity. I_{inj} includes the emission enhancement of the master laser's signal by the locked QD micropillar emission. The quotient is constant with a conversion efficiency of 9.2 ± 0.4 %, being on the order of magnitude as reported previously for semiconductor lasers [Nak86, Nak85b]. Thus, the present results indicate that the dependence of FWM in QD micropillar lasers on the injection strength κ_{eff} is

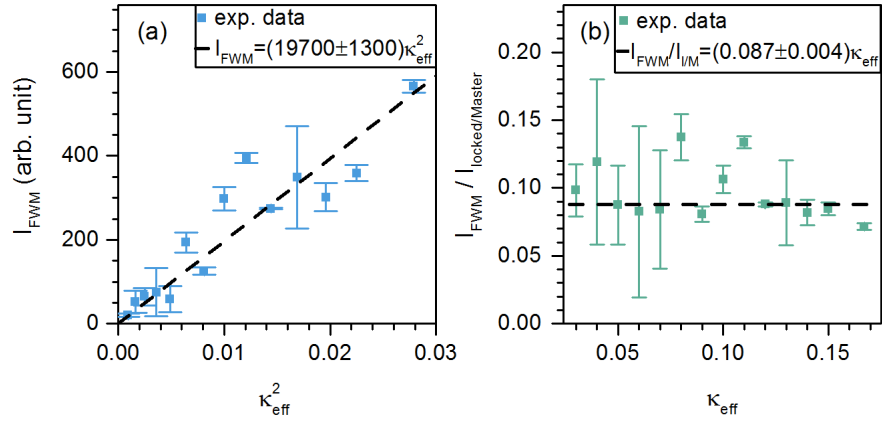


Figure 6.11: Intensity of the FWM emission of QD micropillar 5-1 at fixed detuning $\Delta = 2.8$ GHz. (a) The intensity of FWM I_{FWM} in dependence of κ_{eff}^2 is fitted with a linear behavior with $I_{\text{FWM}} = (19700 \pm 1300) \kappa_{\text{eff}}^2$. (b) The quotient with the (enhanced) master intensity $I_{\text{FWM}}/I_{\text{inj}}$ has a constant value of approximately 0.087.

similar to conventional low β semiconductor lasers.

6.2 Optical Injection in Bimodal QD Micropillar Lasers

Stochastic mode switching in bimodal QD micropillar lasers features rich intrinsic dynamics. The influence of optical injection on the bimodal behavior and in particular the polarization switching dynamics of QD micropillar lasers is studied in this section. The studied bimodal QD micropillar laser 5-2 from sample B (c.f. section 3.1 and A.2) has a linearly polarized lasing mode, called strong mode and a perpendicular polarized non-lasing mode, called weak mode.

Experiments with linearly polarized optical injection experiments are performed parallel and orthogonal to the lasing strong mode and the response of both modes is analyzed. Optical injection influences the intensity of both modes and can cause stochastic switching 4.2. The results of this section are published in [Sch19]

Emission Characteristics of the Bimodal QD Micropillar Laser

The input-output characteristics of the electrically driven bimodal QD micropillar laser 5-2 with 5 μm diameter at 30 K are presented in figure 6.12. The optical spectrum in panel (a) exhibits emission of the strong mode and weak mode with an excitation current $1.6 I_{\text{thr}}$ ($I_{\text{thr}} = 12 \mu\text{A}$) at 898.55 nm and 898.5 nm which corresponds to an energy splitting of the modes is $47 \mu\text{eV} \hat{=} 11 \text{GHz}$. The laser threshold is estimated conventionally as the matching point of a linear regression from the intensity below threshold and the fast increasing part. The measured emission intensity is scaled to an intracavity photon number of $\langle n \rangle = 1$ at the threshold. The intensity of the weak mode of QD micropillar 5-2 is higher than the weak mode intensity of QD micropillar 5-1 which was investigated as a single mode laser in the previous section 6.1 (c.f. figure 6.1). For example, the intracavity photon number of the weak mode from microlaser 5-2 at $1.6 I_{\text{thr}}$ is $\langle n \rangle = 170$ and at $2 I_{\text{thr}}$ $\langle n \rangle = 32$ while it is for QD micropillar laser 5-1 at $1.6 I_{\text{thr}}$ is $\langle n \rangle = 12$ and at $2 I_{\text{thr}}$ $\langle n \rangle = 7$. The weak mode emission of QD micropillar 5-2 is significant and the microlaser is considered as bimodal. The Q factor the QD micropillar is estimated via the linewidth at transparency (12 μA) to be $Q_{\text{strong}} = 9,100$ and $Q_{\text{weak}} = 10,700$. Interestingly, the non-lasing weak mode has a slightly higher intensity than the strong mode up to a current of $I/I_{\text{thr}} \approx 1.3$ and lower linewidth than the strong mode due to the larger Q factor. However, intermode kinetics describe processes with photon transfer between the modes and can favor the mode with lower Q [Ley17] which leads here to an intensity take-over of the strong mode at $1.4 I/I_{\text{thr}}$. The α -factor is estimated via numerical modeling of the QD micropillar laser in agreement with the experimental above-threshold linewidth to amount $\alpha = 1$ [Sch19].

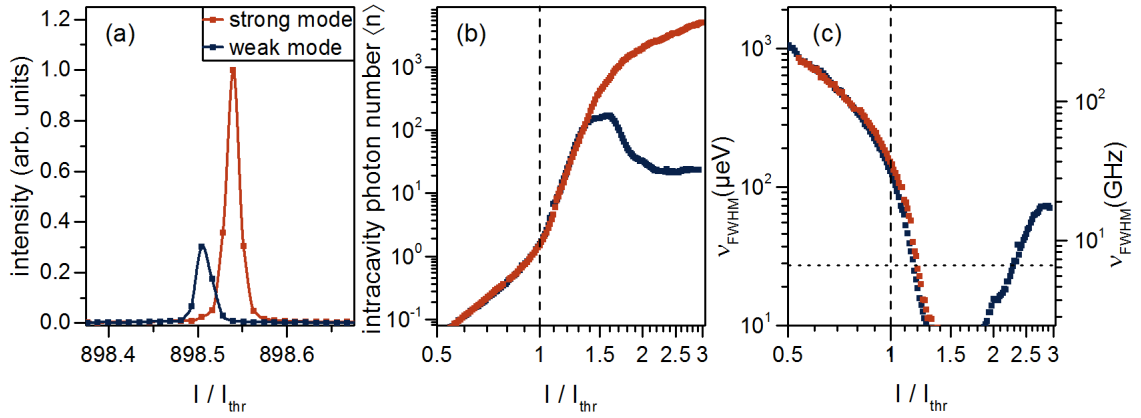


Figure 6.12: (a) Optical spectrum of the bimodal mode QD micropillar 5-2 at $I/I_{thr}=1.6$ and 30 K shows emission of the strong mode at 898.55 nm and of the weak mode at 898.5 nm. (b) Emission intensity and (c) linewidth characteristics are depicted in dependence of the current in units of the threshold current (dashed line) $I_{thr} = 12 \mu\text{A}$. The strong mode has a laser-like s-shape behavior while the weak mode's intensity shows a maximum at $1.6 I/I_{thr}$ and decreases for higher injection current. The linewidth decreases around the threshold (dashed line) below the resolution limit of the monochromator (dotted line). The weak mode broadens above $I/I_{thr}=2$.

Optical Injection into the Lasing Strong Mode

In the following subsections, first optical injection into the strong mode and afterwards into the weak mode and their influence on both modes is studied. An injection current $I/I_{thr} = 2$ is chosen for all optical injection experiments in this section. The injection strength κ is stated for the output power of the slave laser $P_S = P_{S,strong} + P_{S,weak}$ and the master laser P_{inj} :

$$\kappa = \sqrt{\frac{P_{inj}}{P_S}} = \sqrt{\frac{P_{inj}}{(P_{S,strong} + P_{S,weak})}} = \sqrt{\frac{P_{inj}}{(1.38 \mu\text{W} + 0.07 \mu\text{W})}}. \quad (6.4)$$

The emission powers P_{inj} , $P_{S,strong}$ and $P_{S,weak}$ are measured with a power meter. Due to the low power of the microlaser's weak mode, κ is lower for injection into the weak mode compared to injection into the strong mode for a similar intensity ratio of the master laser to the injected mode. Reflections of the master laser on the micropillar surface and non-ideal incoupling lead to an overestimation of κ . Comparing the width of the experimental and theoretical locking cones, the effective conversion factor is determined to be $\kappa_{eff} = \kappa/(10.8 \pm 1.8)$ [Sch19].

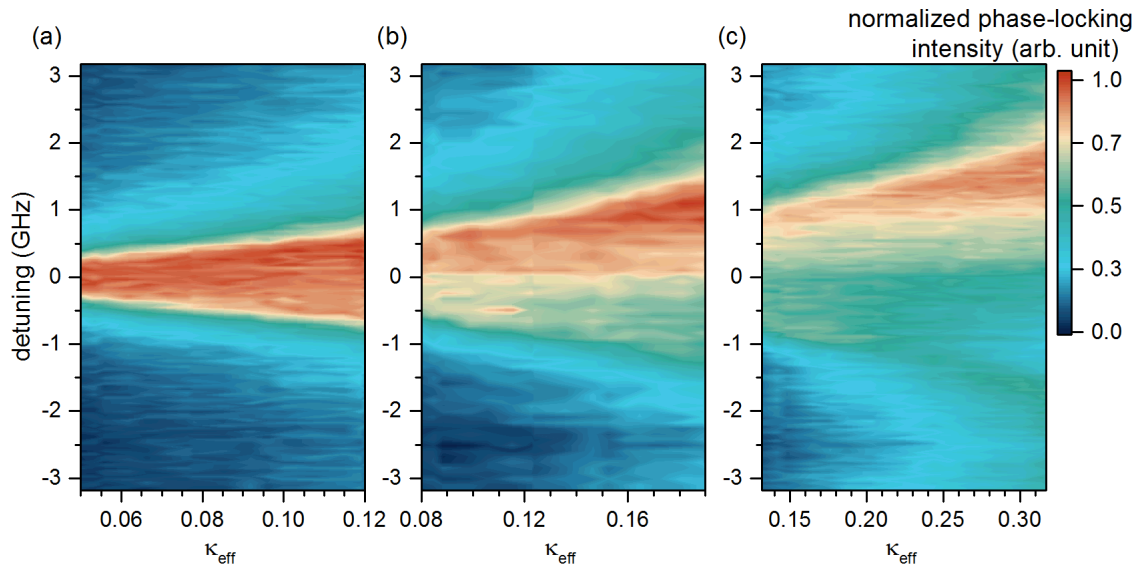


Figure 6.13: Phase-locking map of QD micropillar laser 5-2 at $I/I_{\text{thr}} = 2$ with optical injection in the strong mode. Three measurements with an injection strength (a) $0.05 < \kappa_{\text{eff}} < 0.12$, (b) $0.08 < \kappa_{\text{eff}} < 0.19$ and (c) $0.13 < \kappa_{\text{eff}} < 0.32$ show an increasing range of phase-locking with κ_{eff} for positive detunings and reduced phase-locking for negative detunings.

Phase-Locking of the Strong Mode

The locking cone is measured equivalent as for QD micropillar laser 5-1 in the previous section (c.f. figure 6.2). κ_{eff} is adjusted with a variable filter wheel with a continuous optical density change from 0 to 1. This limits the accessible region of the injection strength κ_{eff} . In addition to the filter wheel, neutral density filters (NDF) were introduced. In figure 6.13 results with three different NDF configurations are obtained. Each panel is scaled to the maximum interference amplitude which is a measure for the phase-locking strength.

The locking cone has a width of 0.7 GHz at low injection strength $\kappa_{\text{eff}} = 0.05$ and increases up to 3.7 GHz for large injection strength $\kappa_{\text{eff}} = 0.32$. The cone is symmetric for low injection strength between $0.05 < \kappa_{\text{eff}} < 0.12$ as shown in figure 6.13 (a). In panels (b) and (c), showing data recorded for a larger injection strength, the width of the phase-locking is symmetric, however, the phase-locking intensity is substantial lower for negative detunings. The total emission intensity is reduced for negative detunings (see figure 6.14) which we attribute to destructive interference between outgoing emission from the microcavity and incident master emission which is reflected on the top facet of the micropillar. Here, the lower intensity of the interfering emission reduces the interference amplitude.

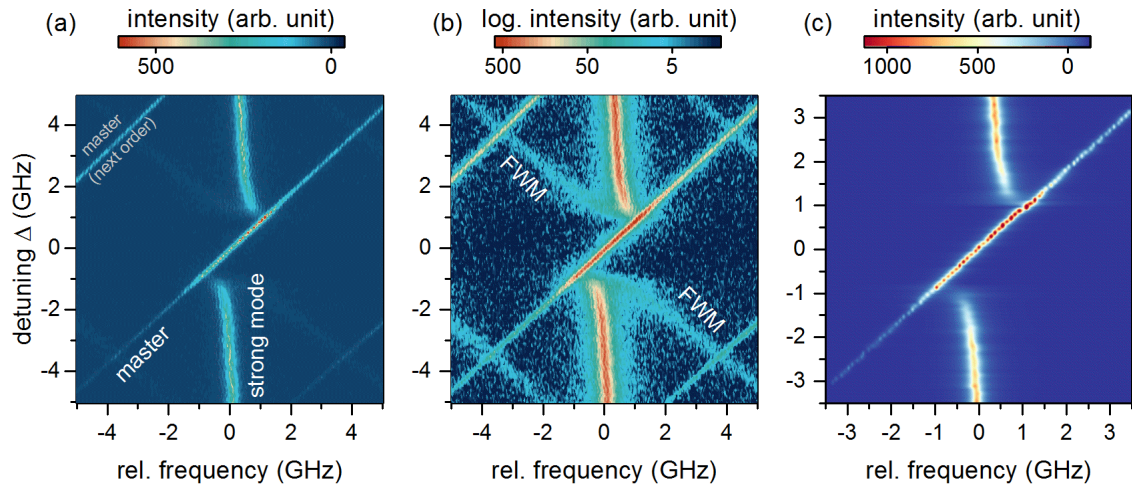


Figure 6.14: Heat map of the strong mode emission spectra of QD micropillar 5-2 under optical injection into the strong mode with $\kappa_{\text{eff}} = 0.12$ in dependence of the detuning Δ . Experimental data are depicted in (a) linear color coding and (b) logarithmic color coding. Panel (c) shows a fit to the experimental data. The master laser is tuned over the microlasers resonance. The QD micropillar is pulled towards the master laser and strongly amplifies the master inside the locking range. Logarithmic scaling reveals FWM outside the locking range.

Optical Spectrum of the Injected Strong Mode

High resolution spectra of QD micropillar 5-2 under optical injection in the strong mode with $\kappa_{\text{eff}} = 0.12$ were measured by an FPI in dependence of the detuning Δ . The resulting spectra are plotted as heatmaps in three different presentations in figure 6.14. Panel (a) shows the experimental data in linear and panel (b) in logarithmic intensity scaling. The spectra are fitted with Lorentzian lineshape for the master and the strong mode peaks. The spectra in panel (c) show the fit to the experimental data. This procedure enables the removal of peaks from the adjacent free spectral range of the FPI which are indicated in grey. This discrimination of the free spectral range is in particular important for the measurement of the weak mode.

For the following experiments, the relative frequency is set to 0 GHz, i.e. at the frequency of the free-running microlaser. The tuned master laser appears as the diagonal line in figure 6.14. With optical injection, polarized to the strong mode of the micropillar, the microlaser locks to the master laser in a range of about 2 GHz. Outside the locking range, the QD micropillar laser is pulled towards the master laser in frequency as described by Adler's equation in section 2.3 (c.f. figure 2.11). The logarithmic scaling of the intensity in panel (b) enables the observation of FWM signals. A continuous reduction of the slave laser intensity, meaning partial injection locking, is observed close to the locking range for

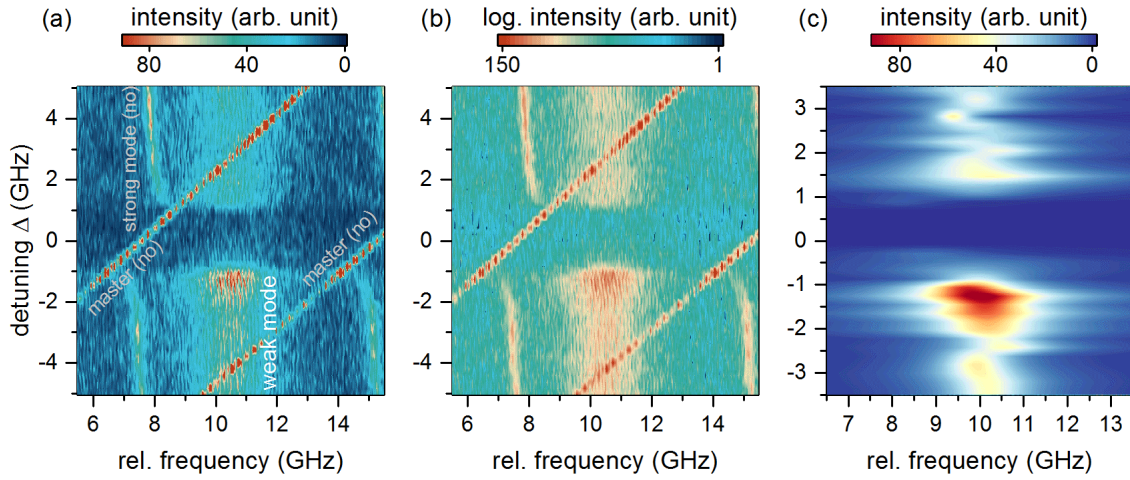


Figure 6.15: 2D map of the non-injected weak mode spectra versus the detuning Δ . Experimental data are depicted in (a) linear and (b) logarithmic color coding. (c) Shows a fit to the experimental data. The weak mode emits at a relative frequency of 10.5 GHz. Emission of the much brighter master laser and strong mode are visible in the spectra as diagonal line and at 7.5 GHz, respectively, and indicated by grey labels. In (c) solely the weak mode is plotted. The weak mode is suppressed inside the locking range $-1 \text{ GHz} < \Delta < 1 \text{ GHz}$. At the edge of the locking range at negative detunings, the weak mode is enhanced.

detunings $-2 \text{ GHz} < \Delta < -1 \text{ GHz}$ and $1 \text{ GHz} < \Delta < 2 \text{ GHz}$. Noteworthy, the spectra of the injected strong mode of the bimodal QD micropillar laser 5-2 reveal a similar behavior to the single mode case of QD micropillar 5-1 (c.f. figure 6.3).

Response of the Non-Lasing Weak Mode to Injection into the Lasing Strong Mode

To investigate the non-injected weak mode, the $\lambda/2$ -wave plate in the detection path is turned by 45° . One has to note, the intensity ratio of weak and strong mode emission ($\approx 1 : 60$) is on the order of the extinction ratio of the polarizing beam splitter ($\approx 1 : 300$). As a result, contributions of the strong mode and the master laser are visible in the weak mode spectra. The free-running weak mode has a large linewidth of $\nu_{\text{FWHM}} = 2.1 \text{ GHz}$ which additionally reduces the peak height for a given intensity compared to the master laser.

Figure 6.15 shows the weak mode spectra in (a) linear and (b) logarithmic scaling. The experimental data is fitted with Lorentzian lineshape and the fit to the spectra of the weak mode is plotted in panel (c). The broad peak at 10.5 GHz shows emission of the weak mode. The diagonal line corresponds to the master laser and the peaks at -7.5 and 15.0 GHz correspond to emission of the strong mode in two adjacent free spectral ranges of the

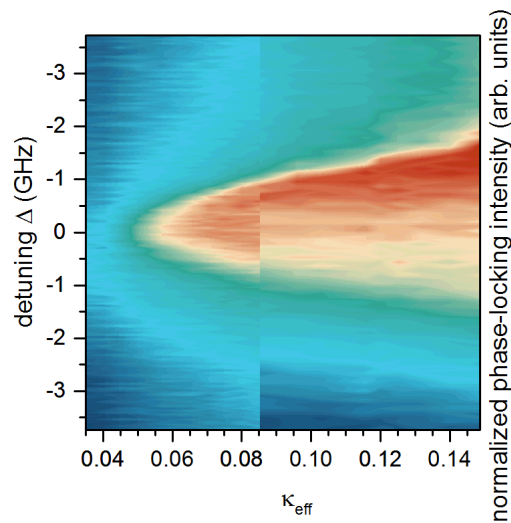


Figure 6.16: Weak mode phase-locking map of QD micropillar laser 5-2. Two measurements with low $0.035 < \kappa_{\text{eff}} < 0.085$ and large injection strength $0.07 < \kappa_{\text{eff}} < 0.15$ are combined. The weak mode is not locked below $\kappa_{\text{eff}} = 0.045$. The range of phase-locking increases with the injection strength κ_{eff} .

FPI. Due to the pillar's mode splitting of ≈ 11 GHz, the weak and strong mode do not match in frequency, although they are overlaid in the spectra.

To isolate the weak mode's contribution in the spectra, all peaks are fitted with Lorentzian lineshape. In figure 6.15 (c), the fit to the weak mode emission is plotted. The weak mode frequency seems to jitter which is an artifact from fitting a broad peak, overlaid by a second narrow peak as can be seen in panel (a). The weak mode intensity is constant for positive detunings and reduced at the edge of the locking range. Within the locking range of the strong mode between $-1 \text{ GHz} < \Delta < 1 \text{ GHz}$, the non-injected weak mode emission is suppressed. The reduction is caused by gain coupling of the weak and the strong mode. The master laser couples to the gain inside the locking range and reduces the available gain of the weak mode, which consequently decreases in intensity.

At the negative edge of the locking cone, the weak mode is enhanced. The master laser and the strong mode emission interfere destructively in this region (c.f. figure 6.13) which reduces the gain coupling of the strong mode. As a result, the available gain for the weak mode is enlarged and higher emission intensity is reached.

Optical Injection into the Non-lasing Weak Mode

For the following experiments, the non-lasing weak mode is injected and the response of both modes is investigated. Therefore, the master laser polarization is aligned to the

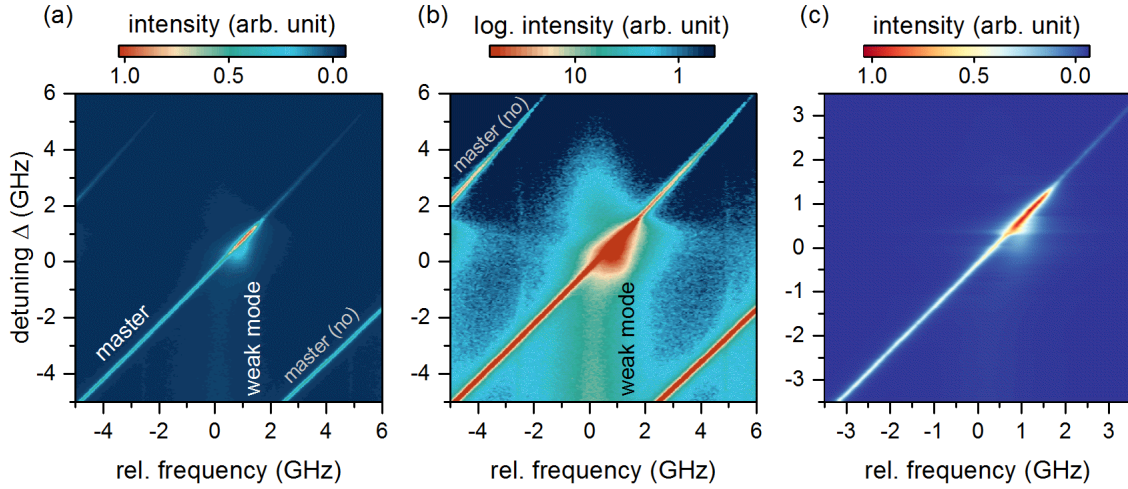


Figure 6.17: 2D map of the optical spectra of the weak mode of QD micropillar 5-2 under optical injection for $\kappa = 0.069$. Experimental data are depicted in (a) linear and (b) logarithmic color coding. Panel (c) shows a fit to the experimental data. The broad, low intensity weak mode emission is observed at a relative frequency of 0 GHz and is visible only in logarithmic scaling. The master laser is strongly enhanced between 0 and 1.5 GHz detuning.

polarization of the weak mode and its frequency is shifted by 11 GHz to match the weak mode's frequency.

Phase-Locking of the Weak Mode

The phase-locking of the weak mode of QD micropillar laser 5-2 to the master laser was measured at an excitation current of $I/I_{\text{thr}} = 2$. The obtained phase-locking cone is depicted in figure 6.16. The range of phase-locking increases with κ_{eff} as expected. Compared to the locking cone of the strong mode (c.f. 6.13), the phase-locking contrast from small to large injection strength κ_{eff} is larger for the weak mode. This means that injection locking of the weak mode needs a higher injection power than for the strong mode because the free-running weak mode is not in the lasing regime. In contrast to the strong mode, the phase-locking intensity shows only a slight asymmetry inside the locking range with respect to the sign of detuning. The locking cone indicates that optical injection in a non-lasing mode can bring this mode to lasing as shown for VCSELs [Pan93].

Optical Spectrum of the Injected Weak Mode

To investigate frequency locking of the weak mode, optical spectra of QD micropillar 5-2 with $\kappa = 0.069$ were recorded for different detunings Δ . The weak mode spectra under optical

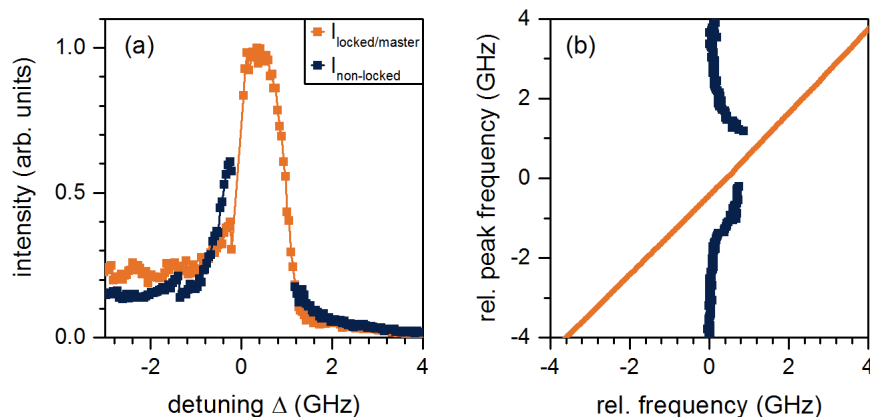


Figure 6.18: (a) Emission intensity and (b) relative frequency of the weak mode under optical injection in dependence of the detuning Δ . The non-locked weak mode emission is plotted in dark blue and the master in orange. (a) The master laser is enhanced up to a factor of four in the positive detuning range of 0 to 1.5 GHz. The non-locked weak mode emission is enhanced between $-1 \text{ GHz} < \Delta < 0 \text{ GHz}$. (b) The relative frequency of the non-locked emission is shifted to larger frequencies.

injection are shown as a 2D map in figure 6.17 in dependence of the detuning Δ . The relative frequency is set to zero at the center of the weak mode. With a linear scaling of the intensity in panel (a), the weak mode is almost not visible. With a logarithmic scaling in panel (b), a broad peak with low intensity appears at 0 GHz. The weak mode is injection locked and the master laser enhanced between $0 \text{ GHz} < \Delta < 1.5 \text{ GHz}$. Additionally, the non-locked weak mode emission is shifted to larger frequencies and has a higher intensity. The peaks of the weak mode and the master laser are fitted with Lorentzian lineshape for a detailed analysis. The extracted intensity and frequency are depicted in figure 6.18 versus the detuning Δ . The integrated intensity of the master laser and the injected weak mode are comparable for negative detunings Δ , although the mode was almost not visible in the spectra. Noteworthy, the peak intensity of the weak mode in the spectra is low because of the large linewidth $\nu_{\text{FWHM}} = 2.1 \text{ GHz}$. At the lower edge of the locking range around $\Delta = -1 \text{ GHz}$, increases the intensity of the non-locked weak mode emission and the master laser. The master laser is enhanced up to a factor of four and concurrently enlarges the available gain for the non-locked weak mode emission.

The non-locked weak mode is shifted to larger frequencies for $-1.5 \text{ GHz} < \Delta < 2 \text{ GHz}$ as can be seen in figure 6.18 (b) with a maximum shift of 0.7 GHz. The microlaser's frequency is expected to be pulled towards the master frequency, described by the Adler equation (c.f. figure 2.11). Here, for negative detuning, the microlaser frequency is pushed away

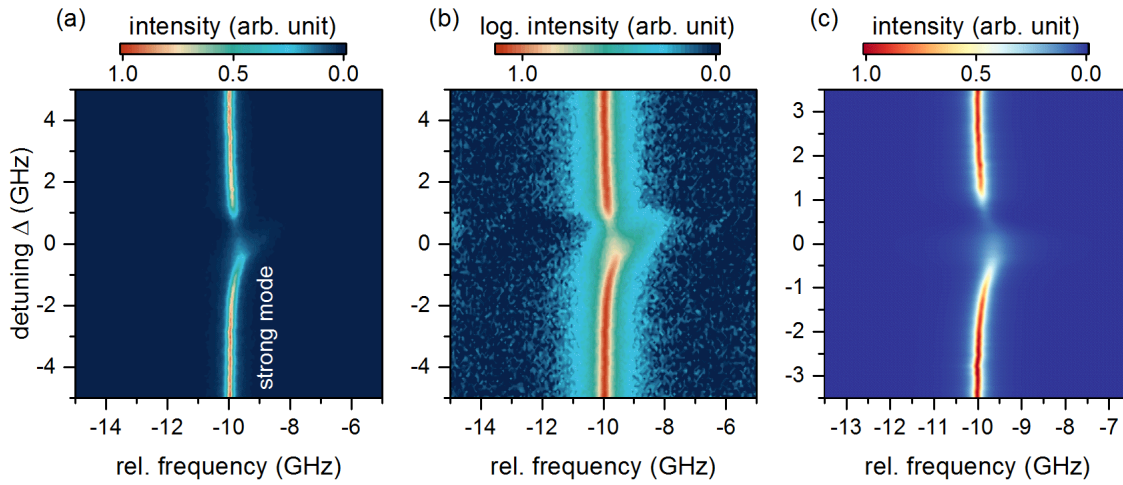


Figure 6.19: Optical spectra of the non-injected strong mode of QD micropillar laser 5-2 with $\kappa = 0.069$ is a 2D presentation versus the detuning Δ . Experimental data are plotted in (a) linear and (b) logarithmic color coding and (c) shows a fit to the experimental data. The strong mode emits at a relative frequency of -10 GHz. Between a detuning of $-1 < \Delta < 1$ GHz, the intensity of the strong mode is reduced and a blue-shift of the emission frequency occurs. Logarithmic intensity scaling reveals remaining strong mode emission for all detunings.

from the master frequency. This behavior was also observed for VCSELs with several higher order transverse modes [Li96] or if the non-lasing polarization mode is injected [Alt06] as in the present case.

Optical Spectrum of the Non-injected Strong Mode

The non-lasing weak mode is pushed to lasing by optical injection. The response of the lasing strong mode to injection in the weak mode is examined. The polarization optics are turned by 45° in the detection path to measure emission of the non-injected strong mode. Heat maps of the non-injected strong mode emission versus the detuning are depicted in figure 6.19. In the locking range of the weak mode $0 \text{ GHz} < \Delta < 1.5 \text{ GHz}$, the strong mode intensity is reduced. Here, the master laser couples to the gain and is enhanced by stimulated emission. Consequently, less gain is available for the strong mode due to gain competition between the two modes. A coupling of the intensity and frequency, described by the α -factor [Hen82], shifts the strong mode emission to larger energies when the intensity is decreased.

Influence of Optical Injection in Bimodal QD Micropillar Lasers on the Temporal Switching

An interesting characteristic of bimodal QD micropillar lasers is the appearance of stochastic mode switching between the strong and the weak mode [Ley13]. This behavior was addressed in section 4.2 and 5.2 for free-running QD micropillar lasers. The occurrence and stability of stochastic switching depends sensitively on many device parameters like the mode splitting and the gain coupling. The switching effects are also very sensitive on external parameters like the pump power [Vir13] and an influence of optical injection on the stability of the QD micropillar modes is expected.

Cross-Correlation Measurements under Optical Injection into the Non-lasing Weak Mode

The temporal correlation of two optical signals, weak and strong mode emission, is measured by cross-correlation measurements in which antibunching indicates stochastic polarization switching. For the cross-correlations measurements, the QD micropillar is driven at $2 I/I_{\text{thr}}$ and the master laser is injected to the polarization angle of the weak mode with an injection strength $\kappa_{\text{eff}} = 0.044$.

Figure 6.20 (a) depicts two exemplary cross-correlation measurements. Without injection (dark blue line), $g_{\text{SW}}^{(2)}(0) = 0.98$ proves negligible correlation of the weak and the strong mode of QD micropillar laser 5-2. The second example (red line) shows the cross-correlation of QD micropillar 5-2 under optical injection with $\kappa_{\text{eff}} = 0.044$ and $\Delta = -0.4$ GHz. $g_{\text{SW}}^{(2)}(\tau)$ reveals pronounced antibunching with $g_{\text{SW}}^{(2)}(0) = 0.46$ at zero time delay. The weak and the strong mode emission are strongly anticorrelated which indicates temporal mode switching.

The cross-correlation $g_{\text{SW}}^{(2)}(\tau)$ is fitted with function 4.2 to extract $g_{\text{SW}}^{(2)}(0)$ and τ_{cor} which are presented in figure 6.20 (b) and (c) in dependence of the detuning Δ . The dashed reference line is $g_{\text{SW}}^{(2)}(0) = 0.98$ as determined for the free-running microlaser. The injection strength is fixed to $\kappa_{\text{eff}} = 0.044$ and the detuning Δ is varied between -2 GHz and 3 GHz. The micropillar modes are uncorrelated up to a detuning $\Delta = -1$ GHz and above $\Delta = 2$ GHz. However, around a detuning $\Delta = -1$ GHz decreases $g_{\text{SW}}^{(2)}(0)$ to 0.4 and increases above $\Delta = 0$ GHz. A look to the locking map of the weak mode in figure 6.16 reveals that the weak mode is not (fully) locked to the master for this low injection strength $\kappa_{\text{eff}} = 0.044$, but induces correlations of the modes.

The cross-correlation measurements prove that optical injection into the non-lasing mode can induce stochastic mode switching in bimodal microlasers. The weak mode is enhanced by the external laser. Thereby, intensity fluctuations are amplified and the weak mode

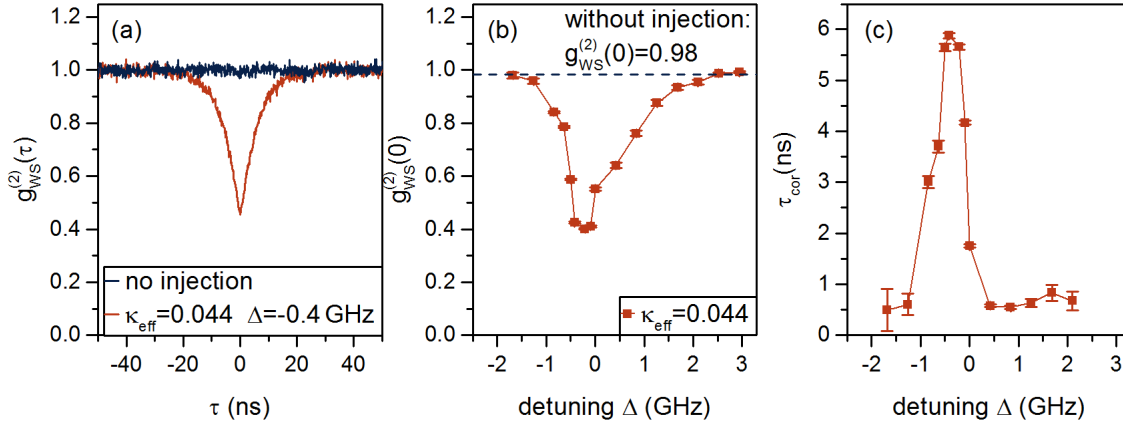


Figure 6.20: Cross-correlation measurements of QD micropillar 5-2 under optical injection in the weak mode with $\kappa_{\text{eff}} = 0.044$. (a) $g_{\text{SW}}^{(2)}(\tau)$ without injection shows minor correlations with $g_{\text{SW}}^{(2)}(0) = 0.98$. With injection, the emission of weak and strong mode is anticorrelated and $g_{\text{SW}}^{(2)}(\tau)$ decreases around $\tau = 0$. (b) $g_{\text{SW}}^{(2)}(0)$ exhibits a sharp onset of switching events at $\Delta = -1$ GHz identified by strong anticorrelation of $g_{\text{SW}}^{(2)}(0) \approx 0.4$ and a transition to $g_{\text{SW}}^{(2)}(0) = 1$ between $0 < \Delta < 1.5$ GHz. The dashed line corresponds to $g_{\text{SW}}^{(2)}(0) \approx 0.98$ without injection. (c) The correlation time τ_{cor} is around 0.6 ns below $\Delta = -1$ GHz and above $\Delta = 0.5$ GHz and increases up to 6 ns for $\Delta = -0.5$ GHz.

is able reach the lasing regime, accompanied with a suppression of the strong mode (c.f. figure 6.15). $g_{\text{SW}}^{(2)}(0)$ does not decrease to zero for two reasons. Firstly, the non-lasing mode has a low, but non-negligible intensity. Secondly, the master laser and its reflection at the sample surface contribute to the detected signal. These temporally uncorrelated signals lead to non-ideal antibunching.

The correlation time of the antibunching τ_{cor} increases in a detuning range of $-1 \text{ GHz} < \Delta < 0.5 \text{ GHz}$ up to a value of 6 ns. The weak mode switches to the lasing regime for an average time of 6 ns. Interestingly, for positive detunings Δ , $g_{\text{SW}}^{(2)}(0)$ is smaller than 1, but the correlation time τ_{cor} is very low around 0.6 ns. Here, either very short switching events occur, or the optical injection causes strong anticorrelated fluctuations, but no complete mode switching events. This explanation is supported by simulations from David Schicke, described in his master thesis [Sch18a] and published in [Sch19].

$g_{\text{SW}}^{(2)}(0)$ is presented in figure 6.21 in dependence of the injection strength κ_{eff} for zero detuning $\Delta = 0$ GHz. A minimal injection strength $\kappa_{\text{eff}} = 0.032$ is required to stimulate the micropillar to stochastic switching, see panel (a). Between $\kappa_{\text{eff}} = 0.4$ and 0.07 the minimum of $g_{\text{SW}}^{(2)}(0) = 0.5$ is reached. Above $\kappa_{\text{eff}} = 0.07$, $g_{\text{SW}}^{(2)}(0) = 0.5$ increases to 1 and switching is suppressed. The strong injection stabilizes the weak mode which is constantly

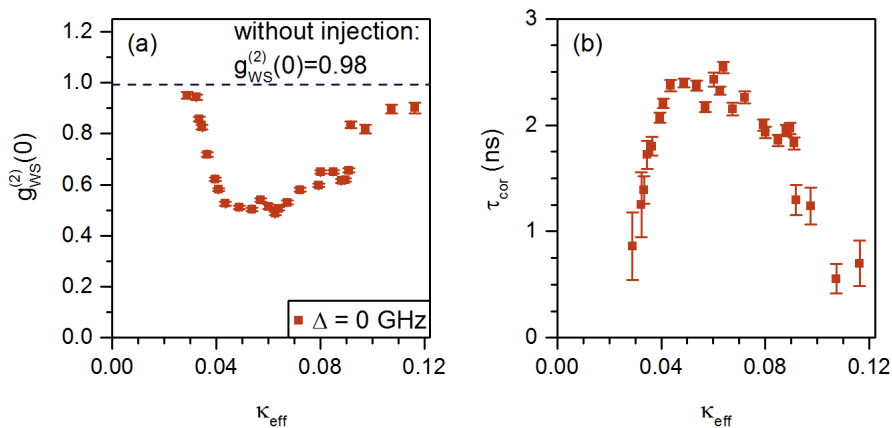


Figure 6.21: Cross-correlation measurement of QD micropillar 5-2 under optical injection in the weak mode at $\Delta = 0$ in dependence of the injection strength κ_{eff} . (a) $g_{\text{SW}}^{(2)}(0)$ reveals stochastic switching for $\kappa_{\text{eff}} > 0.03$ which is suppressed for high injection strength $\kappa_{\text{eff}} > 0.1$ due to stable lasing of the weak mode. (d) The correlation time increases for $0.3 < \kappa_{\text{eff}} < 0.1$ up to 2.5 ns.

lasing while the strong mode is suppressed. This is in good agreement with the measured locking cone for injection in the weak mode shown in figure 6.16.

The correlation time τ_{cor} in figure 6.21 (b) increases in the range of anticorrelations with a decreasing $g_{\text{SW}}^{(2)}(0)$. Lasing in the weak mode is stabilized for an injection strength $\kappa_{\text{eff}} > 0.1$. Interestingly, the onset of switching happens in a small range of $0.032 < \kappa_{\text{eff}} < 0.043$ compared to the stabilization of lasing in the weak mode between $0.067 < \kappa_{\text{eff}} < 0.11$. The emission intensity and intensity fluctuations amplitude of weak and strong mode, respectively, the lasing and non-lasing case, differ. This leads to a different sensitivity to perturbations of the weak and the strong mode [Sch18a].

Polarization mode switching was also observed in bimodal VCSELs [Ole11, Vir13] without injection. A comparable mode configuration exists in ring-lasers with the forth and backward propagation direction where switching between corresponding modes was observed [MT78]. Mode switching was observed in VCSELs under optical injection in references [Gat06, Yua07b, Li08]. However, the mode switching described in these publications is temporally stable and does not have a stochastic nature. In references [Sal15] and [Yua07a] pulsed orthogonal injection triggers a switch to the orthogonal (cw) mode which switches back shortly after the pulse. In contrast, the switching effects induced in high- β QD micropillar lasers in the presented experiments describe stochastic polarization switching. Optical injection into the non-lasing weak mode of a QD micropillar laser exhibited that the incidence and dwell time of stochastic polarization switching can be tailored by the

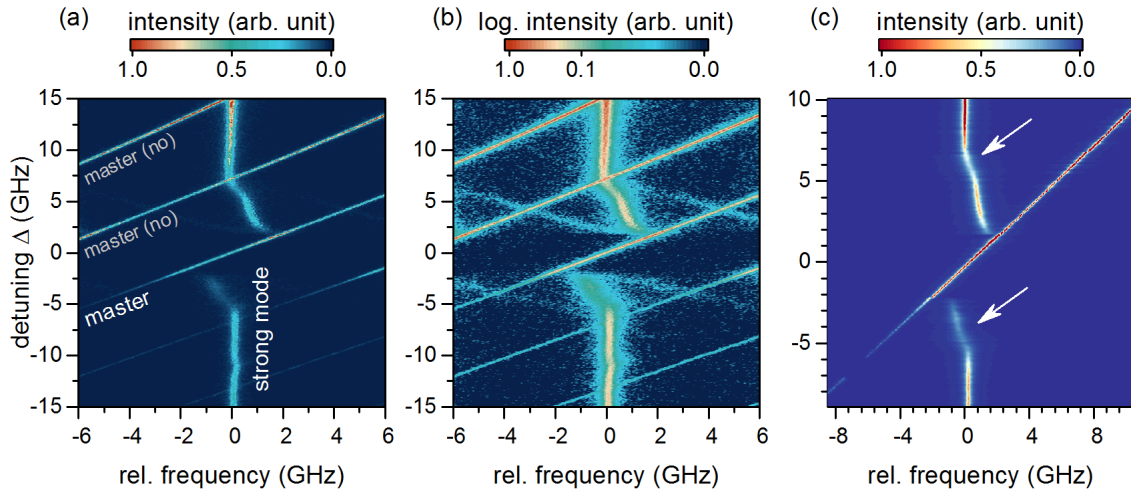


Figure 6.22: Heat map of the optical spectra of QD micropillar 5-2 under injection in the strong mode with $\kappa_{\text{eff}} = 0.27$ in dependence of the detuning Δ . Experimental data are presented in (a) linear and (b) logarithmic color coding. Panel (c) shows a fit to the experimental data. With the strong injection, a large locking range is achieved and the signals of several free spectral ranges of the FPI are shown to depict the full range of effects. Outside the locking range, the strong mode intensity decreases at -5 GHz and +7 GHz (indicated by white arrows).

injection strength and the detuning.

Indication of Mode Switching in the Optical Spectrum under Optical Injection into the Lasing Strong Mode

Optical injection outside the locking range can destabilize the injected mode [Ern10]. So far, this behavior has not been observed in the presented measurements. A destabilization of the strong mode was achieved by injection into the non-lasing weak mode, but not under injection in the strong mode itself. Hints of a destabilization of the optically injected strong mode are found for intense optical injection.

2D maps of the optical spectra of QD micropillar 5-2 at $I/I_{\text{thr}} = 2$ under high optical injection in the strong mode are presented in figure 6.22 with $\kappa_{\text{eff}} = 0.27$. The spectra reveal several features compared to the spectra with $\kappa_{\text{eff}} = 0.12$ in figure 6.14. Here, the locking range is much larger from $-2 < \Delta < 2$ GHz. The plotted detuning range includes the signals of the neighboring two free spectral ranges of the FPI as diagonal lines which are labeled in grey. They are removed in the plot of spectra calculated from fit parameter in panel (c). In logarithmic scaling contributions of FWM are visible.

Outside the locking range at -5 GHz, respectively 7 GHz, the strong mode is changed in

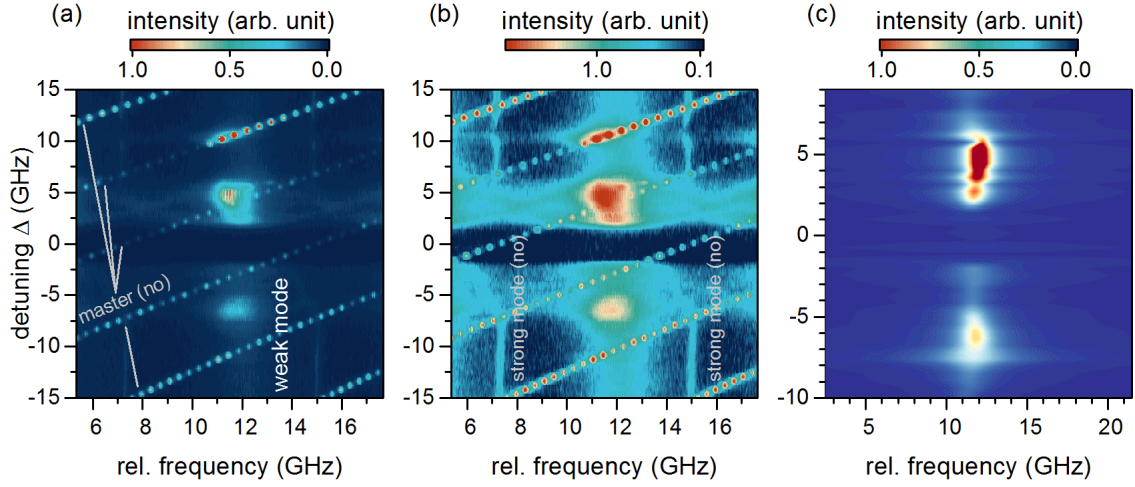


Figure 6.23: 2D maps of the optical spectra of the non-injected weak mode versus the detuning Δ . Experimental data are depicted in (a) linear and (b) logarithmic color coding. Panel (c) shows a fit to the experimental data. The master laser intensity is not completely suppressed and appears as diagonal lines. The weak mode emits at a relative frequency of 12 GHz as a broad peak with a low peak intensity. The weak mode emission is suppressed inside the locking range of the strong mode at $|\Delta| < 2$ GHz. Around $\Delta = -6$ GHz and $\Delta = 5$ GHz, the weak mode emission increases.

intensity and frequency. The intensity decreases in direction of the locking range and is pulled towards the master laser frequency. The master laser is not enhanced in this region due to the large detuning.

The associated 2D plots of the weak mode spectra are presented in figure 6.23. The diagonal lines of the master laser are due to a non-sufficient suppression by the polarizing beam splitter and can be disregarded. In panel (c) solely the spectra of the weak mode are plotted.

The weak mode has a low intensity and a large linewidth $\nu_{\text{FWHM}} \approx 2.5$ GHz. With logarithmic scaling in figure 6.23 (b) the peak of the weak mode is visible at a relative frequency of 12 GHz outside the locking range. Inside the locking region of the strong mode -2 GHz $< \Delta < 2$ GHz, the gain is pulled towards the master laser and the weak mode is suppressed. At both sides of the locking range, up to $\Delta = -8$ GHz and 6 GHz, the weak mode is enhanced up to a factor of 8.

For a further analysis, the spectra of strong and weak mode are fitted with Lorentzian lineshape. The extracted intensity and linewidth are plotted in figure 6.24 in dependence of the detuning Δ . The intensity of the strong mode and the weak mode is normalized to 1, respectively. Two regions with a width of 3.6 GHz are accentuated with light blue boxes

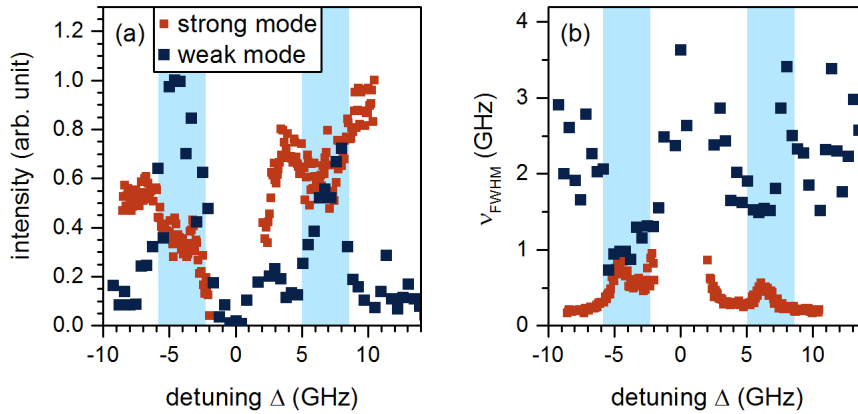


Figure 6.24: (a) Intensity of the non-locked strong mode (red) and the weak mode (blue) of QD micropillar 5-2 under optical injection in the strong mode with $\kappa_{\text{eff}} = 0.27$ in dependence of the detuning Δ . The light blue shaded area indicates the region where the weak mode increases and the strong mode decreases in intensity. (b) The linewidth of the weak mode decreases and the strong mode broadens in this area.

where the intensity of the weak mode increases. Here, simultaneously the strong mode drops in intensity (c.f. figure 6.22) and a change in the linewidth can be observed. The strong mode's linewidth is enlarged up to $\nu_{\text{strong}} = 1$ GHz while the weak mode narrows to $\nu_{\text{weak}} = 0.8$ GHz. The opposed behavior of the weak and the strong mode regarding the intensity and the linewidth is a hint for switching processes induced by injection into the strong mode. Stochastic switching is expected for optical injection into the strong mode of QD micropillar lasers [Sch18a].

An indirect proof of switching by enhanced anticorrelation via cross-correlation measurements was not accessible. The master laser could not be sufficiently suppressed by polarization optics and was masking the signal of the weak mode on the SPCM. In auto- and cross-correlation measurements consistently $g^{(2)}(\tau)=1$ was measured and reflects only the coherent character of the master laser.

Stochastic polarization switching under optical injection was achieved by VCSELs [DIC17, DIC18]. There, time series show sudden changes in the intensity where the lasing mode decreases in intensity and the non-lasing polarization mode becomes brighter. However, a complete switch from lasing to the orthogonal mode was not observed. The optical spectra of the QD micropillar laser give hints for polarization chaos, although the switching was not directly proven.

In summary, QD micropillar lasers under optical injection have been studied in this chapter. In the section 6.1, the microlaser was considered as single mode laser. The injected QD micropillar 5-1 revealed phase-locking and frequency locking as described by Adler's equation. Outside the locking range, the new effect of 'partial injection locking' was observed where the master laser is enhanced and the QD micropillar laser partially suppressed. The simultaneous emission on both frequencies was proven by measurements of the second-order autocorrelation. Partial injection locking is attributed to the large spontaneous emission in high- β microlasers.

The bimodal QD micropillar 5-2 was target of optical injection in section 6.2. Injection with the strong mode polarization locks this mode while the weak mode emission is suppressed. Although the weak mode is not in the lasing regime, parallel optical injection locks the weak mode. Moreover, optical injection into the weak mode can induce stochastic mode switching dependent on the injection strength and detuning which are observable preferentially in high- β microlasers.

7 Conclusion and Outlook

Nonlinear laser dynamics of semiconductor lasers is a highly interdisciplinary research topic with manifold applications [Wie05]. With the ongoing improvement of laser efficiency and miniaturization, the assessment of nonlinear dynamics close to the quantum regime has become possible using high- β microlasers with enhanced spontaneous emission [Alb11, Cas17]. Quantum dot micropillar lasers are attractive nanophotonics devices that can be electrically driven to emit sub- μW output powers [Böc08]. This makes them ideal candidates for the investigation of nonlinear dynamics. Moreover, their bimodal emission characteristics exhibit rich intrinsic dynamics [Ley13].

In this thesis, the photon statistics of QD micropillar lasers and exciton-polariton lasers have been investigated. Optical injection experiments of QD micropillar lasers addressed their dynamics under various polarization and coupling configurations.

The fundamental emission characteristics of bimodal QD micropillar lasers are presented in chapter 4. The typical s-shape input-output dependence of high- β microlasers is shown and HBT measurements prove the transition to lasing. Cross-correlation measurements indicate stochastic switching between the two modes of free-running QD micropillar lasers which is directly proven by a Streak camera [Red16].

Chapter 5 examines the photon statistics of QD micropillar lasers and exciton-polariton lasers. With a transition-edge sensor based photon number resolving detection system, the full-photon number distribution of the nanophotonic devices is measured [Sch18c]. The photon statistics distinguishes between a stable and a bistable QD micropillar laser configuration. In the stable case, the microlaser experiences a transition from thermal to coherent emission with increasing pump. In contrast, the bistable microlaser reveals a superposition of a thermal and a coherent state in the photon number distribution. The different cases were inaccessible with common experimental techniques and are exhibited by the photon number distribution. The coherent emission of another interesting type of semiconductor laser, namely an exciton-polariton laser, relies on stimulation scattering to the ground state. The photon statistics of this device exhibits a coherence buildup close to a photon laser transition.

Optical injection experiments have been performed for chapter 6. QD micropillar lasers show phase-locking and frequency locking to the master laser. Caused by the large spon-

taneous emission in high- β lasers, the QD micropillar reveals a novel regime of partial injection locking where the injected laser emits on two frequencies simultaneously. Weak optical injection into the non-lasing polarization mode can destabilize the QD micropillar laser, hence provoking a bistable behavior with pronounced mode switching. Furthermore, the non-lasing mode can be excited to laser emission with stronger parallel optical injection.

As an outlook to further studies in the field of high- β microlaser it is interesting to note that the intrinsic and generated dynamics in QD micropillar lasers are known to offer further intriguing physics like superradiance [Jah16] or dissipative coupling [Fan16] which become experimentally accessible by knowledge of the full photon number distribution. Theoretical simulations predict intermediate states for mode switching micropillars [Red16, Ley17] which can be measured by the correlated photon statistics of both modes. Exciton-polariton devices offer multiple effects that can be explored with the measurement of the photon number distribution, for instance in photonic condensates [Kla10], equilibrium condensates [Sun17] or exciton-polaritons with strong interactions [Ros18]. The measurement of the photon statistics can possibly be extended to polariton devices based on emerging 2D transition metal dichalcogenide materials as gain medium.

Beyond that, QD micropillar lasers can play an important role in energy efficient all-optical neuromorphic computing of coupled laser arrays [Bru15, Heu19]. The understanding and controlling of laser dynamics under feedback and optical injection is crucial for these applications. From the technology point of view, side-controlled QDs [Kag19] enable lasing of micropillars for very few emitters and allow for precise tailoring of the emission properties. This is a major technological advance that may lead to investigations of the laser dynamics with unprecedented control of the system and unforeseen applications of QD microlasers at the crossway between classical and quantum physics in the future.

Formula Symbol and Abbreviation List

formula symbol	name
α	linewidth enhancement factor
β	spontaneous emission factor
Δ	detuning between master and slave laser
Δ_{QD}	spectral detuning between cavity mode and maximum of QD emission band
κ	injection strength
κ_{eff}	effective injection strength
λ_{cav}	cavity mode wavelength
τ	time delay
τ_{bulk}	carrier lifetime in bulk material
τ_{coh}	coherence time
τ_{cor}	correlation time
τ_{phot}	photon lifetime inside the cavity
τ_{pol}	polarization decay time
τ_{pulse}	pulse length
τ_{pump}^{-1}	pump rate
τ_{res}	temporal resolution
τ_{rt}	cavity round-trip time
τ_{sp}	radiative carrier lifetime
τ_{SPCM}	temporal resolution of the SPCM
ν_{cav}	linewidth of the cavity mode (full width at half maximum)
ν_{FWHM}	peak linewidth (full width at half maximum)
Φ	photon density
ω_0	emission frequency (free running)
ω_{FWM}	frequency of four-wave mixing
ω_{inj}	injection frequency
ω_{RO}	relaxation oscillation frequency
ω_{M}	master laser frequency
$\omega_{\text{non-l}}$	non-locked slave laser frequency
ω_{sl}	slave laser frequency

formula symbol	name
a	oscillator coupling strength
d	thickness of the active layer
E	electric field
E_0	electric field amplitude
E_{inj}	electric field of the injection laser
E_{Phot}	photon energy
F_{P}	Purcell factor
$g^{(k)}(\tau)$	k's order autocorrelation
$g_{\text{SW}}^{(2)}(\tau)$	second-order cross-correlation between strong and weak mode
G	gain
I	intensity
I_{thr}	threshold current
n	population inversion
n_{eff}	effective refractive index
n_{ph}	photon number
n_{thr}	population inversion at threshold
$\langle n_{\text{ph}} \rangle$	average photon number
N	carrier density
P	polarization
$P(n_{\text{ph}})$	photon number distribution
P_{inj}	power of the master laser
P_{sl}	power of the slave laser
$P_{>\text{thr}}$	pump parameter above threshold
Q	quality factor
R	mirror reflection
t	time
T	transmission
V_{M}	mode volume

abbreviation	name
ADR	adiabatic demagnetization refrigerator
AOM	acusto optical modulator
AlAs	aluminium arsenide
cQED	cavity quantum electrodynamics
CW	continuous wave
DBR	distributed bragg reflector mirror
FPI	Fabry-Perot interferometer
FSR	free spectral range (of the FPI)
FWHM	full width half maximum
GaAs	gallium arsenide
HBT	Hanbury-Brown and Twiss configuration
InGaAs	indium gallium arsenide
OD	optical density
NDF	neutral density filter
PBS	polarizing beam splitter
PND	photon number distribution
QD	quantum dot
QW	quantum well
SPCM	single photon counting module
SQUID	superconducting quantum interference device
TES	transition-edge sensor
VCSEL	vertical cavity surface emitting laser

Bibliography

- [Adl46] R. Adler. “A study of locking phenomena in oscillators”. *Proceedings of the IRE*, **34** (1946), 351.
- [Agr13] G. P. Agrawal, N. K. Dutta. *Semiconductor lasers*. Springer Science & Business Media (2013).
- [Alb11] F. Albert, C. Hopfmann, S. Reitzenstein, C. Schneider, S. Höfling, L. Worschech, M. Kamp, W. Kinzel, A. Forchel, I. Kanter. “Observing chaos for quantum-dot microlasers with external feedback”. *Nature Communications*, **2** (2011), 366.
- [Alf63] Z. I. Alferov, R. Kazarinov. “Semiconductor laser with electric pumping”. *Inventor’s certificate*, **181737** (1963).
- [All97] K. T. Alligood, T. D. Sauer, J. A. Yorke, J. D. Crawford. “Chaos: An introduction to dynamical systems”. *Physics Today*, **50** (1997), 67.
- [Alt06] J. B. Altés, I. Gatara, K. Panajotov, H. Thienpont, M. Sciamanna. “Mapping of the dynamics induced by orthogonal optical injection in vertical-cavity surface-emitting lasers”. *IEEE journal of quantum electronics*, **42** (2006), 198.
- [And99] L. C. Andreani, G. Panzarini, J.-M. Gérard. “Strong-coupling regime for quantum boxes in pillar microcavities: Theory”. *Physical Review B*, **60** (1999), 13276.
- [Ara82] Y. Arakawa, H. Sakaki. “Multidimensional quantum well laser and temperature dependence of its threshold current”. *Applied Physics Letters*, **40** (1982), 939.
- [Are66] F. Arecchi, A. Berne, A. Sona, P. Burlamacchi. “1A4 - Photocount distributions and field statistics”. *IEEE Journal of Quantum Electronics*, **2** (1966), 341.
- [Are84] F. Arecchi, G. Lippi, G. Puccioni, J. Tredicce. “Deterministic chaos in laser with injected signal”. *Optics communications*, **51** (1984), 308.
- [Aßm09] M. Aßmann, F. Veit, M. Bayer, M. van der Poel, J. M. Hvam. “Higher-order photon bunching in a semiconductor microcavity”. *Science*, **325** (2009), 297.

- [Aßm11] M. Aßmann, J.-S. Tempel, F. Veit, M. Bayer, A. Rahimi-Iman, A. Löffler, S. Höfling, S. Reitzenstein, L. Worschech, A. Forchel. “From polariton condensates to highly photonic quantum degenerate states of bosonic matter”. *Proceedings of the National Academy of Sciences*, **108** (2011), 1804.
- [Bak15] L. Bakemeier, A. Alvermann, H. Fehske. “Route to chaos in optomechanics”. *Physical Review Letters*, **114** (2015), 013601.
- [Bal07] R. Balili, V. Hartwell, D. Snoke, L. Pfeiffer, K. West. “Bose-Einstein condensation of microcavity polaritons in a trap”. *Science*, **316** (2007), 1007.
- [Bar02] S. Barnett, P. M. Radmore. *Methods in theoretical quantum optics*, volume 15. Oxford University Press (2002).
- [Bay01] M. Bayer, T. L. Reinecke, F. Weidner, A. Larionov, A. McDonald, A. Forchel. “Inhibition and enhancement of the spontaneous emission of quantum dots in structured microresonators”. *Physical Review Letters*, **86** (2001), 3168.
- [Bim99] D. Bimberg, M. Grundmann, N. N. Ledentsov. *Quantum dot heterostructures*. John Wiley & Sons (1999).
- [Bjö91] G. Björk, Y. Yamamoto. “Analysis of semiconductor microcavity lasers using rate equations”. *IEEE Journal of Quantum Electronics*, **27** (1991), 2386.
- [Bjö94] G. Björk, A. Karlsson, Y. Yamamoto. “Definition of a laser threshold”. *Physical Review A*, **50** (1994), 1675.
- [Boi09] F. Boitier, A. Godard, E. Rosencher, C. Fabre. “Measuring photon bunching at ultrashort timescale by two-photon absorption in semiconductors”. *Nature Physics*, **5** (2009), 267.
- [Bru15] D. Brunner, I. Fischer. “Reconfigurable semiconductor laser networks based on diffractive coupling”. *Optics Letters*, **40** (2015), 3854.
- [Byr14] T. Byrnes, N. Y. Kim, Y. Yamamoto. “Exciton–polariton condensates”. *Nature Physics*, **10** (2014), 803.
- [Böc08] C. Böckler, S. Reitzenstein, C. Kistner, R. Debusmann, A. Löffler, T. Kida, S. Höfling, A. Forchel, L. Grenouillet, J. Claudon, J. M. Gérard. “Electrically driven high-Q quantum dot-micropillar cavities”. *Applied Physics Letters*, **92** (2008), 091107.

- [Cao10] D.-Z. Cao, G.-J. Ge, K. Wang. “Two-photon subwavelength lithography with thermal light”. *Applied Physics Letters*, **97** (2010), 051105.
- [Car13] A. Carmele, J. Kabuss, F. Schulze, S. Reitzenstein, A. Knorr. “Single Photon Delayed Feedback: A Way to Stabilize Intrinsic Quantum Cavity Electrodynamics”. *Physical Review Letters*, **110** (2013), 013601.
- [Cas17] M. Cassidy, A. Bruno, S. Rubbert, M. Irfan, J. Kammhuber, R. Schouten, A. Akhmerov, L. Kouwenhoven. “Demonstration of an ac Josephson junction laser”. *Science*, **355** (2017), 939.
- [Ciu98] C. Ciuti, V. Savona, C. Piermarocchi, A. Quattropani, P. Schwendimann. “Role of the exchange of carriers in elastic exciton-exciton scattering in quantum wells”. *Physical Review B*, **58** (1998), 7926.
- [DE14] J. Dreyling-Eschweiler. *A superconducting microcalorimeter for low-flux detection of near-infrared single photons*. Ph.D. thesis, Universität Hamburg (2014).
- [Den02] H. Deng, G. Weihs, C. Santori, J. Bloch, Y. Yamamoto. “Condensation of semiconductor microcavity exciton polaritons”. *Science*, **298** (2002), 199.
- [Den03] H. Deng, G. Weihs, D. Snoke, J. Bloch, Y. Yamamoto. “Polariton lasing vs. photon lasing in a semiconductor microcavity”. *Proceedings of the National Academy of Sciences*, **100** (2003), 15318.
- [Den10] H. Deng, H. Haug, Y. Yamamoto. “Exciton-polariton bose-einstein condensation”. *Reviews of Modern Physics*, **82** (2010), 1489.
- [Din16] X. Ding, Y. He, Z.-C. Duan, N. Gregersen, M.-C. Chen, S. Unsleber, S. Maier, C. Schneider, M. Kamp, S. Höfling, C.-Y. Lu, J.-W. Pan. “On-demand single photons with high extraction efficiency and near-unity indistinguishability from a resonantly driven quantum dot in a micropillar”. *Physical Review Letters*, **116** (2016).
- [DIC17] F. Denis-le Coarer, A. Quirce, Á. Valle, L. Pesquera, M. Sciamanna, H. Thienpont, K. Panajotov. “Polarization dynamics induced by parallel optical injection in a single-mode VCSEL”. *Optics letters*, **42** (2017), 2130.
- [DIC18] F. Denis-le Coarer, A. Quirce, A. Valle, L. Pesquera, M. A. Rodríguez, K. Panajotov, M. Sciamanna. “Attractor hopping between polarization dynamical states in a vertical-cavity surface-emitting laser subject to parallel optical injection”. *Physical Review E*, **97** (2018), 032201.

- [Dou10] A. Dousse, J. Suffczyński, A. Beveratos, O. Krebs, A. Lemaître, I. Sagnes, J. Bloch, P. Voisin, P. Senellart. “Ultrabright source of entangled photon pairs”. *Nature*, **466** (2010), 217.
- [Dru07] D. Drung, C. Abmann, J. Beyer, A. Kirste, M. Peters, F. Ruede, T. Schurig. “Highly sensitive and easy-to-use SQUID sensors”. *IEEE Transactions on Applied Superconductivity*, **17** (2007), 699.
- [Eic15] H. J. Eichler, J. Eichler. *Laser: Bauformen, Strahlführung, Anwendungen*. Springer-Verlag (2015).
- [Ern10] T. Erneux, P. Glorieux. *Laser dynamics*. Cambridge University Press (2010).
- [Fab93] L. Fabiny, P. Colet, R. Roy, D. Lenstra. “Coherence and phase dynamics of spatially coupled solid-state lasers”. *Physical Review A*, **47** (1993), 4287.
- [Fan16] M. Fanaei, A. Foerster, H. A. M. Leymann, J. Wiersig. “Effect of direct dissipative coupling of two competing modes on intensity fluctuations in a quantum-dot-microcavity laser”. *Physical Review A*, **94** (2016), 043814.
- [Fer11] L. Ferrier, E. Wertz, R. Johne, D. D. Solnyshkov, P. Senellart, I. Sagnes, A. Lemaître, G. Malpuech, J. Bloch. “Interactions in confined polariton condensates”. *Physical Review Letters*, **106** (2011), 126401.
- [Fox06] M. Fox. *Quantum optics: an introduction*, volume 15. Oxford University Press (2006).
- [Gat04] A. Gatti, E. Brambilla, M. Bache, L. A. Lugiato. “Ghost imaging with thermal light: comparing entanglement and classical correlation”. *Physical Review Letters*, **93** (2004), 093602.
- [Gat06] I. Gatara, M. Sciamanna, J. Buesa, H. Thienpont, K. Panajotov. “Nonlinear dynamics accompanying polarization switching in vertical-cavity surface-emitting lasers with orthogonal optical injection”. *Applied Physics Letters*, **88** (2006), 101106.
- [Gav97] A. Gavrielides, V. Kovanis, T. Erneux. “Analytical stability boundaries for a semiconductor laser subject to optical injection”. *Optics Communications*, **136** (1997), 253.
- [Gie07] C. Gies, J. Wiersig, M. Lorke, F. Jahnke. “Semiconductor model for quantum-dot-based microcavity lasers”. *Physical Review A*, **75** (2007), 013803.

- [Gie17] C. Gies, F. Gericke, P. Gartner, S. Holzinger, C. Hopfmann, T. Heindel, J. Wolters, C. Schneider, M. Florian, F. Jahnke, S. Höfling, M. Kamp, S. Reitzenstein. “Strong light-matter coupling in the presence of lasing”. *Physical Review A*, **96** (2017), 023806.
- [Gut98] T. Gutbrod, M. Bayer, A. Forchel, J. Reithmaier, T. Reinecke, S. Rudin, P. Knipp. “Weak and strong coupling of photons and excitons in photonic dots”. *Physical Review B*, **57** (1998), 9950.
- [Hal62] R. N. Hall, G. E. Fenner, J. D. Kingsley, T. J. Soltys, R. O. Carlson. “Coherent light emission from GaAs junctions”. *Physical Review Letters*, **9** (1962), 366.
- [Hay70] I. Hayashi, M. Panish, P. Foy, S. Sumski. “Junction lasers which operate continuously at room temperature”. *Applied Physics Letters*, **17** (1970), 109.
- [HB56] R. Hanbury-Brown, R. Q. Twiss. “Correlation between photons in two coherent beams of light”. *Nature*, **177** (1956), 27 .
- [Hec98] E. Hecht. “Optics”. *Addison Wesley*, **997** (1998), 213.
- [Hen82] C. Henry. “Theory of the linewidth of semiconductor lasers”. *IEEE Journal of Quantum Electronics*, **18** (1982), 259.
- [Heu19] T. Heuser, J. Große, S. Holzinger, M. Sommer, S. Reitzenstein. “Development of highly homogenous quantum dot micropillar arrays for optical reservoir computing”. *IEEE Journal of Selected Topics in Quantum Electronics Sel. Top. Quant.*, **26** (2019), 1900109.
- [Hol18] S. Holzinger, C. Redlich, B. Lingnau, M. Schmidt, M. von Helversen, J. Beyer, C. Schneider, M. Kamp, S. Höfling, K. Lüdge, X. Porte, S. Reitzenstein. “Tailoring the mode-switching dynamics in quantum-dot micropillar lasers via time-delayed optical feedback”. *Optics Express*, **26** (2018), 22457.
- [Hon02] Y. Hong, P. S. Spencer, P. Rees, K. A. Shore. “Optical injection dynamics of two-mode vertical cavity surface-emitting semiconductor lasers”. *IEEE Journal of Quantum Electronics*, **38** (2002), 274.
- [Hop58] J. J. Hopfield. “Theory of the Contribution of Excitons to the Complex Dielectric Constant of Crystals”. *Phys. Rev.*, **112** (1958), 1555.
- [Hor10] T. Horikiri, P. Schwendimann, A. Quattropani, S. Höfling, A. Forchel, Y. Yamamoto. “Higher order coherence of exciton-polariton condensates”. *Physical Review B*, **81** (2010), 033307.

- [Hui92] R. Hui, A. Mecozzi. “Phase noise of four-wave mixing in semiconductor lasers”. *Applied physics letters*, **60** (1992), 2454.
- [Ima96] A. Imamog, R. Ram, S. Pau, Y. Yamamoto, *et al.* “Nonequilibrium condensates and lasers without inversion: Exciton-polariton lasers”. *Physical Review A*, **53** (1996), 4250.
- [Irw05] K. Irwin, G. Hilton. *Cryogenic Particle Detection*. Springer (2005).
- [Jag18] S. T. Jagsch, N. V. Triviño, F. Lohof, G. Callsen, S. Kalinowski, I. M. Rousseau, R. Barzel, J.-F. Carlin, F. Jahnke, R. Butté, C. Gies, A. Hoffmann, N. Grandjean, S. Reitzenstein. “A quantum optical study of thresholdless lasing features in high- β nitride nanobeam cavities”. *Nature Communications*, **9** (2018), 564.
- [Jah12] F. Jahnke, editor. *Quantum optics with semiconductor nanostructures*. Elsevier (2012).
- [Jah16] F. Jahnke, C. Gies, M. Aßmann, M. Bayer, H. A. M. Leymann, A. Foerster, J. Wiersig, C. Schneider, M. Kamp, S. Höfling. “Giant photon bunching, superradiant pulse emission and excitation trapping in quantum-dot nanolasers”. *Natur Communications*, **7** (2016), 11540.
- [Jec13] A. Jechow, M. Seefeldt, H. Kurzke, A. Heuer, R. Menzel. “Enhanced two-photon excited fluorescence from imaging agents using true thermal light”. *Nature Photonics*, **7** (2013), 973.
- [Jeo06] Y. D. Jeong, J. S. Cho, Y. H. Won, H. J. Lee, H. Yoo. “All-optical flip-flop based on the bistability of injection locked Fabry-Perot laser diode”. *Optics express*, **14** (2006), 4058.
- [Kag19] A. Kaganskiy, S. Kreinberg, X. Porte, S. Reitzenstein. “Micropillar lasers with site-controlled quantum dots as active medium”. *Optica*, **6** (2019), 404.
- [Kas06] J. Kasprzak, M. Richard, S. Kundermann, A. Baas, P. Jeambrun, J. Keeling, F. Marchetti, M. Szymańska, R. André, J. Staehli, *et al.* “Bose–Einstein condensation of exciton polaritons”. *Nature*, **443** (2006), 409.
- [Kas08] J. Kasprzak, M. Richard, A. Baas, B. Deveaud, R. André, J.-P. Poizat, L. S. Dang. “Second-order time correlations within a polariton Bose-Einstein condensate in a CdTe microcavity”. *Physical Review Letters*, **100** (2008), 067402.

- [Kav17] A. V. Kavokin, J. J. Baumberg, G. Malpuech, F. P. Laussy. *Microcavities*. Oxford University Press (2017).
- [Kha12] M. Khajavikhan, A. Simic, M. Katz, J. H. Lee, B. Slutsky, A. Mizrahi, V. Lomakin, Y. Fainman. “Thresholdless nanoscale coaxial lasers”. *Nature*, **482** (2012), 204.
- [Kha15] M. Khanbekyan, H. A. M. Leymann, C. Hopfmann, A. Foerster, C. Schneider, S. Höfling, M. Kamp, J. Wiersig, S. Reitzenstein. “Unconventional collective normal-mode coupling in quantum-dot-based bimodal microlasers”. *Physical Review A*, **91** (2015), 043840.
- [Kla10] J. Klaers, J. Schmitt, F. Vewinger, M. Weitz. “Bose–Einstein condensation of photons in an optical microcavity”. *Nature*, **468** (2010), 545.
- [Kla18a] M. Klaas, H. Flayac, M. Amthor, I. G. Savenko, S. Brodbeck, T. Ala-Nissila, S. Klemmt, C. Schneider, S. Höfling. “Evolution of temporal coherence in confined exciton-polariton condensates”. *Physical Review Letters*, **120** (2018), 017401.
- [Kla18b] M. Klaas, E. Schlottmann, H. Flayac, F. P. Laussy, F. Gericke, M. Schmidt, M. v. Helversen, J. Beyer, S. Brodbeck, H. Suchomel, S. Höfling, S. Reitzenstein, C. Schneider. “Photon-number-resolved measurement of an exciton-polariton condensate”. *Physical Review Letters*, **121** (2018), 047401.
- [Kre17] S. Kreinberg, W. W. Chow, J. Wolters, C. Schneider, C. Gies, F. Jahnke, S. Höfling, M. Kamp, S. Reitzenstein. “Emission from quantum-dot high- β microcavities: transition from spontaneous emission to lasing and the effects of superradiant emitter coupling”. *Light: Science & Applications*, **6** (2017), e17030.
- [Kro63] H. Kroemer. “Semiconductor laser with electric pumping” (1963).
- [Kul10] V. D. Kulakovskii, A. V. Larionov, S. I. Novikov, S. Höfling, C. Schneider, A. Forchel. “Bose-Einstein condensation of exciton polaritons in high-Q planar microcavities with GaAs quantum wells”. *JETP Letters*, **92** (2010), 595.
- [LÖ8] A. Löffler. *Selbstorganisiertes Wachstum von (Ga)InAs/GaAs-Quantenpunkten und Entwicklung von Mikroresonatoren höchster Güte für Experimente zur starken Exziton-Photon-Kopplung*. Ph.D. thesis, Julius-Maximilians-Universität Würzburg, Fakultät für Physik und Astronomie (2008).

- [Lai07] C. W. Lai, N. Y. Kim, S. Utsunomiya, G. Roumpos, H. Deng, M. D. Fraser, T. Byrnes, P. Recher, N. Kumada, T. Fujisawa, Y. Yamamoto. “Coherent zero-state and π -state in an exciton–polariton condensate array”. *Nature*, **450** (2007), 529.
- [Lan80] R. Lang, K. Kobayashi. “External optical feedback effects on semiconductor injection laser properties”. *IEEE Journal of Quantum Electronics*, **16** (1980), 347.
- [Lar12] L. Larger, M. C. Soriano, D. Brunner, L. Appeltant, J. M. Gutiérrez, L. Pesquera, C. R. Mirasso, I. Fischer. “Photonic information processing beyond Turing: an optoelectronic implementation of reservoir computing”. *Optics Express*, **20** (2012), 3241.
- [Lau04] F. P. Laussy, G. Malpuech, A. Kavokin, P. Bigenwald. “Spontaneous coherence buildup in a polariton laser”. *Physical Review Letters*, **93** (2004), 016402.
- [Len93] D. Lenstra, G. H. M. van Tartwijk, W. A. van der Graaf, P. C. De Jagher. “Multiwave-mixing dynamics in a diode laser”. In *Chaos in Optics*, volume 2039, 11–23. International Society for Optics and Photonics (1993).
- [Ler13] M. Lerner, N. Gregersen, M. Lorke, E. Schild, P. Gold, J. Mørk, C. Schneider, A. Forchel, S. Reitzenstein, S. Höfling, M. Kamp. “High beta lasing in micropillar cavities with adiabatic layer design”. *Applied Physics Letters*, **102** (2013), 052114.
- [Ley13] H. Leymann, C. Hopfmann, F. Albert, A. Foerster, M. Khanbekyan, C. Schneider, S. Höfling, A. Forchel, M. Kamp, J. Wiersig, S. Reitzenstein. “Intensity fluctuations in bimodal micropillar lasers enhanced by quantum-dot gain competition”. *Physical Review A*, **87** (2013), 053819.
- [Ley14] H. A. M. Leymann, A. Foerster, J. Wiersig. “Expectation value based equation-of-motion approach for open quantum systems: a general formalism”. *Physical Review B*, **89** (2014), 085308.
- [Ley17] H. A. M. Leymann, D. Vorberg, T. Lettau, C. Hopfmann, C. Schneider, M. Kamp, S. Höfling, R. Ketzmerick, J. Wiersig, S. Reitzenstein, A. Eckardt. “Pump-power-driven mode switching in a microcavity device and its relation to Bose-Einstein condensation”. *Physical Review X*, **7** (2017), 021045.

- [Li96] H. Li, T. L. Lucas, J. G. McInerney, M. W. Wright, R. A. Morgan. “Injection locking dynamics of vertical cavity semiconductor lasers under conventional and phase conjugate injection”. *IEEE Journal of Quantum Electronics*, **32** (1996), 227.
- [Li08] B. Li, M. I. Memon, G. Mezosi, G. Yuan, Z. Wang, M. Sorel, S. Yu. “All-optical response of semiconductor ring laser to dual-optical injections”. *IEEE Photonics Technology Letters*, **20** (2008), 770.
- [Lin15a] B. Lingnau. *Nonlinear and nonequilibrium dynamics of quantum-dot optoelectronic devices*. Springer (2015).
- [Lin15b] B. Lingnau, K. Lüdge. “Analytic characterization of the dynamic regimes of quantum-dot lasers”. In *Photonics*, volume 2, 402–413. Multidisciplinary Digital Publishing Institute (2015).
- [Lin17] H. Lin, S. Ourari, T. Huang, A. Jha, A. Briggs, N. Bigagli. “Photonic microwave generation in multimode VCSELs subject to orthogonal optical injection”. *Journal of the Optical Society of America B*, **34** (2017), 2381.
- [Lin19] M. Lindemann, G. Xu, T. Pusch, R. Michalzik, M. R. Hofmann, I. Žutić, N. C. Gerhardt. “Ultrafast spin-lasers”. *Nature*, **568** (2019), 212.
- [Lit08] A. E. Lita, A. J. Miller, S. W. Nam. “Counting near-infrared single-photons with 95 % efficiency”. *Optics Express*, **16** (2008), 3032.
- [Liu94] J.-M. Liu, T. B. Simpson. “Four-wave mixing and optical modulation in a semiconductor laser”. *IEEE Journal of Quantum Electronics*, **30** (1994), 957.
- [Lou83] R. Loudon. *The quantum theory of light*. Oxford Science Publications, 2. edition (1983).
- [Lou00] R. Loudon. *The quantum theory of light*. Oxford Science Publications (2000).
- [Lov08] A. P. D. Love, D. N. Krizhanovskii, D. M. Whittaker, R. Bouchekioua, D. Sanvitto, S. Al Rizeiqi, R. Bradley, M. S. Skolnick, P. R. Eastham, R. André, L. S. Dang. “Intrinsic decoherence mechanisms in the microcavity polariton condensate”. *Physical Review Letters*, **101** (2008), 067404.
- [Lu12] Y.-J. Lu, J. Kim, H.-Y. Chen, C. Wu, N. Dabidian, C. E. Sanders, C.-Y. Wang, M.-Y. Lu, B.-H. Li, X. Qiu, W.-H. Chang, J. Chen, G. Shvets, C.-K. Shih,

- S. Gwo. “Plasmonic nanolaser using epitaxially grown silver film”. *Science*, **337** (2012), 450.
- [Lüd12] K. Lüdge, H. G. Schuster. *Nonlinear laser dynamics: from quantum dots to cryptography*. John Wiley & Sons (2012).
- [Ma19] R.-M. Ma, R. F. Oulton. “Applications of nanolasers”. *Nature Nanotechnology*, **14** (2019), 12.
- [Mac86] H. A. Macleod. *Thin-film optical filters*. Macmillan Publishing Company, New York, 2. edition (1986).
- [Mai60] T. H. Maiman. “Stimulated optical radiation in ruby”. *Nature*, **187** (1960), 493.
- [Mar16] M. Marconi, J. Javaloyes, F. Raineri, J. A. Levenson, A. M. Yacomotti. “Asymmetric mode scattering in strongly coupled photonic crystal nanolasers”. *Optics Letters*, **41** (2016), 5628.
- [Mar18] M. Marconi, J. Javaloyes, P. Hamel, F. Raineri, A. Levenson, A. M. Yacomotti. “Far-from-equilibrium route to superthermal light in bimodal nanolasers”. *Physical Review X*, **8** (2018), 011013.
- [Mic00] P. Michler, A. Kiraz, L. Zhang, C. Becher, E. Hu, A. Imamoglu. “Laser emission from quantum dots in microdisk structures”. *Applied Physics Letters*, **77** (2000), 184.
- [Mic09] P. Michler. *Single semiconductor quantum dots*. Springer (2009).
- [Mig13] A. Migdall, S. V. Polyakov, J. Fan, J. C. Bienfang. *Single-photon generation and detection: physics and applications*, volume 45. Academic Press (2013).
- [Mil03] A. J. Miller, S. W. Nam, J. M. Martinis, A. V. Sergienko. “Demonstration of a low-noise near-infrared photon counter with multiphoton discrimination”. *Applied Physics Letters*, **83** (2003), 791.
- [Mil11] A. J. Miller, A. E. Lita, B. Calkins, I. Vayshenker, S. M. Gruber, S. W. Nam. “Compact cryogenic self-aligning fiber-to-detector coupling with losses below one percent”. *Optics Express*, **19** (2011), 9102.
- [Mor06] T. Mori, Y. Yamayoshi, H. Kawaguchi. “Low-switching-energy and high-repetition-frequency all-optical flip-flop operations of a polarization bistable vertical-cavity surface-emitting laser”. *Applied Physics Letters*, **88** (2006), 101102.

- [MT78] M. M-Tehrani, L. Mandel. “Intensity fluctuations in a two-mode ring laser”. *Physical Review A*, **17** (1978), 694.
- [Nak85a] H. Nakajima, R. Frey. “Intracavity nearly degenerate four-wave mixing in a (GaAl) As semiconductor laser”. *Applied Physics Letters*, **47** (1985), 769.
- [Nak85b] H. Nakajima, R. Frey. “Observation of bistable reflectivity of a phase-conjugated signal through intracavity nearly degenerate four-wave mixing”. *Physical Review Letters*, **54** (1985), 1798.
- [Nak86] H. Nakajima, R. Frey. “Collinear nearly degenerate four-wave mixing in intracavity amplifying media”. *IEEE Journal of Quantum Electronics*, **22** (1986), 1349.
- [Nat62] M. I. Nathan, W. P. Dumke, G. Burns, F. H. Dill Jr, G. Lasher. “Stimulated emission of radiation from GaAs p-n junctions”. *Applied Physics Letters*, **1** (1962), 62.
- [Nez10] M. P. Nezhad, A. Simic, O. Bondarenko, B. Slutsky, A. Mizrahi, L. Feng, V. Lomakin, Y. Fainman. “Room-temperature subwavelength metallo-dielectric lasers”. *Nature Photonics*, **4** (2010), 395.
- [Nie89] R. Nietzke, P. Panknin, W. Elsasser, E. O. Gobel. “Four-wave mixing in GaAs/AlGaAs semiconductor lasers”. *IEEE Journal of Quantum Electronics*, **25** (1989), 1399.
- [Oht12] J. Ohtsubo. *Semiconductor lasers: stability, instability and chaos*, volume 111. Springer (2012).
- [Ole11] L. Olejniczak, K. Panajotov, H. Thienpont, M. Sciamanna, A. Mutig, F. Hopfer, D. Bimberg. “Polarization switching and polarization mode hopping in quantum dot vertical-cavity surface-emitting lasers”. *Optics Express*, **19** (2011), 2476.
- [O’s14] D. O’shea, S. Osborne, N. Blackbeard, D. Goulding, B. Kelleher, A. Amann. “Experimental classification of dynamical regimes in optically injected lasers”. *Optics Express*, **22** (2014), 21701.
- [Pan93] Z. G. Pan, S. Jiang, M. Dagenais, R. A. Morgan, K. Kojima, M. T. Asom, R. E. Leibenguth, G. D. Guth, M. W. Focht. “Optical injection induced polarization bistability in vertical-cavity surface-emitting lasers”. *Applied Physics Letters*, **63** (1993), 2999.

- [Par08] D. Parekh, X. Zhao, W. Hofmann, M. C. Amann, L. A. Zenteno, C. J. Chang-Hasnain. “Greatly enhanced modulation response of injection-locked multimode VCSELs”. *Optics Express*, **16** (2008), 21582.
- [Pet88] I. Petitbon, P. Gallion, G. Debarge, C. Chabran. “Locking bandwidth and relaxation oscillations of an injection-locked semiconductor laser”. *IEEE Journal of Quantum Electronics*, **24** (1988), 148.
- [Red16] C. Redlich, B. Lingnau, S. Holzinger, E. Schlottmann, S. Kreinberg, C. Schneider, M. Kamp, S. Höfling, J. Wolters, S. Reitzenstein, K. Lüdge. “Mode-switching induced super-thermal bunching in quantum-dot microlasers”. *New Journal of Physics*, **18** (2016), 063011.
- [Rei04] J. P. Reithmaier, G. Sęk, A. Löffler, C. Hofmann, S. Kuhn, S. Reitzenstein, L. V. Keldysh, V. D. Kulakovskii, T. L. Reinecke, A. Forchel. “Strong coupling in a single quantum dot-semiconductor microcavity system”. *Nature*, **432** (2004), 197.
- [Rei06] S. Reitzenstein, A. Bazhenov, A. Gorbunov, C. Hofmann, S. Münch, A. Löffler, M. Kamp, J. P. Reithmaier, V. D. Kulakovskii, A. Forchel. “Lasing in high-Q quantum-dot micropillar cavities”. *Applied Physics Letters*, **89** (2006), 051107.
- [Rei07] S. Reitzenstein, C. Hofmann, A. Gorbunov, M. Strauß, S. H. Kwon, C. Schneider, A. Löffler, S. Höfling, M. Kamp, A. Forchel. “AlAs/GaAs micropillar cavities with quality factors exceeding 150.000”. *Applied Physics Letters*, **90** (2007), 251109.
- [Rei08a] S. Reitzenstein, C. Böckler, A. Bazhenov, A. Gorbunov, A. Löffler, M. Kamp, V. D. Kulakovskii, A. Forchel. “Single quantum dot controlled lasing effects in high-Q micropillar cavities”. *Optics Express*, **16** (2008), 4848.
- [Rei08b] S. Reitzenstein, T. Heindel, C. Kistner, A. Rahimi-Iman, C. Schneider, S. Höfling, A. Forchel. “Low threshold electrically pumped quantum dot-micropillar lasers”. *Applied Physics Letters*, **93** (2008), 061104.
- [Rei10] S. Reitzenstein, A. Forchel. “Quantum dot micropillars”. *Journal of Physics D: Applied Physics*, **43** (2010), 033001.
- [Rog01] F. Rogister, A. Locquet, D. Pieroux, M. Sciamanna, O. Deparis, P. Mégret, M. Blondel. “Secure communication scheme using chaotic laser diodes subject

- to incoherent optical feedback and incoherent optical injection”. *Optics Letters*, **26** (2001), 1486.
- [Ros18] I. Rosenberg, D. Liran, Y. Mazuz-Harpaz, K. West, L. Pfeiffer, R. Rapaport. “Strongly interacting dipolar-polaritons”. *Science Advances*, **4** (2018), eaat8880.
- [Sal15] M. F. Salvide, M. S. Torre, I. D. Henning, M. J. Adams, A. Hurtado. “Dynamics of normal and reverse polarization switching in 1550-nm VCSELs under single and double optical injection”. *IEEE Journal of Selected Topics in Quantum Electronics*, **21** (2015), 643.
- [San02] C. Santori, D. Fattal, J. Vučković, G. S. Solomon, Y. Yamamoto. “Indistinguishable photons from a single-photon device”. *Nature*, **419** (2002), 594.
- [Sat16] Z. A. Sattar, N. A. Kamel, K. A. Shore. “Optical injection effects in nanolasers”. *IEEE Journal of Quantum Electronics*, **52** (2016), 1.
- [Sch08] P. Schwendimann, A. Quattropani. “Statistics of the polariton condensate”. *Physical Review B*, **77** (2008), 085317.
- [Sch16] E. Schlottmann, S. Holzinger, B. Lingnau, K. Lüdge, C. Schneider, M. Kamp, S. Höfling, J. Wolters, S. Reitzenstein. “Injection Locking of Quantum-Dot Microlasers Operating in the Few-Photon Regime”. *Physical Review Applied*, **6** (2016), 044023.
- [Sch18a] D. Schicke. *Stochastic switching dynamics of QD micropillar lasers under optical perturbations*. Master’s thesis, Technische Universität Berlin (2018).
- [Sch18b] E. Schlottmann, M. von Helversen, H. A. M. Leymann, T. Lettau, F. Krüger, M. Schmidt, C. Schneider, M. Kamp, S. Höfling, J. Beyer, J. Wiersig, S. Reitzenstein. “Exploring the Photon-Number Distribution of Bimodal Microlasers with a Transition Edge Sensor”. *Physical Review Applied*, **9** (2018), 064030.
- [Sch18c] M. Schmidt, M. von Helversen, M. López, F. Gericke, E. Schlottmann, T. Heindel, S. Kück, S. Reitzenstein, J. Beyer. “Photon-Number-Resolving Transition-Edge Sensors for the Metrology of Quantum Light Sources”. *Journal of Low Temperature Physics*, **193** (2018), 1243.
- [Sch19] E. Schlottmann, D. Schicke, F. Krüger, B. Lingnau, C. Schneider, S. Höfling, K. Lüdge, X. Porte, S. Reitzenstein. “Stochastic polarization switching induced by optical injection in bimodal quantum-dot micropillar lasers”. *Optics Express*, **27** (2019), 28816.

- [Scu67] M. O. Scully, W. E. Lamb Jr. “Quantum theory of an optical maser. I. General theory”. *Physical Review*, **159** (1967), 208.
- [She95] C. J. R. Sheppard. “Approximate calculation of the reflection coefficient from a stratified medium”. *Pure and Applied Optics: Journal of the European Optical Society Part A*, **4** (1995), 665.
- [Sim97] T. B. Simpson, J. M. Liu. “Enhanced modulation bandwidth in injection-locked semiconductor lasers”. *IEEE Photonics Technology Letters*, **9** (1997), 1322.
- [Sin79] S. Singh, L. Mandel. “Mode competition in a homogeneously broadened ring laser”. *Physical Review A*, **20** (1979), 2459.
- [Slu93] R. E. Slusher, A. F. J. Levi, U. Mohideen, S. L. McCall, S. J. Pearton, R. A. Logan. “Threshold characteristics of semiconductor microdisk lasers”. *Applied Physics Letters*, **63** (1993), 1310.
- [Sod79] H. Soda, K.-i. Iga, C. Kitahara, Y. Suematsu. “GaInAsP/InP surface emitting injection lasers”. *Japanese Journal of Applied Physics*, **18** (1979), 2329.
- [Sto66] H. L. Stover, W. H. Steier. “Locking of laser oscillators by light injection”. *Applied Physics Letters*, **8** (1966), 91.
- [Str37] I. N. Stranski, L. Krastanow. “Zur Theorie der orientierten Ausscheidung von Ionenkristallen aufeinander”. *Monatshefte für Chemie und verwandte Teile anderer Wissenschaften*, **71** (1937), 351.
- [Str06] S. Strauf, K. Hennessy, M. T. Rakher, Y.-S. Choi, A. Badolato, L. C. Andreani, E. L. Hu, P. M. Petroff, D. Bouwmeester. “Self-tuned quantum dot gain in photonic crystal lasers”. *Physical Review Letters*, **96** (2006), 127404.
- [Sun17] Y. Sun, P. Wen, Y. Yoon, G. Liu, M. Steger, L. N. Pfeiffer, K. West, D. W. Snoke, K. A. Nelson. “Bose-Einstein condensation of long-lifetime polaritons in thermal equilibrium”. *Physical Review Letters*, **118** (2017), 016602.
- [Tem12] J.-S. Tempel, F. Veit, M. Aßmann, L. E. Kreilkamp, A. Rahimi-Iman, A. Löffler, S. Höfling, S. Reitzenstein, L. Worschech, A. Forchel, M. Bayer. “Characterization of two-threshold behavior of the emission from a GaAs microcavity”. *Phys. Rev. B*, **85** (2012), 075318.
- [Uch08] A. Uchida, K. Amano, M. Inoue, K. Hirano, S. Naito, H. Someya, I. Oowada, T. Kurashige, M. Shiki, S. Yoshimori, K. Yoshimura, P. Davis. “Fast physical

- random bit generation with chaotic semiconductor lasers”. *Nature Photonics*, **2** (2008), 728.
- [Ulr07] S. M. Ulrich, C. Gies, S. Ates, J. Wiersig, S. Reitzenstein, C. Hofmann, A. Löffler, A. Forchel, F. Jahnke, P. Michler. “Photon statistics of semiconductor microcavity lasers”. *Physical Review Letters*, **98** (2007), 043906.
- [Val07] A. Valle, I. Gatara, K. Panajotov, M. Sciamanna. “Transverse mode switching and locking in vertical-cavity surface-emitting lasers subject to orthogonal optical injection”. *IEEE Journal of Quantum Electronics*, **43** (2007), 322.
- [vH17] M. von Helversen. *Quantenoptische Charakterisierung nanophotonischer Strukturen mittels photonenzahlauflösender Detektoren*. Master’s thesis, Technische Universität Berlin (2017).
- [Vir13] M. Virte, K. Panajotov, H. Thienpont, M. Sciamanna. “Deterministic polarization chaos from a laser diode”. *Nature Photonics*, **7** (2013), 60.
- [Wei91] C. O. Weiss, R. Vilaseca. *Dynamics of lasers*, volume 92. VCH Publishing (1991).
- [Wei92] C. Weisbuch, M. Nishioka, A. Ishikawa, Y. Arakawa. “Observation of the coupled exciton-photon mode splitting in a semiconductor quantum microcavity”. *Physical Review Letters*, **69** (1992), 3314.
- [Wie05] S. Wieczorek, B. Krauskopf, T. B. Simpson, D. Lenstra. “The dynamical complexity of optically injected semiconductor lasers”. *Physics Reports*, **416** (2005), 1.
- [Wie09] J. Wiersig, C. Gies, F. Jahnke, M. Aßmann, T. Berstermann, M. Bayer, C. Kistner, S. Reitzenstein, C. Schneider, S. Höfling, A. Forchel, C. Kruse, J. Kalden, D. Hommel. “Direct observation of correlations between individual photon emission events of a microcavity laser”. *Nature*, **460** (2009), 245.
- [Wim14] S. Wimberger. *Nonlinear dynamics and quantum chaos*. Springer (2014).
- [Yua07a] G. Yuan, S. Yu. “Analysis of dynamic switching behavior of bistable semiconductor ring lasers triggered by resonant optical pulse injection”. *IEEE Journal of Selected Topics in Quantum Electronics*, **13** (2007), 1227.
- [Yua07b] G. Yuan, S. Yu. “Bistability and switching properties of semiconductor ring lasers with external optical injection”. *IEEE Journal of Quantum Electronics*, **44** (2007), 41.

A Appendix

A.1 Layer Design Sample M4072

quantity	material & thickness	doping
2 ·	GaAs 60 nm	$2 \cdot 10^{19}$ 1/cm p-doped
	AlAs 71 nm	
9 ·	GaAs 60 nm	$3 \cdot 10^{18}$ 1/cm p-doped
	AlAs 71 nm	
5 ·	GaAs 60 nm	$2 \cdot 10^{18}$ 1/cm p-doped
	AlAs 71 nm	
7 ·	GaAs 60 nm	$1 \cdot 10^{18}$ 1/cm p-doped
	AlAs 71 nm	
	GaAs cavity 264 nm, including one layer InGaAs QDs	
	AlAs 71 nm	
4 ·	GaAs 60 nm	$1 \cdot 10^{18}$ 1/cm n-doped
	AlAs 71 nm	
5 ·	GaAs 60 nm	$2 \cdot 10^{18}$ 1/cm n-doped
	AlAs 71 nm	
17 ·	GaAs 60 nm	$3 \cdot 10^{18}$ 1/cm n-doped
	AlAs 71 nm	
	GaAs buffer 300 nm	$3 \cdot 10^{18}$ 1/cm n-doped
	GaAs substrate	n-doped

A.2 Layer Design Sample M2977

quantity	material & thickness	doping
2 ·	GaAs 63 nm	$2 \cdot 10^{19}$ 1/cm p-doped
	AlAs 76 nm	
9 ·	GaAs 63 nm	$3 \cdot 10^{18}$ 1/cm p-doped
	AlAs 76 nm	
5 ·	GaAs 63 nm	$2 \cdot 10^{18}$ 1/cm p-doped
	AlAs 76 nm	
7 ·	GaAs 63 nm	$1 \cdot 10^{18}$ 1/cm p-doped
	AlAs 76 nm	
	GaAs cavity 264 nm, including one layer InGaAs QDs	
	AlAs 76 nm	
4 ·	GaAs 63 nm	$1 \cdot 10^{18}$ 1/cm n-doped
	AlAs 76 nm	
5 ·	GaAs 63 nm	$2 \cdot 10^{18}$ 1/cm n-doped
	AlAs 76 nm	
17 ·	GaAs 63 nm	$3 \cdot 10^{18}$ 1/cm n-doped
	AlAs 76 nm	
	GaAs buffer 300 nm	$3 \cdot 10^{18}$ 1/cm n-doped
	GaAs substrate	n-doped

A.3 Layer Design Sample M4159

quantity	material & thickness
22 ·	AlAs 67 nm
	AlGaAs 58 nm
	AlAs 30 nm
	GaAs 13 nm QW
3 ·	AlAs 4 nm
	GaAs 13 nm QW
	AlAs 31 nm
	AlGaAs 21 nm
	GaAs 13 nm QW
3 ·	AlAs 4 nm
	GaAs 13 nm QW
	AlGaAs 21 nm
	AlAs 31 nm
	GaAs 13 nm QW
3 ·	AlAs 4 nm
	GaAs 13 nm QW
	AlAs 30 nm
26 ·	AlGaAs 58 nm
	AlAs 67 nm
	GaAs substrate

Acknowledgements / Danksagung

Mein Dank gilt allen, die mich in der langen Zeit an der TU Berlin begleitet haben.

Prof. Stephan Reitzenstein, der mich für die Masterarbeit in die Gruppe geholt hat und mir die Möglichkeit gegeben hat hier meine Doktorarbeit anzufertigen.

Prof. Frédéric Grillot, der sich bereit erklärt hat Gutachter für meine Dissertation zu sein und die Reise nach Berlin anzutreten. Prof. Ulrike Woggon, die den Vorsitz meiner wissenschaftlichen Aussprache übernimmt.

Meinen ehemaligen Studenten Martin von Helversen und Felix Krüger, die maßgeblich zu den Ergebnissen dieser Arbeit beigetragen haben. Es hat mit euch immer viel Spaß gemacht!

Prof. Kathy Lüdge, Benjamin Lingnau, David Schicke und Christoph Redlich für die gute Zusammenarbeit und die Simulationen zur optischen Injektion.

Alex Leymann, Prof. Jan Wiersig, Thomas Lettau, Alex Foerster und Mikael Khanbekyan für die tollen Diskussionen in Magdeburg und die Simulationen zu Mikrosäulen-Lasern und zur Photonenstatistik.

Marco Schmidt und Jörn Beyer für die Bereitstellung des Transition-Edge Sensors, der viele Messungen erst ermöglicht hat.

Christian Schneider und Prof. Sven Höfiling für das Wachstum und die Prozessierung der Quantenpunkt-Mikrosäulen-Laser und gemeinsam mit Martin Klaas, Hugo Flayac und Prof. Fabrice Laussy für die Zusammenarbeit in dem Exziton-Polariton-Laser Projekt.

Dem ganzen ERC-Team.

Alex Thoma, Marco Schmidt, Martin von Helversen, Tobias und Luzy Heindel, Felix Krüger, Pierce Munnely, Sven Rodt, Milo Sommer, Max Strauß, Fabian Gericke, Peter Schnauber, Xavi Porte, Steffen Holzinger, Sören Kreinberg, Janik Wolters, Lucas Bremer, Anna Musial und allen Kolleginnen und Kollegen der AG Reitzenstein, die die Arbeitsgruppe zu mehr als nur einem kollegialem Ort gemacht haben.

Doro, Fabs, Leo, Hakim, Csongor, Lucas, Daniel, Nele, Matti, Paul, Basti, Timo, Robert, Mascha, Erik, Anatoli, Konsti (in alph. Reihenfolge) und allen aktiven und ehemaligen Mitgliedern der Ini Physik für unsere gute gemeinsame Arbeit. Der Mittelbauinitiative, insbesondere Franz-Josef Schmitt, und den WiMis im Fakultätsrat.

Tobias Bischoff, Tim Oelze, Mario Sauppe und Hans Tornatzky, die mein Schicksal teilen und wir uns gegenseitig motivieren konnten. Unser Jour Faxe und der Samosa Friday werden mir fehlen. Meinen Studierenden aus dem Praktikum Kimon, Philipp, Moritz, Andrej, Andi, Kevin, Marta und Jeronimo.

Meine Familie, die mich immer unterstützt hat zu promovieren.

In ganz besonderem Maße danke ich meinem Lebensgefährten Arash, der mich das ganze Studium über tatkräftig unterstützt hat und mir mit viel Liebe in allen anstrengenden Zeiten beistand ♡♡♡